



저작자표시-비영리-변경금지 2.0 대한민국

이용자는 아래의 조건을 따르는 경우에 한하여 자유롭게

- 이 저작물을 복제, 배포, 전송, 전시, 공연 및 방송할 수 있습니다.

다음과 같은 조건을 따라야 합니다:



저작자표시. 귀하는 원저작자를 표시하여야 합니다.



비영리. 귀하는 이 저작물을 영리 목적으로 이용할 수 없습니다.



변경금지. 귀하는 이 저작물을 개작, 변형 또는 가공할 수 없습니다.

- 귀하는, 이 저작물의 재이용이나 배포의 경우, 이 저작물에 적용된 이용허락조건을 명확하게 나타내어야 합니다.
- 저작권자로부터 별도의 허가를 받으면 이러한 조건들은 적용되지 않습니다.

저작권법에 따른 이용자의 권리는 위의 내용에 의하여 영향을 받지 않습니다.

이것은 [이용허락규약\(Legal Code\)](#)을 이해하기 쉽게 요약한 것입니다.

[Disclaimer](#)

Abstract

Numerical Studies on the GaN Thin Film Layer Grown on Sapphire Wafer by Multi-Wafer Hydride Vapor Phase Epitaxy Equipment

Xuefeng Han

Department of Material Science and Engineering

The Graduate School

Seoul National University

In this study, experimental analysis and numerical simulation analysis have been exploited to investigate the effects of operating parameters on the uniformity of deposition thickness in a new multi-wafer hydride vapor phase epitaxy (HVPE) device. The numerical calculation results have shown the same trend with the experimental results demonstrating that increasing the carrier gas flow rate could shift the maximum value position of the deposition rate to increase the uniformity of the deposition rate distribution within the wafer. Moreover, the temperature effect, pressure effect, susceptor rotation effect, wafer rotation effect and carrier gas composition effect on the uniformity of the deposition thickness are evaluated through the analysis of standard deviation. Among the operating parameters, wafer rotation could not be directly simulated due to its complexity. However, we employed a method to track the trajectory of the points at the wafers to obtain the deposition rate

distribution, which has considered the coupled effects of the susceptor rotation and wafer rotation. Through the numerical analysis, it is concluded that with regard to the uniformity of deposition thickness along the radial direction, high carrier gas flow rate, high temperature, low pressure, low rotation speed and nitrogen as the carrier gas are the optimized conditions.

Moreover, in order to investigate the factors in affecting the distribution of the density of the hillocks along radial direction, we have conducted calculations to observe the fluid flow, mass transfer and deposition rate distribution. The numerical calculation results have shown that due to rotation of the susceptor, the wafers have experienced high and low growth rate alternately. So the growth rate fluctuations at different distances from the inlets are compared by standard deviation analysis. The calculation results show that the standard deviations of deposition rates along the azimuthal direction increase from the center to the periphery, which might explain why the density of the hillocks increases from the center to the periphery in the experiments. Moreover, it is found that the non-uniform deposition rates are the result of low speed rotation of the susceptor. Increasing rotation speed of the susceptor increases the uniformity of the gas flow pattern and deposition rate, which means that the high rotation speed can decrease the standard deviation of the deposition rate along azimuthal direction. Consequently, the

density of the hillocks can be decreased. Thus, through the numerical analysis, we predict that the high speed rotation will prevent the hillock formation in the multi-wafer horizontal HVPE equipment.

We also proposed a 3D multi-susceptor model for analyzing the GaN deposition thickness distribution and V/III ratio distribution at the GaN deposition surface. The GaN thin film is grown in the multi-susceptor HVPE equipment at 1213 K and 1 Bar. The deposition thickness distributions from the calculations have been compared with the experimental results. Moreover, the standard deviations of deposition thickness of the films achieved from calculations and experiments have been compared. Besides, in the calculation results, we found that the V/III ratio at the GaN deposition surface increases from the center to the periphery and from low susceptor to high susceptor. Our calculation results have also been verified by LMM (Laser measuring microscope) observation of the surface morphology of the GaN thin film. In according with the calculation results, the density of the pits also decreases from the center to the periphery as well as from low susceptor to high susceptor, demonstrating that our calculation model has the capability to predict the distribution of the pits at the surface of the GaN thin films.

Key words: GaN, multi-wafer HVPE, CFD simulation, pits, hillocks, fluid flow, surface reaction.

Student number: 2011-22858

Contents

Abstract	I
Contents	IV
List of Figures	IX
List of Tables	XVI
Chapter 1. Introduction	1
1.1 Background.....	1
1.2 GaN bulk crystal growth method	4
1.2.1 High nitrogen pressure solution growth (HNPSG).....	4
1.2.2 Na-flux method.....	6
1.2.3 Ammonothermal method.....	8
1.3 GaN thin film growth method.....	10
1.3.1 Metalorganic chemical vapor deposition (MOCVD).....	10
1.3.2 Hydride vapor phase epitaxy (HVPE)	12
1.4 Aims of HVPE research.....	14
Chapter 2. Numerical modeling	16
2.1 Flow.....	16
2.1.1 Mass conservation	16

2.1.2 Momentum conservation.....	17
2.1.3 Navier-Stokes equations.....	18
2.2 Heat Transfer.....	20
2.3 Chemical reaction.....	22
2.3.1 Composition variables	22
2.3.2 Chemical rate expressions.....	24
2.3.3 Surface reaction models	28
2.4 Mixture fractions	31
Chapter 3. Experiments	33
Chapter 4. Four-way nozzle design.....	37
4.1 Introduction.....	37
4.1.1 Deposition uniformity.....	37
4.1.2 Surface morphology.....	38
4.2 Model description.....	40
4.3 Simulation conditions	43
4.3.1 Boundary conditions	43
4.3.2 Volume conditions	44
4.4 Results and discussion.....	45

4.4.1 Operating parameter effect	45
4.4.1.1 Carrier gas flow rate effect	45
4.4.1.2 Temperature effect.....	55
4.4.1.3 Pressure effect	63
4.4.1.5 Wafer rotation effect.....	73
4.4.1.6 Carrier gas composition effect	86
4.4.2 Effect of non-uniform deposition rate on hillocks	93
4.4.2.1 Hillock distribution at the GaN surface	93
4.4.2.2 Growth rate distribution along the radial direction	97
4.4.2.3 Growth rate distribution along the rotation direction	99
4.4.2.4 Rotation effect on non-uniform deposition rate	104
4.5 Summary.....	110
4.5.1 Thickness uniformity	110
4.5.2 Processing time.....	115
4.5.3 Hillock density distribution.....	119
Chapter 5. Three-way nozzle design	120
5.1 Introduction.....	120
5.2 Model description.....	121

5.3 Simulation conditions	123
5.3.1 Boundary conditions	123
5.3.2 Volume conditions	125
5.4 Results and discussion	126
5.4.1 Fluid flow analysis	126
5.4.1.1 Fluid flow of GaCl	126
5.4.1.2 Fluid flow of NH ₃	128
5.4.4.3 Flow velocity at different susceptors	130
5.4.2 Deposition rate analysis	134
5.4.3 Reacting gas distribution analysis	136
5.4.3.1 GaCl analysis at horizontal cross section	136
5.4.3.2 GaCl and NH ₃ analysis at vertical cross section	138
5.4.4 Experimental verification of deposition rate	142
5.4.5 Effect of backflow	148
5.4.6 V-III ratio distribution	151
5.4.7 Experimental verification of V-III ratio distribution	153
5.5 Summary	155
Chapter 6. Conclusions	156

References	158
초록.....	177
Curriculum Vitae	179
Education.....	오류! 책갈피가 정의되어 있지 않습니다.
Journal Publications	오류! 책갈피가 정의되어 있지 않습니다.
International Conference ..	오류! 책갈피가 정의되어 있지 않습니다.

List of Figures

Figure 1.1 Packaged LED market trend. [20].....	3
Figure 1.2 Photograph of the HNPSG equipment. [29]	5
Figure 1.3 Schematic diagram of the Na flux method. [33]	7
Figure 1.4 Experimental configuration of ammonothermal GaN growth. [10]	9
Figure 1.5 Photo of MOCVD equipment produced by Aixtron [58]	11
Figure 1.6 Schematic diagram of hydride vapor phase epitaxy [70]	13
Figure 3.1 Schematic configuration of the equipment from the top view.	35
Figure 3.2 Method of measuring the thickness distribution	36
Figure 4.1 Schematic diagram of multi-wafer HVPE equipment.	42
Figure 4.2 GaN deposition rate distributions under different carrier gas flow rates: 7 slm, 13 slm, 19 slm, 30 slm.	46
Figure 4.3 Comparison of experimental result and calculation result with carrier gas flow rate of 7slm and 30slm.	47
Figure 4.4 Deposition thickness distributions along the radial direction from the inlet with different flow rates of carrier gas: 7slm, 13slm, 19slm, 30slm.	49
Figure 4.5 Standard deviations of the deposition thickness under different carrier gas flow rate conditions.....	49

Figure 4.6 Mass fraction distributions of the species along the inlet direction: (a) GaCl; (b) NH ₃	52
Figure 4.7 Mass fraction distributions of the species along the direction in the middle of the two adjacent inlets: (a) GaCl; (b) NH ₃	54
Figure 4.8 GaN deposition rate distribution under different temperature conditions: 1173 K, 1223 K, 1273K.	58
Figure 4.9 Deposition rate distributions along the radial direction from the inlet with different temperatures: 1173 K, 1223 K, 1273 K.....	58
Figure 4.10 Deposition thickness distributions along the radial direction from the inlet with different temperatures: 1173 K, 1223 K, 1273 K.	61
Figure 4.11 Standard deviations of the deposition thickness under different temperature conditions.	61
Figure 4.12 (a) GaCl mass fraction distributions along the radial direction; (b) normalized mass fractions at the upstream and the downstream with different temperatures.	62
Figure 4.13 GaN deposition rate distribution under different pressure conditions: 0.3 Bar, 0.6 Bar, 1 Bar.....	65
Figure 4.14 Deposition rate distributions along the radial direction from the inlet with different pressures: 0.3 Bar, 0.6 Bar, 1 Bar.	66

Figure 4.15 Deposition thickness distributions along the radial direction from the inlet with different pressures: 0.3 Bar, 0.6 Bar, 1 Bar.....	66
Figure 4.16 Standard deviations of the deposition thickness under different pressure conditions.	67
Figure 4.17 GaN deposition rate distribution under different rotation speeds: 2.5 rpm, 5 rpm, 10 rpm, 15 rpm.....	70
Figure 4.18 Deposition rate distributions along the radial direction from the inlet with different rotation speeds: 0 rpm, 5 rpm, 10 rpm, 15 rpm.	71
Figure 4.19 Deposition thickness distributions along the radial direction from the inlet with different rotation speeds: 0 rpm, 5 rpm, 10 rpm, 15 rpm.	71
Figure 4.20 Standard deviations of the deposition thickness under different rotation speed conditions.....	72
Figure 4.21 Schematic diagram of the movement of a certain point at the wafer.....	75
Figure 4.22 Trajectories of the points at the wafers over time under revolution and rotation are 5 rpm and 10 rpm.....	77
Figure 4.23 Trajectories of the points at the wafers over time under different rotation conditions (revolution-rotation).....	79
Figure 4.24 Comparison between the deposition rate distributions under different rotation conditions.	81

Figure 4.25 Standard deviation distribution under different revolution and rotation conditions.	83
Figure 4.26 Standard deviation map under different revolution and rotation conditions.	85
Figure 4.27 GaN deposition rate distribution under different carrier gas compositions: N0 H30, N10 H20, N20 H10, N30 H0.	88
Figure 4.28 Deposition rate distributions along the radial direction from the inlet with different carrier gas compositions: N0 H30, N10 H20, N20 H10, N30 H0.	89
Figure 4.29 Deposition thickness distributions along the radial direction from the inlet with different carrier gas compositions: N0 H30, N10 H20, N20 H10, N30 H0.	91
Figure 4.30 Standard deviations of the deposition thickness under different carrier gas composition conditions	92
Figure 4.31 Surface morphology taken from the center of the sapphire wafers of P2, P4 and P6 by 3D laser measuring microscope (white scale bar is 320 μm).	94
Figure 4.32 The density of the hillocks at the GaN surface grown under: (a) 1193 K and (b) 1223 K.	96

Figure 4.33 Deposition rate distribution at different temperatures: (a) 1193 K; (b) 1223 K. 98

Figure 4.34 Deposition rate distribution along the radial direction at 1193 K and 1223 K. 98

Figure 4.35 Deposition rate distribution along the radial direction at different temperatures: (a) 1193 K; (b) 1223 K. 100

Figure 4.36 The comparison between the hillock distribution and the deviation of the deposition rate along the radial direction for P2, P4 and P6 at: (a) 1193 K; (b) 1223 K..... 103

Figure 4.37 Flow velocity vector distributions and deposition rate distributions at 1223 K under different rotation speeds: (a) flow velocity vector distribution at the horizontal symmetry plane under 5 RPM; (b) flow velocity vector distribution at the horizontal symmetry plane under 15 RPM; (c) deposition rate distribution under 5 RPM; (d) deposition rate distribution under 5 RPM..... 107

Figure 4.38 Deposition rate distribution along the rotation direction at different rotation speeds: (a) 5 RPM; (b) 15 RPM..... 108

Figure 4.39 The comparison of standard deviation of deposition rate along the rotation direction between 5 RPM and 15 RPM..... 109

Figure 4.40 Optimal operating parameters for high thickness uniformity along the radial direction in the newly developed 6-inch wafer HVPE device..... 113

Figure 4.41 Optimal operating parameters for shortest processing time in the newly developed 6-inch wafer HVPE device.	116
Figure 5.1 Schematic diagram of multi-layer simulation model.	122
Figure 5.2 Deposition rate distribution at different susceptors. (Only S1, S4 and S7 are shown in the figure)	124
Figure 5.3 Velocity vector distribution at the horizontal cross section of GaCl & SiH ₄ holes from susceptor 1 to susceptor 7.	127
Figure 5.4 Velocity vector distribution at the horizontal cross section of NH ₃ holes from susceptor 1 to susceptor 7.	129
Figure 5.5 Velocity vector distribution at vertical cross section.....	132
Figure 5.6 Flow velocity magnitude distribution in front of GaCl and NH ₃ holes from bottom to top.	133
Figure 5.7 Flow velocity magnitude distribution in front of N ₂ holes from bottom to top.....	133
Figure 5.8 Deposition rate distributions at the different susceptors.....	135
Figure 5.9 GaCl mass fraction distribution at 1mm above the susceptors ...	137
Figure 5.10 GaCl mass fraction distribution and NH ₃ mass fraction at vertical cross section along the radial direction in front of the gas holes.	139
Figure 5.11 GaCl mass fraction distribution and NH ₃ mass fraction at vertical cross section in the middle of two adjacent gas holes.....	141

Figure 5.12 Experimental results of deposition rate distributions along the radial direction from susceptor 1 to susceptor 7.....	143
Figure 5.13 Calculation results of deposition rate distributions along the radial direction from susceptor 1 to susceptor 7.....	143
Figure 5.14 Experimental results of deposition thickness distributions along the radial direction from susceptor 1 to susceptor 5.	145
Figure 5.15 Calculation results of deposition rate distributions along the radial direction from susceptor 1 to susceptor 5.....	145
Figure 5.16 Comparison of the standard deviation of the deposition thickness between the calculation results and experimental results at different susceptors.	147
Figure 5.17 (a) Backflow velocity vector distribution at the outlet. (b) The GaCl mass distribution at the outlet.....	149
Figure 5.18 The N ₂ mass fraction distribution at horizontal cross section: (a) S7 (b) S1.....	150
Figure 5.19 Calculated V-III ratio along the radial direction from susceptor 1 to susceptor 5.....	152
Figure 5.20 Surface morphology of GaN thin film from susceptor 1 to susceptor 5.....	154

List of Tables

Table 2.1 Reaction examples of the species H ₂ , H ₂ O, CO, CO ₂ , O ₂ , and N ₂ ..	25
Table 4.1 Major conditions in the calculation.....	43
Table 4.2 Physical properties of gases and susceptor employed in the calculation.	44
Table 4.3 Standard deviation under different operating parameters in the newly developed 6-inch wafer HVPE device.....	114
Table 4.4 Processing time under different operating parameters in the newly developed 6-inch wafer HVPE device.	118
Table 5.1 Major conditions in the calculation	123
Table 5.2 Physical properties of gases and susceptors employed in the calculation	125

Chapter 1. Introduction

1.1 Background

Gallium nitride (GaN) has a direct band gap which is widely used in the LED (light emitting diodes) and LD (laser diodes) fabrication [1-3]. After the excellent work and numerous contributions from the Nichia Corporation's research team [4-8], the GaN growth method has received a lot of attentions from many research groups and companies. During few past decades, GaN thin film growth technology has tremendously developed because of its wide band gap well applicable to laser diodes (LDs) and light emitting diodes (LEDs) [9-11].

At present, high nitrogen pressure solution growth (HNPSG) is feasible to grow the bulk GaN crystal, metal-organic chemical vapor deposition (MOCVD) and hydride vapor phase epitaxy (HVPE) are feasible to produce the GaN film. Among them, only HNPSG has the ability to produce the dislocation-free GaN single crystal and the directional growth experiment has been conducted by M. Bockowski and etc [12]. But this method seems not to be a hot topic across the commercial LED companies due to its harsh conditions such as high temperature of 2000 K and high pressure of 2 GPa. Meanwhile, the GaN film grown by MOCVD based on the trimethylgallium (TMGa) has a good quality with a much lower cost in comparison with HNPSG. Thus this method is favored in LED product application. Also,

because of the widespread use of MOCVD such as TiN deposition, grapheme deposition, GaAs deposition, it has been studied very thoroughly during the past years [13-17].

Recently, the constantly increasing illuminating LED market (shown in the figure 1.1) demands a more cost-effective way to produce the GaN film. Until now, due to the limitation of the feasible method to grow bulk GaN with large dimension and high purity, epitaxy is the most popular method to fabricate the GaN thin film. Among the epitaxy methods, Hydride vapor phase epitaxy (HVPE) is widely employed to produce the GaN template for the LED chips [18]. Considering that the cost effectiveness of LED light bulb is the key factor to replace the traditional lamp, improving the efficiency of energy consumption, HVPE equipment capable of producing high quality of GaN on large sapphire wafer with high throughput is urgently required to improve the competitiveness of LED application [19]. Therefore, a multi-wafer HVPE equipment has been produced. Accordingly, the studies on the multi-wafer HVPE equipment have a great significance to the LED industries.

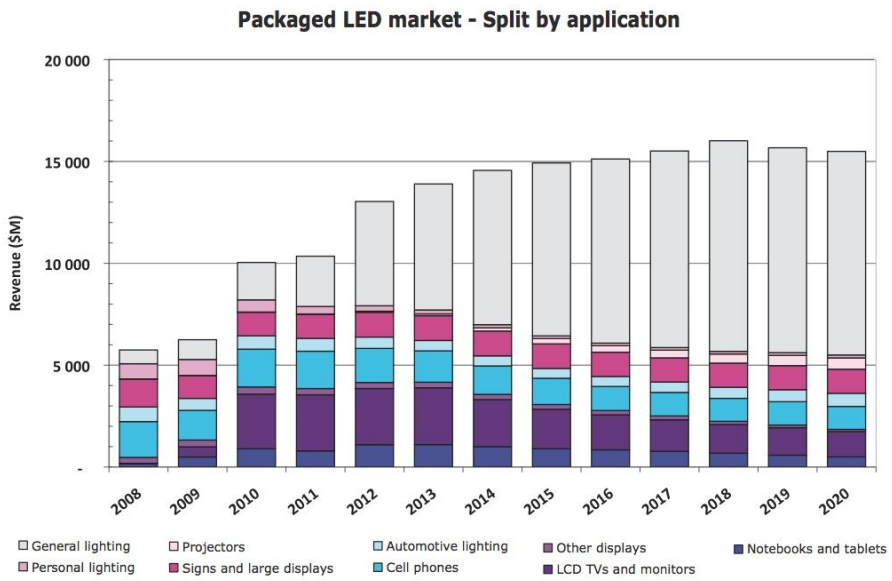


Figure 1.1 Packaged LED market trend. [20]

1.2 GaN bulk crystal growth method

1.2.1 High nitrogen pressure solution growth (HNPSG)

The HNPSG method can be traced back to the early 1980s when Karpinski carried out the research under 20 kbar and at temperature up to 1700°C [21, 22]. The results show that the undoped layer contains less nitrogen vacancies than that achieved by CVD. Subsequently, Grzegory has successfully made improvement at growth rate and morphological stability and analyzed the mechanisms of crystallization of bulk GaN obtained by HNPSG in his work [23-27]. Due to the low growth rate and limited crystal dimension, the GaN bulk crystal prepared by HNPSG has been used for the substrate of HVPE GaN and recently, Bockowski has published his experimental and calculation results on this process [12, 28-30].

The advantage of HNPSG gives the credit to the high crystalline quality and a low dislocation density of elaborated GaN. However, the pressure about 1-2 GPa as well as the temperature of 1500°C can be reached only with a very limited and expensive equipment (figure 1.2), which restricts the commercial application for producing bulk GaN.

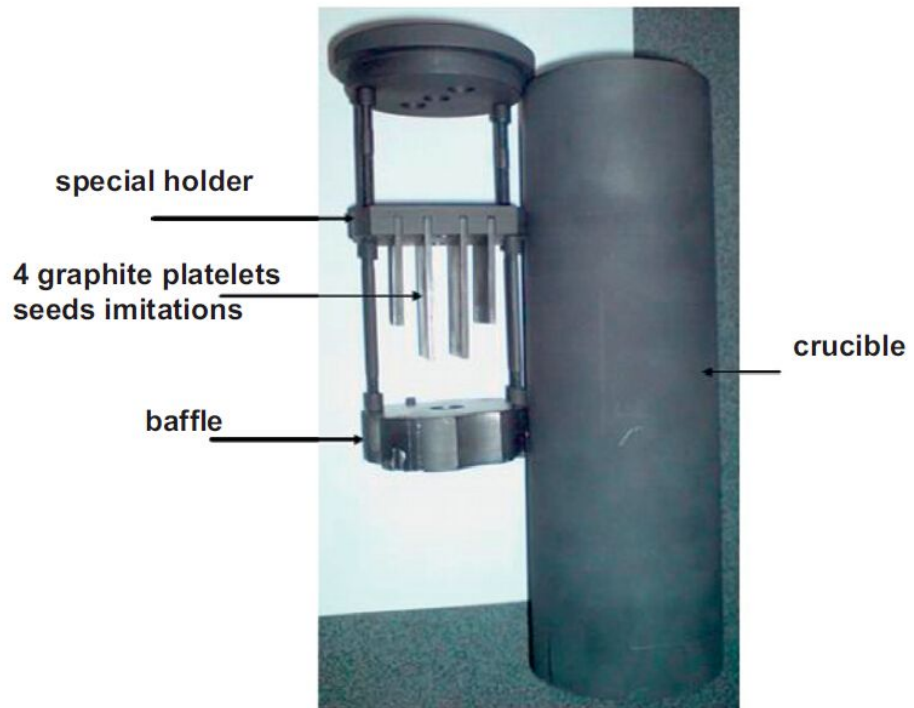


Figure 1.2 Photograph of the HNPSG equipment. [29]

1.2.2 Na-flux method

Na flux method is one of the popular methods to grow the GaN crystal. Yamane et al. assert that GaN single crystal can be grown using Na flux at 600-800 °C [31-33]. In the Na flux experiments, sodium azide and gallium are introduced into a stainless steel container in the argon atmosphere. Then the container is sealed and placed in the furnace, which is shown in the figure 1.3. When the temperature is above 300 °C, NaN_3 decomposed into high purified Na and N_2 , which provides N source to the GaN crystal. The needless sodium can be eliminating by washing with ethanol. The experiments are conducted under a pressure between 5 and 10 MPa during 24 to 96 h [34]. Especially, wurtzite type gallium nitride has been observed for high molar ratio of sodium [31].

Some important issues in developing Na flux process are as following: First, the stainless steel tube used as a container for Na-Ga melt could react with the high temperature melt. So a boron nitride crucible has been employed in the experiment to prevent the reaction between the crucible and the melt [35]. Second, the pressure decreases with time due to the consumption of nitrogen. Consequently, the duration of the crystal growth experiments and crystal size are limited [36].

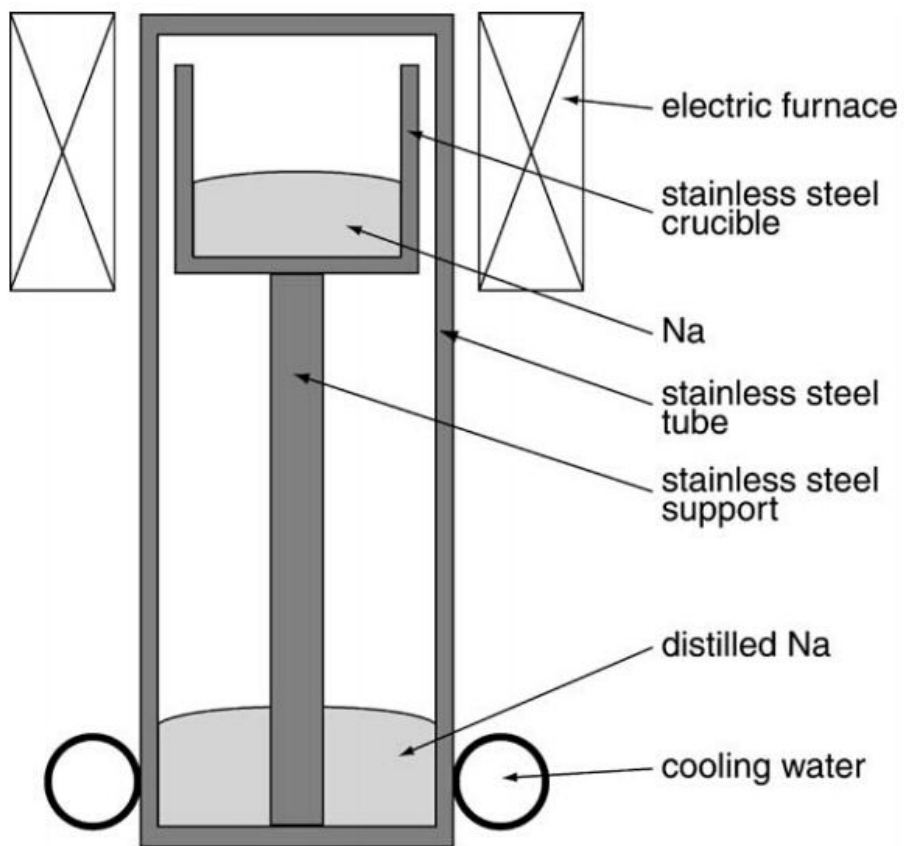


Figure 1.3 Schematic diagram of the Na flux method. [33]

1.2.3 Ammonothermal method

In the middle of 1990s, Dwilinski et al published many studies [37-39] on the ammonothermal synthesis of gallium nitride. GaN synthesis is feasible in supercritical ammonia at a temperature 500 °C and a pressure in the range of 400-500 MPa [34]. A mineralizer such as lithium or potassium amide is required. The crystalline quality highly depends on the ratio of NH₃ in the mineralizer. For a lower molar ratio (LiNH₂:NH₃), only the surrounding of the Ga grains is converted in GaN, leading to irregular gray particles [31]. Recently, NH₄F has been proved to be a promising mineralizer for the ammonothermal method crystal growth of GaN. The configuration of the ammonothermal GaN growth using NH₄F as mineralizer is shown in the figure 1.4 [10]. Numerical model is also an efficient tool to analyze ammonothermal GaN growth [40, 41]. Though the temperature and pressure required in the experiment are moderate, the growth rate of this method is still very low [42].

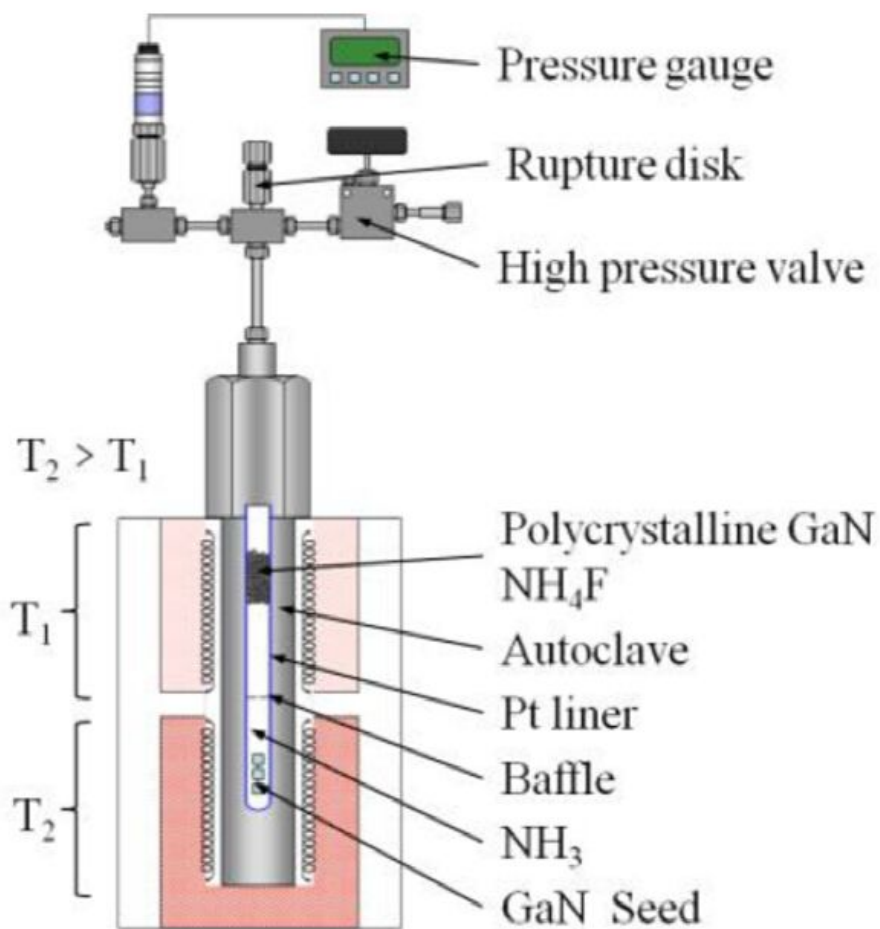


Figure 1.4 Experimental configuration of ammonothermal GaN growth. [10]

1.3 GaN thin film growth method

1.3.1 Metalorganic chemical vapor deposition (MOCVD)

The first successful MOCVD growth of high-quality III-V films was reported by Amano et al., who employed an RF-heated atmospheric-pressure reactor [43]. Later, many researchers have prepared high-quality GaN film produced by MOCVD [44-47]. In order to provide a good comprehension of MOCVD equipment, CFD simulations have been widely used in the previous studies [48-51]. Besides, GaAs and AlN are also widely fabricated by MOCVD [43, 52-55]. Generally, the chemical reaction is in the form of $R_3M(g) + EH_3(g) \rightarrow ME(s) + 3RH(g)$, where M is belong to the Column III metal element such as Ga, Al or In, R is an organic radical such as CH_3 or C_2H_5 . E is a Column V element [56]. The great advantage of using metalorganics is that they are volatile at moderately low temperatures. There are no liquid Ga or In sources in the reactor to control for transport to the substrate. With pyrolysis reaction insensitive to temperature, MOCVD allows for efficient and reproducible deposition. However, the growth rate is low that usually less than $5 \mu\text{m/h}$ [57]. Additionally, despite its excellent application in the industries, the cost of the equipment is also expensive.

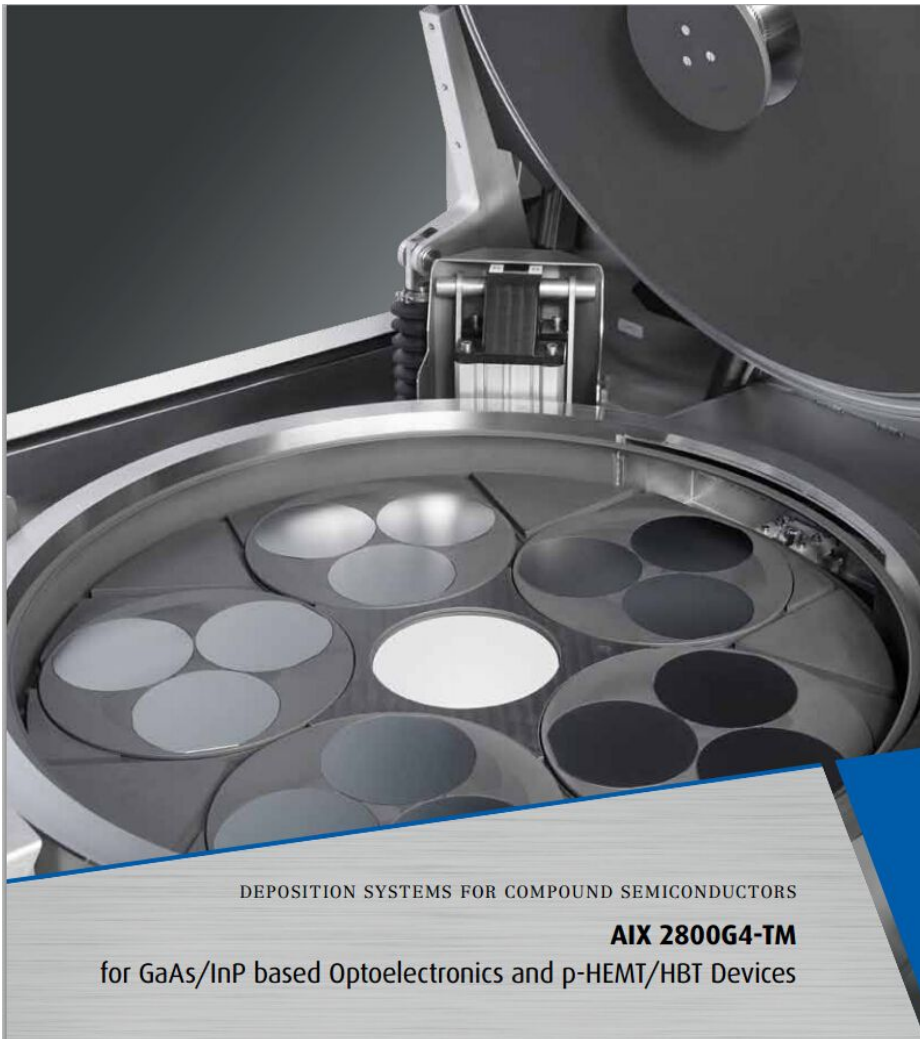


Figure 1.5 Photo of MOCVD equipment produced by Aixtron. [58]

1.3.2 Hydride vapor phase epitaxy (HVPE)

HVPE has played an important historical role before 1980s, which is the most popular method of gallium nitride growth [59]. However, this technology has been almost abandoned since early 1980s due to its unavoidable inability to reduce the defect and incapability of P-type doping [60]. Since the successful fabrication of GaN blue LED by Nakamura et al. [5-7, 61], HVPE method to grow GaN has drawn attentions again [62-69]. Due to a relatively high growth rate ($>100\mu\text{m/h}$) and a possibility to crystallize high-quality and high-purity material, HVPE is the best candidate to produce the GaN substrate [69]. In a common HVPE equipment as shown in the figure 1.6, HCl gas reacts with molten Ga, forming GaCl gas, which provides the Ga atom source. At the same time, NH_3 is piped into the equipment and reacts with GaCl at the surface of the wafers. N_2 or H_2 is usually employed as a carrier gas to increase the quality of the GaN film. Then, the unnecessary gases flow away from the exhaust. The temperature of the experiment is between 950°C to 1050°C . And the pressure is atmospheric pressure or lower.

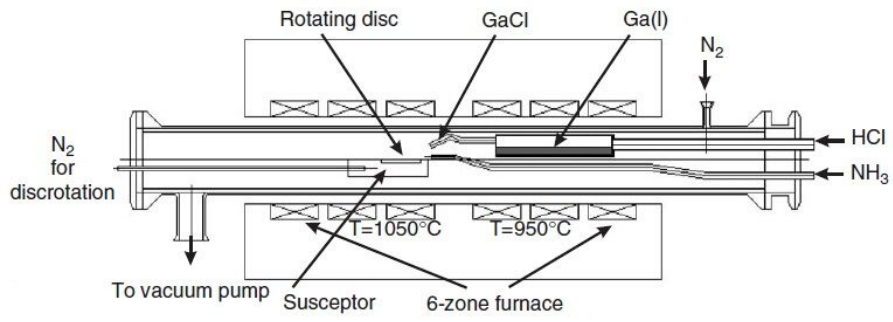


Figure 1.6 Schematic diagram of hydride vapor phase epitaxy. [70]

1.4 Aims of HVPE research

Many researches on HVPE have been published before, from the atomic scale simulation [71-78], molecular-dynamics study [79-84] to computer fluid dynamics (CFD) [13, 70, 85-88]. Especially for the CFD calculation, previous studies have provided considerable insights into the effect of the equipment geometry [88, 89], the effect of the temperature [90], the effect of the carrier gas [86] and the effect of the GaCl synthesis reaction [70]. Most of them are focusing on the experimental stage other than mass production stage. Thus we hope that our work will make a distribution to help people think about the method to improve the quality of the mass production by HVPE. In traditional HVPE equipment, there are usually two pipes to transport the reacting gases, and sometimes the carrier gas is input through another pipe [91]. Alternatively, reacting gases can be mixed with the carrier gas to deposit. In order to improve the uniformity of the deposition thickness at the wafer, the wafer is rotated with the susceptor. And through the remarkable studies on the traditional HVPE equipment, a nice uniformity of GaN thin film can be controlled. To increase the productivity, a new HVPE equipment with 7 susceptors and with 6 wafers at each susceptor has been developed. However, the uniformity of the thickness and the surface morphology of GaN thin film are much more difficult to control than the traditional HVPE equipment. Therefore, the purpose of this study is to

improve the uniformity of the thickness and the surface morphology of GaN thin film through computational and experimental analysis.

Chapter 2. Numerical modeling

2.1 Flow

2.1.1 Mass conservation

Conservation of mass requires that the time rate of change of mass in a control volume be balanced by the net mass flow into the same control volume (outflow - inflow). This can be expressed as:

$$\frac{\partial \rho}{\partial t} + \nabla \cdot (\rho \vec{V}) = 0 \quad (2-1)$$

The first term on the left hand side is the time rate of change of the density (mass per unit volume). The second term describes the net mass flow across the control volume's boundaries and is called the convective term. [92]

2.1.2 Momentum conservation

Newton's second law states that the time rate of change of the momentum of a fluid element is equal to the sum of the forces on the element. The x-component of the momentum equation is found by setting the rate of change of x-momentum of the fluid particle equal to the total force in the x-direction on the element due to surface stresses plus the rate of increase of x-momentum due to sources:

$$\frac{\partial(\rho u)}{\partial t} + \nabla \cdot (\rho \vec{V} u) = \frac{\partial(-p + \tau_{xx})}{\partial x} + \frac{\partial\tau_{yx}}{\partial y} + \frac{\partial\tau_{zx}}{\partial z} + S_{Mx} \quad (2-2)$$

Similar equations can be written for the y- and z-components of the momentum equation:

$$\frac{\partial(\rho v)}{\partial t} + \nabla \cdot (\rho \vec{V} v) = \frac{\partial\tau_{xy}}{\partial x} + \frac{\partial(-p + \tau_{yy})}{\partial y} + \frac{\partial\tau_{zy}}{\partial z} + S_{My} \quad (2-3)$$

$$\frac{\partial(\rho w)}{\partial t} + \nabla \cdot (\rho \vec{V} w) = \frac{\partial\tau_{xz}}{\partial x} + \frac{\partial\tau_{yz}}{\partial y} + \frac{\partial(-p + \tau_{zz})}{\partial z} + S_{Mz} \quad (2-4)$$

In these equations, p is the static pressure and τ_{ij} is the viscous stress tensor. [92]

2.1.3 Navier-Stokes equations

The momentum equations given above, contain as unknowns the viscous stress components τ_{ij} , therefore a model must be provided to define the viscous stresses.

In Newtonian flows, the viscous stresses are proportional to the deformation rates of the fluid element. The nine viscous stress components (of which six are independent for isotropic fluids) can be related to velocity gradients to produce the following shear stress terms:

$$\tau_{xx} = 2\mu \frac{\partial u}{\partial x} - \frac{2}{3}u(\nabla \cdot \vec{V}) \quad (2-5)$$

$$\tau_{yy} = 2\mu \frac{\partial v}{\partial y} - \frac{2}{3}u(\nabla \cdot \vec{V}) \quad (2-6)$$

$$\tau_{zz} = 2\mu \frac{\partial w}{\partial z} - \frac{2}{3}u(\nabla \cdot \vec{V}) \quad (2-7)$$

$$\tau_{xy} = \tau_{yx} = \mu \left(\frac{\partial u}{\partial y} + \frac{\partial v}{\partial x} \right) \quad (2-8)$$

$$\tau_{xz} = \tau_{zx} = \mu \left(\frac{\partial u}{\partial z} + \frac{\partial w}{\partial x} \right) \quad (2-9)$$

$$\tau_{yz} = \tau_{zy} = \mu \left(\frac{\partial v}{\partial z} + \frac{\partial w}{\partial y} \right) \quad (2-10)$$

Substitution of the above shear stress terms into the momentum equations yields the Navier-Stokes equations [92]:

$$\begin{aligned} \frac{\partial(\rho u)}{\partial t} + \nabla \cdot (\rho \vec{V} u) = & -\frac{\partial p}{\partial x} + \frac{\partial}{\partial x} \left[2\mu \frac{\partial u}{\partial x} - \frac{2}{3} \mu (\nabla \cdot \vec{V}) \right] \\ & + \frac{\partial}{\partial y} \left[\mu \left(\frac{\partial u}{\partial y} + \frac{\partial v}{\partial x} \right) \right] + \frac{\partial}{\partial z} \left[\mu \left(\frac{\partial u}{\partial z} + \frac{\partial w}{\partial x} \right) \right] + S_{Mx} \end{aligned} \quad (2-11)$$

$$\begin{aligned} \frac{\partial(\rho v)}{\partial t} + \nabla \cdot (\rho \vec{V} v) = & -\frac{\partial p}{\partial y} + \frac{\partial}{\partial x} \left[\mu \left(\frac{\partial u}{\partial y} + \frac{\partial v}{\partial x} \right) \right] \\ & + \frac{\partial}{\partial y} \left[2\mu \frac{\partial v}{\partial x} - \frac{2}{3} \mu (\nabla \cdot \vec{V}) \right] + \frac{\partial}{\partial z} \left[\mu \left(\frac{\partial v}{\partial z} + \frac{\partial w}{\partial y} \right) \right] + S_{My} \end{aligned} \quad (2-12)$$

$$\begin{aligned} \frac{\partial(\rho w)}{\partial t} + \nabla \cdot (\rho \vec{V} w) = & -\frac{\partial p}{\partial z} + \frac{\partial}{\partial x} \left[\mu \left(\frac{\partial u}{\partial y} + \frac{\partial v}{\partial x} \right) \right] \\ & + \frac{\partial}{\partial y} \left[\mu \left(\frac{\partial v}{\partial z} + \frac{\partial w}{\partial x} \right) \right] + \frac{\partial}{\partial z} \left[2\mu \frac{\partial w}{\partial y} - \frac{2}{3} \mu (\nabla \cdot \vec{V}) \right] + S_{Mz} \end{aligned} \quad (2-13)$$

By rearranging these equations and moving the smaller contributions of the viscous stress terms to the momentum source term, we can rewrite the Navier-Stokes equations in a more useful form [92]:

$$\frac{\partial(\rho u)}{\partial t} + \nabla \cdot (\rho \vec{V} u) = -\frac{\partial p}{\partial x} + \nabla \cdot (\mu \nabla u) + S_{Mx} \quad (2-14)$$

$$\frac{\partial(\rho v)}{\partial t} + \nabla \cdot (\rho \vec{V} v) = -\frac{\partial p}{\partial y} + \nabla \cdot (\mu \nabla v) + S_{My} \quad (2-15)$$

$$\frac{\partial(\rho w)}{\partial t} + \nabla \cdot (\rho \vec{V} w) = -\frac{\partial p}{\partial z} + \nabla \cdot (\mu \nabla w) + S_{Mz} \quad (2-16)$$

2.2 Heat Transfer

Heat transfer processes are computed by solving the equation for the conservation of energy. This equation can take several forms and CFD-ACE+ numerically solves the energy equation in the form known as the total enthalpy equation. This form is fully conservative and is given in equation (2-17).

$$\begin{aligned}
 \frac{\partial(\rho h_0)}{\partial t} + \nabla \cdot (\rho \vec{V} h_0) = & \nabla \cdot (k_{eff} \nabla T) + \frac{\partial p}{\partial t} \\
 & + \left[\frac{\partial(u\tau_{xx})}{\partial x} + \frac{\partial(u\tau_{yx})}{\partial y} + \frac{\partial(u\tau_{zx})}{\partial z} \right] \\
 & + \left[\frac{\partial(u\tau_{xy})}{\partial x} + \frac{\partial(u\tau_{yy})}{\partial y} + \frac{\partial(u\tau_{zy})}{\partial z} \right] \\
 & + \left[\frac{\partial(u\tau_{xz})}{\partial x} + \frac{\partial(u\tau_{yx})}{\partial y} + \frac{\partial(u\tau_{zx})}{\partial z} \right] + S_h
 \end{aligned} \tag{2-17}$$

Where h_0 is the total enthalpy and is defined as

$$h_0 = i + \frac{p}{\rho} + \frac{1}{2}(u^2 + v^2 + w^2) \tag{2-18}$$

Where i is the internal energy and is a function of the state variables r and T , P is the static pressure and τ_{ij} is the viscous stress tensor. k_{eff} is the effective thermal conductivity of the material. In laminar flow, this will be the thermal conductivity of the fluid, k . In turbulent flows:

$$k_{eff} = K + \frac{\mu_t C_p}{\sigma_t} \quad (2-19)$$

Where σ_t is the turbulent Prandtl number.

S_h contains terms for additional sources due to reactions, radiation, spray, body forces, etc. [92]

2.3 Chemical reaction

2.3.1 Composition variables

Several different composition variables are used for flow with mixing or reaction. The mass fraction of species i in a multi-component system, Y_i , is defined as the mass of the i th species per unit mass of the mixture. Similarly, the mole fraction x_i is defined as the number of moles of the i th species per mole of the mixture. The mole and mass fractions are related to each other by the molecular weight of the i th species, M_i , and the mixture molecular weight, M .

$$x_i = \frac{Y_i M}{M_i} \quad (2-20)$$

The mixture molecular weight is given by:

$$M = \frac{1}{\sum (Y_i/M_i)} = \sum (x_i/M_i) \quad (2-21)$$

The molar concentration of species i , c_i , is defined as the number of moles of the i th species per unit volume. It is related to Y_i as:

$$c_i = \frac{\rho Y_i}{M_i} \quad (2-22)$$

Where ρ , the mixture density, is computed from the equation of state. The number density ($\# / \text{m}^3$) of a species i is obtained by multiplying the molar concentration with Avogadro's number ($6.023 \times 10^{23} / \text{mol}$). The number of moles of species i per unit mass, n^i , is defined as:

$$n_i = \frac{Y_i}{M_i} \quad (2-23)$$

It is a useful quantity in converting concentration units, as can be seen by examining equations 2-20 through 2-22. The partial pressure of species i in a mixture of gases is defined as [92]:

$$P_i = x_i P \quad (2-24)$$

2.3.2 Chemical rate expressions

A system of N_{rxn} chemical reactions involving N_{sp} species can be expressed in a general notation by:

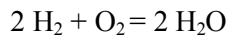
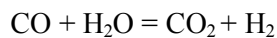
$$\sum_{i=1}^{N_{sp}} v'_{ij} \varphi_i = \sum_{i=1}^{N_{sp}} v''_{ij} \varphi_i, j = 1, \dots, N_{rxn} \quad (2-25)$$

where φ_i is the chemical symbol for species i , v'_{ij} and v''_{ij} are the forward and reverse stoichiometric coefficients for the i th species in the j th reaction. Equation 2-25 can be written more compactly as:

$$\sum_{i=1}^{N_{sp}} v_{ij} \varphi_i = 0, j = 1, \dots, N_{rxn} \quad (2-26)$$

where $v_{ij} = v''_{ij} - v'_{ij}$. The chemical reaction must be balanced. The stoichiometric coefficients are integers for elementary reactions and are normally 0, 1, or 2. Elementary reactions usually involve no more than four species, so the array of stoichiometric coefficients is sparse.

The nomenclature given above is illustrated in the following example. A system containing the species H_2 , H_2O , CO , CO_2 , O_2 , and N_2 may have the following reactions:



For this system the stoichiometric coefficients for the above reactions are shown in the table 1

φ_i	v'_{i1}	v'_{i2}	v''_{i1}	v''_{i2}
H ₂	0	2	1	0
H ₂ O	1	0	0	2
CO	1	0	0	0
CO ₂	0	0	1	0
O ₂	0	1	0	0
N ₂	0	0	0	0

Table 2.1 Reaction examples of the species H₂, H₂O, CO, CO₂, O₂, and N₂.

The molar production rate of species i due to chemical reaction is

$$\omega_i = \sum_{j=1}^{N_{rxn}} v_{ij} q_j \quad (2-27)$$

The rate-of-progress variable for the j th reaction, q_j , can be generally expressed as:

$$q_j = (k_f)_j \prod_{i=1}^{N_{sp}} c_i^{a'_{ij}} - (k_r)_j \prod_{i=1}^{N_{sp}} c_i^{a''_{ij}} \quad (2-28)$$

where: $(k_f)_j$ and $(k_r)_j$ are temperature-dependent forward and reverse rate coefficients. a'_{ij} and a''_{ij} are constants.

For elementary reactions which obey the mass action law:

$$a'_{ij} = v'_{ij} \quad (2-29)$$

$$a''_{ij} = v''_{ij} \quad (2-30)$$

Where: v'_{ij} and v''_{ij} are the stoichiometric coefficients defined in equation 2-25. The concentration exponents in equation 2-28 are not necessarily related to the stoichiometric coefficients for global reaction.

The rate coefficients are assumed to have an Arrhenius form:

$$k_f = AT^n (P/P_{atm})^m e^{-E_a/RT} \quad (2-31)$$

Where:

A = pre-exponential constant

n = temperature exponent

E_a/R = activation temperature

m = exponent on pressure dependency

The units of the reaction rate given by equation 2-28 are (moles / volume / time). The units of A , therefore, depends on the exponents of the molar concentrations in equation 2-28. In other words, for a simple reaction of form:



the rate of the reaction is expressed:

$$\dot{\omega} = A_p T^n (P/P_{atm})^m e^{-E_a/RT} [A]^\alpha [B]^\beta \quad (2-33)$$

where $\dot{\omega}$ is expressed in kmoles / (m³ s). The units on A_p are dependent upon α , β , and n as shown below:

$$\text{units of } A_p = \frac{m^{3\alpha+3\beta-3}}{\text{kmol}^{(\alpha+\beta-1)}sK^n} \quad (2-34)$$

The reverse rate coefficient can be obtained from the equilibrium constant, K_c , for reactions obeying the law of mass action:

$$K_r = \frac{K_f}{K_c} \quad (2-35)$$

The equilibrium constant (actually a function of temperature) can be calculated from thermodynamic data:

$$\ln(K_c)_j = \left(\sum_{i=1}^{N_{sp}} \nu_{ij} \right) \ln \frac{p_0}{RT} - \sum_{i=1}^{N_{sp}} (\nu_{ij} \frac{g_i^0}{RT}) \quad (2-36)$$

where P_0 is reference pressure of one atmosphere, g_i^0 is Gibbs free energy of species i at one atmosphere. [92]

2.3.3 Surface reaction models

The surface reaction models allow the calculation of deposition, etching, or catalytic reaction at surfaces. The surface reaction provides a boundary condition for the mass fractions of species in the fluid, rather than a source term in the transport equations. The general form of the surface reaction considered in CFD-ACE+ is:

$$\sum_{i=1}^{N_g} a'_{ij} A_i + \sum_{i=1}^{N_s} b'_{ij} B_i(s) + \sum_{i=1}^{N_b} c'_{ij} C_i(b) = \sum_{i=1}^{N_g} a''_{ij} A_i + \sum_{i=1}^{N_s} b''_{ij} B_i(s) + \sum_{i=1}^{N_b} c''_{ij} C_i(b) \quad (2-37)$$

where:

a_{ij} = gas species stoichiometric coefficient

b_{ij} = adsorbed species stoichiometric coefficient

c_{ij} = bulk species stoichiometric coefficient

N_g = total number of gas-phase species

N_s = total number of adsorbed species

N_b = total number of bulk (deposited) species

For this reaction, the surface reaction rate may be expressed as:

$$\dot{S}_j = k_{fj} \prod_{i=1}^{N_g} [A_i]_w^{a'_{ij}} \prod_{i=1}^{N_s} [B_i(s)]^{b'_{ij}} - k_{rj} \prod_{i=1}^{N_g} [A_i]_w^{a''_{ij}} \prod_{i=1}^{N_s} [B_i(s)]^{b''_{ij}} \quad (2-38)$$

where:

k_{fj} = forward rates

k_{rj} = reverse rates

As seen from the above expression, the surface reaction rate is assumed to be independent of the concentration of the bulk species. The gas-phase concentrations at the surface are expressed as:

$$[A_i]_w = \frac{\rho_w Y_i^w}{M_i} \quad (2-39)$$

and the surface concentrations are expressed as:

$$[B_i(s)]_w = \rho_s X_i \quad (2-40)$$

Where

ρ_w = gas -phase mass density in kg/m³

ρ_s = surface site density in kmol/m²

Y_i^w = gas-phase mass fractions adjacent to the wall

X_i = surface site fractions

A species flux balance at the reacting surface yields

$$J_{i,n} = M_i \sum_j (a''_{ij} - a'_{ij}) \dot{S}_j \quad i = 1, \dots, N_g \quad (2-41)$$

$$\frac{d[B_i(s)]}{dt} = \sum_j (b''_{ij} - b'_{ij}) \dot{S}_j \quad i = 1, \dots, N_s \quad (2-42)$$

where, the left-hand side of equation 2-41 is the diffusive flux of species i normal to the surface and the right-hand side of equation 2-41 is the

production rate of species i per unit area of surface, on a mass basis. Equation 2-41 and equation 2-42 are solved by coupled Newton-Raphson iterations. The reaction flux can be computed by using two different approaches, namely the sticking coefficient method and the general rate method. The sticking coefficient method evaluates the production rate based on sticking probability and precursor thermal flux, while the finite-rate chemistry uses the kinetic expression to evaluate the reaction rate.

For sticking coefficient expression, surface reaction rate equation 2-38 becomes:

$$\dot{S}_j = \gamma_j j_{A,th} \prod_{i=1}^{N_s} [X_i]^{b'_{ij}} \quad (2-43)$$

where sticking probability is expressed in Arrhenius form and the thermal flux of precursor species A is [92]

$$j_{A,th} = \sqrt{\frac{1}{2\pi M_A R T_w}} [A]_w \quad (2-44)$$

2.4 Mixture fractions

Flows with mixing or reaction can be calculated by solving transport equations for the mass fraction of all (or all but one) species. The number of variables needed to calculate the flow can be reduced, in certain cases, by introducing variables referred to as mixture fractions. A mixture is defined as a combination of species with a fixed composition.

Each mixture is tracked with a mixture fraction variable, which is governed by the general transport equation

$$\frac{\partial}{\partial t}(\rho f_k) + \frac{\partial}{\partial x_j}(\rho u_j f_k) = \frac{\partial}{\partial x_j} \left(\Gamma \frac{\partial f_k}{\partial x_j} \right) + (\dot{m}_k)_{evap} \quad (2-45)$$

In the preceding equation f_k represents the mixture fraction for the k th mixture. Note that this equation contains no source terms due to chemical reaction. The only source term is due to the evaporation of spray droplets. The diffusion coefficient (Γ) is the same for all mixture fractions.

Mixture fractions are normally associated with one or more inlet boundaries and normalized such that the value is 1 for the boundaries associated with that mixture and 0 for other boundaries. A mixture fraction is also associated with the evaporating spray droplets. With this convention, the sum of mixture fractions over all defined mixtures is unity. Since the mixture fractions sum to unity, $K - 1$ mixture fraction equations will have to be solved when K mixtures are defined.

Equation 2-45 is linear in f_k and, therefore, also applies to linear combinations of the mixture fractions. The overall continuity equation is recovered by summing equation 2-45 over all mixtures. Let ξ_{jk} denote the mass fraction of the i th species in the k th mixture. It is easily shown that when equation 2-45 is multiplied by ξ_{jk} for each mixture fraction and summed over all mixture fractions, the following equation is obtained.

$$\frac{\partial}{\partial t}(\rho Y_i) + \frac{\partial}{\partial x_j}(\rho u_j Y_i) = \frac{\partial}{\partial x_j} \left(\Gamma \frac{\partial Y_i}{\partial x_j} \right) + (\dot{m}_i)_{evap} \quad (2-46)$$

Where

$$Y_i = \sum \xi_{ik} f_k \quad (2-47)$$

This is the transport equation for the mass fraction of a non-reacting species, showing that composition can be calculated from the mixture fractions using equation 2-47 when the diffusion coefficients of all species are equal. The boundary conditions for the mixture fractions are defined such that the boundary conditions for the mass fractions are satisfied by equation 2-47 as well. The effect of mass diffusivity differences among different species is negligible in most turbulent flows at moderate to high Reynolds numbers (convection-driven flows). The use of mixture fractions normally reduces the number of variables to be solved because the number of mixtures is usually less than the number of species. Mixture fractions are also used with certain reaction models to calculate the composition of reacting flows. [92]

Chapter 3. Experiments

A new design of multi-wafer HVPE equipment is used to deposit the GaN epi-layer in our experiments. As shown in the figure 3.1, six 6-inch wafers are placed on the susceptor, the reacting gases and carrier gas are transported from the center pipe and flow out through the peripheral wall. To increase the throughput, the susceptor is designed large enough to hold many wafers. Compared to the single-wafer equipment, the control of the uniformity of the deposition thickness in all of the wafers becomes more difficult. Since the susceptor is very large, the wafers near the nozzle deposit more quickly than the wafers far away from the nozzle due to the transport phenomena. The similar phenomena are also presented in the conventional equipment [17, 86-88]. With the increase of the susceptors size, the transport effect becomes more obvious and the uniformity becomes much lower. To overcome the transport effect, carrier gas is utilized to dilute and transport the reacting gases. Actually, the method to introduce the carrier gas is diverse: carrier gas can be injected separately from reacting gases [90]; carrier gas can be also mixed into reacting gases [87]. Besides, the geometry of the gas pipes has an effect on the distribution of the gas species [88]. In our experiments, with other conditions constant, flow rate of carrier gas, temperature, pressure, susceptor rotation speed, wafer rotation speed and carrier gas composition are changed respectively to investigate how the operating parameters influence on the GaN deposition thickness. The thickness of the GaN deposition is measured by the

epi-layer thickness mapping device named PL+A310, which exploits the interference phenomena of the crystal surface and the interface between the crystal and substrate. To reduce the cost of the experiment, 6-inch wafer is replaced by the three 2-inch wafers in a row as shown in the figure 3.2. Besides, the surface morphology of GaN thin film is observed through the OLS4000 3D laser measuring microscope.

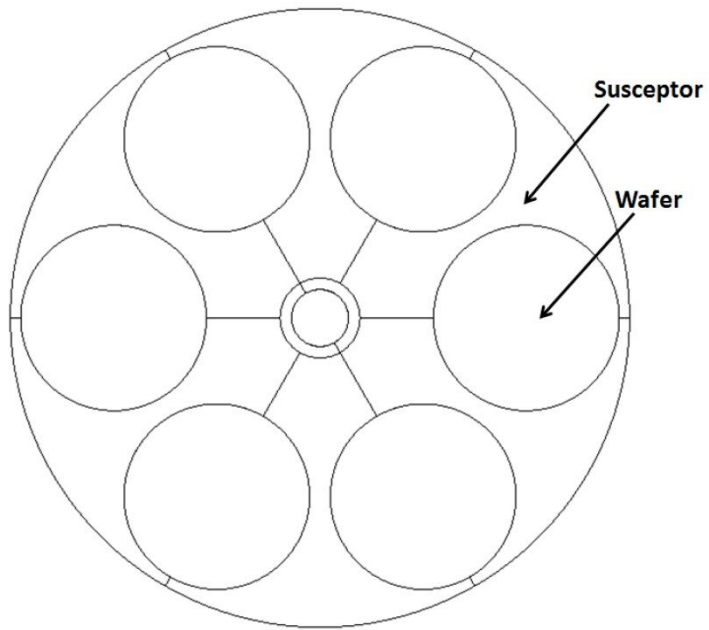


Figure 3.1 Schematic configuration of the equipment from the top view.

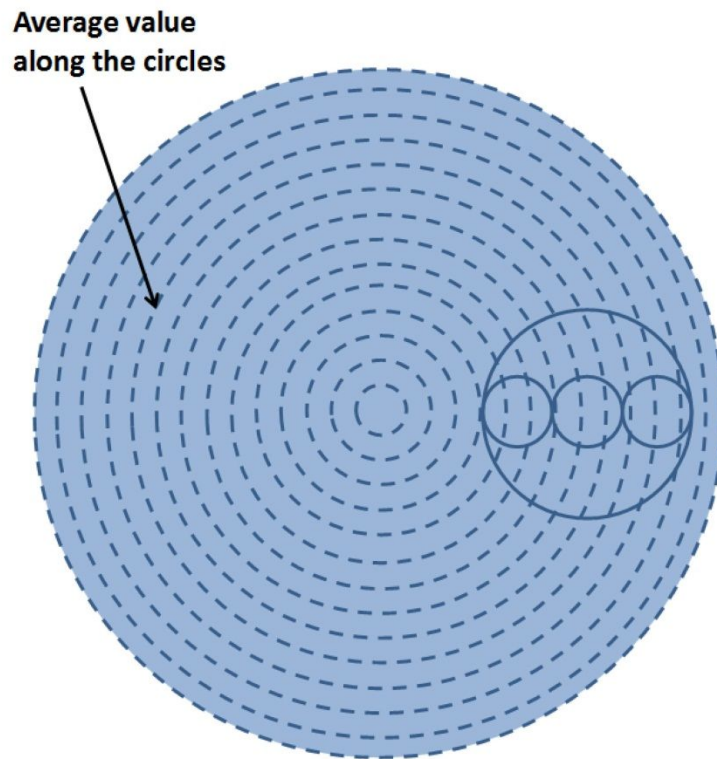


Figure 3.2 Method of measuring the thickness distribution.

Chapter 4. Four-way nozzle design

4.1 Introduction

4.1.1 Deposition uniformity

From previous studies, it is found that many factors could affect the growth of GaN film in the HVPE equipment, which include design parameter and operating parameter [89, 93, 94]. In the present study, we focused on the operating parameters such as flow rate, temperature, pressure, susceptor rotation speed, wafer rotation speed and composition of carrier gas. According to the thermodynamic analysis [15], it is known to us that the low reaction temperature causes slow reaction rate which can be simply derived from the equation of the reaction rate. On the contrary, quite high temperature decreases the probability of the Ga adsorption on the GaN site, and therefore too high temperature or too low temperature could not meet the efficiency requirements of the mass production. Thus, we select only a small range of temperature applicable in the mass production from 1173 K to 1273 K.

4.1.2 Surface morphology

When the number or the size of the wafers is increased, not only the non-uniformity of the deposition thickness becomes severer, [93, 95] but also the surface morphology becomes more difficult to control [96]. Surface morphology is extremely important since the rough interface will result in poor device performance [97, 98]. Among the surface defects frequently occurring at III-V semiconductors, hillocks have been investigated in many previous studies [97, 99-103]. A.R.A Zauner asserted that the misorientation of substrate caused the hillock formation by comparing the surface morphology of GaN grown on different oriented GaN substrates [99]. Moreover, according to T. B. Wei [100], the radius of the spiral is huge due to a high growth rate and a great strain. F. Oehler also have meticulously observed the hillocks, concluding that the formation of hillocks is linked to the screw dislocation [101]. Through the cathodoluminescence (CL) and atomic force microscopy (AFM) measurements, K. Zhou believes that a larger strain field around a dislocation cluster than a single dislocation may be the reason for hillock formation [97]. Pawel Kempisty asserts that the non-uniformity of the growth rate may also lead to significant strains in GaN material [15]. The strains related phenomena in GaN thin film also has been studied By Kisielowski [104].

In this study, hillocks have been observed at the surface of GaN thin film grown by HVPE. It is found that the density of the hillocks increases

along the radial direction from the center to the periphery. As stated by the previous study, the hillocks are closely related to the screw dislocation [100, 101, 105]. In order to explore the factor resulting in the high density of screw dislocation, a steady 3D numerical simulation has been conducted. The calculation results and experimental results show an explicit correlation between the density of hillocks and the deposition rate change, which provides support for the opinion that non-uniformity of the growth rate may also lead to significant strain. Moreover, through the comparison of the deviations of deposition rate between different rotation speeds, it is predicted that high susceptor rotation speed will decrease the density of the hillocks.

4.2 Model description

Since the deposition and reaction occurred at high temperature in a hermetic chamber, the phenomenon is hard to investigate by experiments, the analysis work is implemented by the CFD software CFD-ACE, which is widely used in the modeling of epitaxy [106, 107]. The simulation domain is including the susceptors, wafers and gas inlets and outlets. The model is made of 316545 unstructured grids (figure 4.1). Since the actual experiment is conducted under a long time at a constant temperature and pressure, steady state was assumed in the simulation.

To make the calculation more efficient, some assumptions have been made: 1) Considering the temperature differences within the susceptor are very small, the temperature of the whole equipment is set as constant. 2) The depositions occur not only at the wafers but also at the susceptor according to the observation of the experiments, and both of the GaN deposition rates are regarded as same value. 3) Gas phase reaction including the decomposition of NH_3 and the formation of NH_4Cl has not been considered due to their effects are not obvious in the previous study [87]. 4. Turbulence would not be included due to the maximum Reynolds number is 1514.74.

The surface chemical reactions are employed based on the quasi-thermodynamics suggested by Segal and Karpov [15, 87, 108-111]. There are two surface reactions which have been involved in this model:



The CFD-ACE database [92] and previous study have been taken as reference for the data of surface reaction in this model. [87, 112]

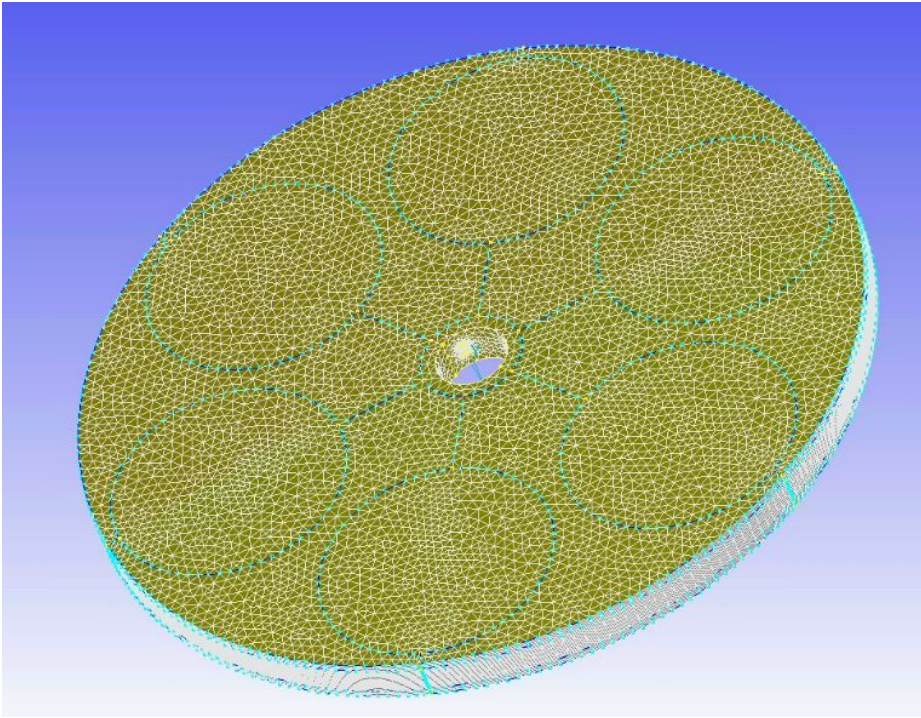


Figure 4.1 Schematic diagram of multi-wafer HVPE equipment.

4.3 Simulation conditions

4.3.1 Boundary conditions

The calculations under different carrier gas flow rates, temperatures, pressures, susceptor rotation speeds, wafer rotation speeds and carrier gas compositions are conducted as shown in the table 4.1. The conditions in bold type are the standard constant parameters when other parameters are changed. The gases are fed from the inlets at the center with a constant volume per minute at a constant pressure. The outer wall of the model is designated as adiabatic wall. The gravity is 9.8 m/s^2 .

Carrier gas flow rate	Temperature	Pressure	Susceptor rotation speed	Wafer rotation speed	Carrier gas composition (N ₂ fraction)
7 slm	1173K	0.3 Bar	0 rpm	-40 rpm	0
13 slm	1223K	0.6 Bar	5 rpm	~	0.333
19 slm	1273K	1 Bar	10 rpm	40 rpm	0.667
30 slm			15 rpm		1

Table 4.1 Major conditions in the calculation.

4.3.2 Volume conditions

Table 4.2 shows the physical properties of the gases and susceptor. The specific property of each gas involved in the calculation refers to the CFD-ACE database. The properties of the mixture of the gases are calculated from each gas species by the methods in the table 4.2. The gases are regarded as compressible fluid that ideal gas law is employed. The susceptor is made up of quartz, the properties of which are also shown in the table 4.2.

	Density	Heat capacity	Thermal conductivity	Viscosity	Mass diffusivity
Gases	Ideal gas law	Mix JANAF method	Mix kinetic theory	Mix kinetic theory	Schmidt number 0.7
Susceptor	2200 kg / m ³	670 J / (kg • K)	1.4 W / (m • K)	-	-

Table 4.2 Physical properties of gases and susceptor employed in the calculation.

4.4 Results and discussion

4.4.1 Operating parameter effect

4.4.1.1 Carrier gas flow rate effect

Effect of carrier gas flow rate on uniformity is investigated. With other conditions constant, we change the carrier gas flow rate from 7 slm to 30 slm. The deposition rate distributions at the susceptor have been shown in figure 4.2. The pink color presents high deposition rate while blue color present low deposition rate. The deposition rate pattern is 4-fold symmetrical because the reacting gases are fed through 4 directions. Then the deposition rates of the GaN layer on the wafers along the radius from the end near the center to the peripheral end have been recorded in the figure 4.3. In the same way, the data from calculation is also plotted in the same figure to make a comparison. From the experimental result in the figure 4.3, we can conclude that the 30 slm flow rate of carrier gas has a better uniformity than that of 7 slm. Though carrier gas with the large flow rate diluting the reacting gases causes the significant decrease of the deposition rate, the uniformity improvement is quite inspiring.

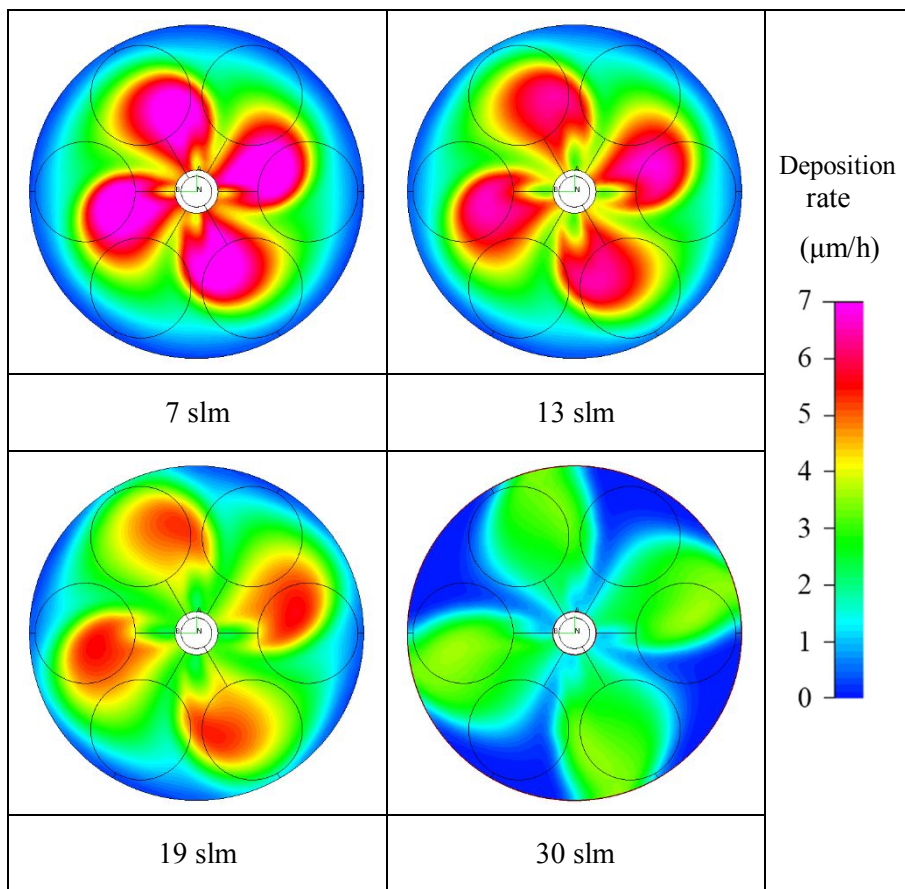


Figure 4.2 GaN deposition rate distributions under different carrier gas flow rates: 7 slm, 13 slm, 19 slm, 30 slm.

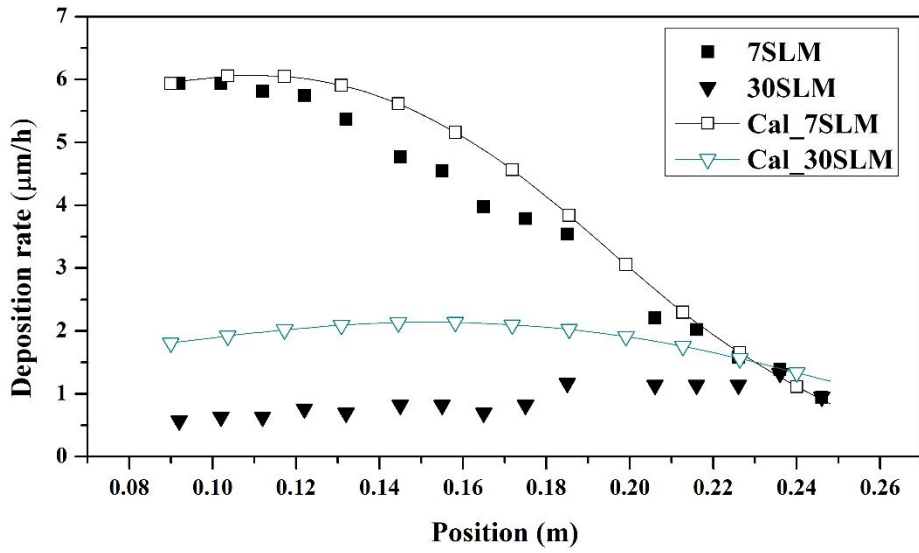


Figure 4.3 Comparison of experimental result and calculation result with carrier gas flow rate of 7 slm and 30 slm.

For the target thickness of the GaN thin layer is $4\mu\text{m}$ in our experiment, with the same average thickness of $4\mu\text{m}$, the deposition thickness distributions of four different carrier gas flow rates are compared in the figure 4.4. In these results, the maximum values do not always appear at the position nearest to the gas inlets and the minimum values do not always appear at the most distant position from the inlets, so we could not simply compare the nearest and farthest value. In contrast, as shown in figure 4.5, we use standard deviation to evaluate the uniformity of the deposition thickness which can reflect the whole distribution of the thickness. From the deviation results, it is observed that although there is a gap between the standard deviation of the experiment result and calculation result, both of them still reflect a same trend. In a word, in the range of the carrier gas flow rate from 7 slm to 30 slm, the larger carrier gas flow rate decreases the deviation. In another word, the larger carrier gas flow rate increases the uniformity.

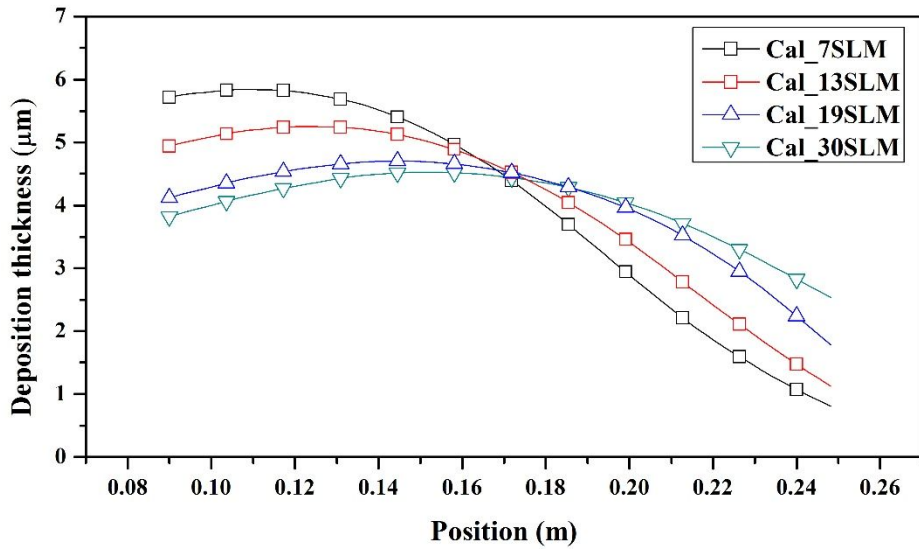


Figure 4.4 Deposition thickness distributions along the radial direction from the inlet with different flow rates of carrier gas: 7slm, 13slm, 19slm, 30slm.

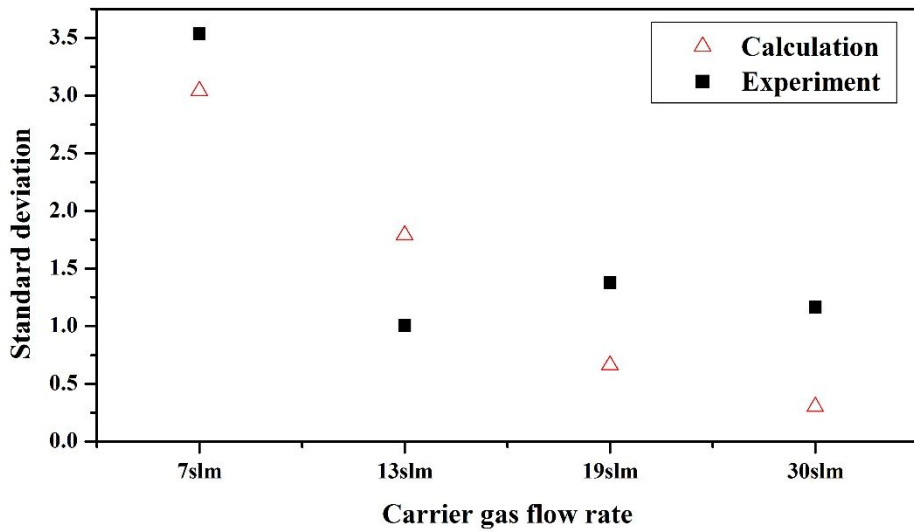


Figure 4.5 Standard deviations of the deposition thickness under different carrier gas flow rate conditions.

To study the effect of carrier gas on the epitaxial layer thickness, we collected the mass fraction distributions of NH_3 and GaCl at 1mm above the susceptors. Since the situations of the mass fraction profiles along the radial direction in front of the nozzle and the mass fraction profiles along the direction in the middle of two adjacent nozzles are different, these two cases are discussed. Figure 4.6(a) shows that along the inlet direction, GaCl mass fraction at the susceptors surface first increases then decreases. To clearly explain the reason, we can divide this process into 3 parts: a) before the maximum value, since GaCl is injected from the inlet with a certain initial velocity, it moves forward instead of sinking to the surface of the susceptor. Thus the mass fraction at the surface of the susceptor is small; b) around the maximum value, with the effect of diffusion and convection as well as the velocity of the gases becoming smaller, GaCl , which is heavier than other gases, starts to sink making the mass fraction at the surface increase; c) after reaching the maximum value, the reaction consumes a lot of GaCl , as the distance increasing, the continuous reduction of the amount of GaCl appears.

By the influence of a larger amount of carrier gas, the mass fraction peak position is slightly migrated to the right. This phenomenon occurs because not only GaCl is diluted further by the carrier gas, but also initial velocity of GaCl has been increased by the larger amount of carrier gas. Thus GaCl can spread to distant locations and sinks. Then a more uniform distribution of GaCl could be achieved by increasing the carrier gas.

Therefore, it is fair to say that the GaCl mass fraction distribution is quite similar with the GaN deposition rate distribution. It is seen from figure 4.6(b) that the effect of the carrier gas on NH₃ only reduces the concentration of NH₃. Because NH₃ is relatively excessive compared to the GaCl, the influence of the NH₃ on the deposition rate is not great.

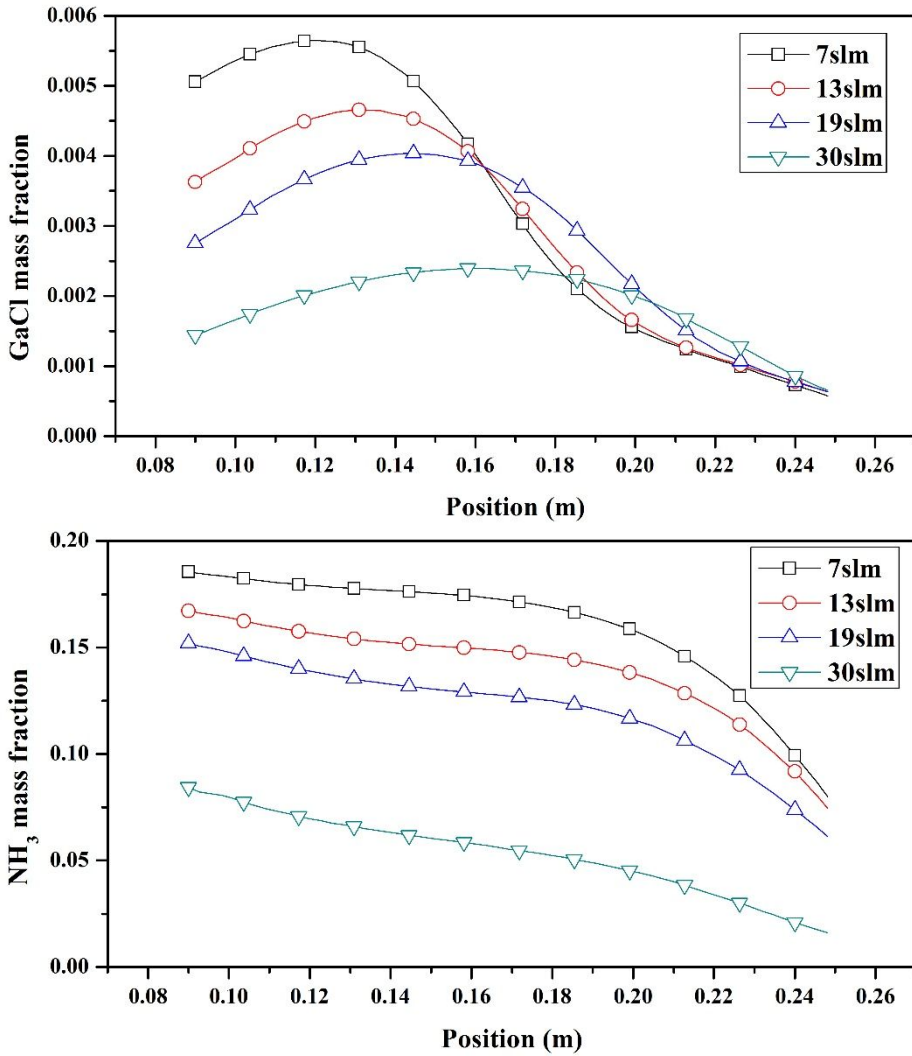


Figure 4.6 Mass fraction distributions of the species along the inlet direction:
 (a) GaCl; (b) NH₃.

Correspondingly, in figure 4.7(a), by analyzing the direction in the middle of the two adjacent inlets, we can achieve similar conclusion: with the

increase of the carrier gas flow rate, the GaCl mass fraction decreases, and the peak value moves toward right. For figure 4.7(a) and 4.7(b), the only difference from 4.6(a) and 4.6(b) is that both of the GaCl and NH₃ profiles show more flat trend due to the inexistence of gas directly flowing from inlet with high velocity. There are some gases flowing across the susceptor due to the rotation and others flow back due to the relatively low pressure compared to the radial direction in front of the nozzles. Therefore, the effect of the carrier gas flow rate on the uniformity of GaCl and NH₃ mass fraction along the direction in the middle of two adjacent nozzles is not obvious.

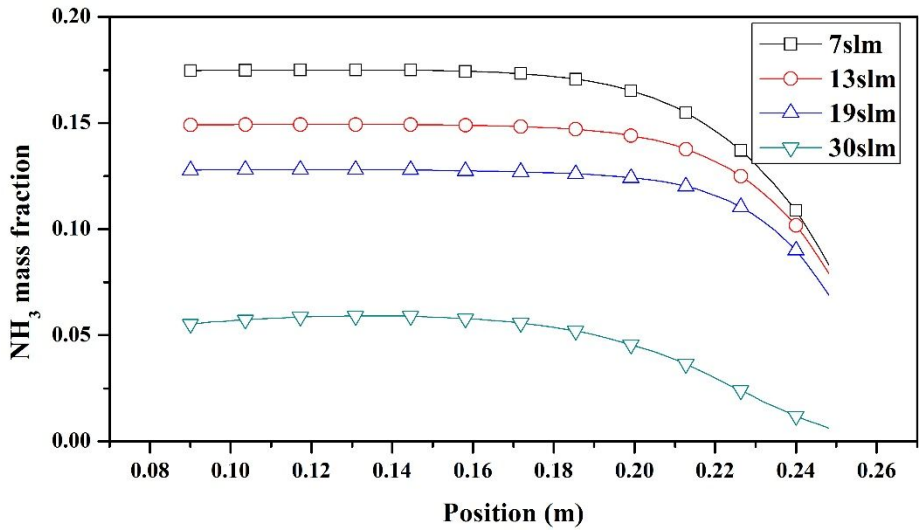
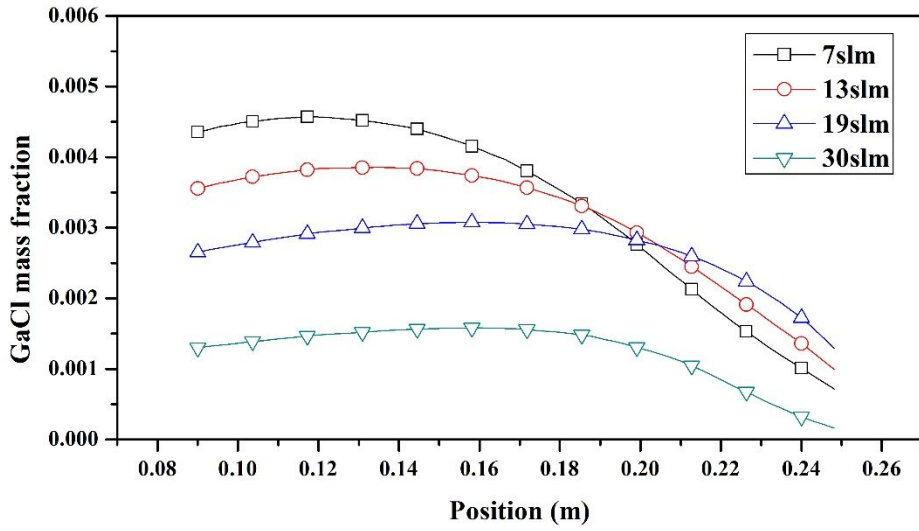


Figure 4.7 Mass fraction distributions of the species along the direction in the middle of the two adjacent inlets: (a) GaCl; (b) NH₃.

4.4.1.2 Temperature effect

Experimental results show that the operating temperature is also among the important factors that affect the uniformity. So the temperature effect is also studied by the calculations. Since the temperature in the furnace is almost same according to the experimental measurement by the thermocouple, we do not have to consider the different temperature at different position. However, we should evaluate the different operating temperature effect on the uniformity. So at the optimum carrier gas flow rate of 30 slm, operating temperature is changed from 1173 to 1223 K and 1273 K to conduct the simulation. Since the calculation results are in accordance with the experimental results in the previous section, the calculation results of different operating temperatures are also credible. Moreover, in this calculation, temperature ranges only from 1173 K to 1273 K that the decrease of Ga adsorption rate and NH_3 decomposition by the high temperature are not considered. Additionally, the formation of NH_4Cl due to the low temperature does not have to be considered, either. Instead, how the operating temperature affects the convection, diffusion rate, gas expansion and deposition rate has been researched.

Firstly, from a theoretical analysis, the temperature rise will change the volume of the gases. In the actual process, the gases are injected into the device with a constant volume per unit time at a fixed temperature and

pressure. Therefore, if the temperature is higher, the flow velocity is higher according to the ideal gas law, $PV=nRT$. It is also demonstrated by the calculation result. In the temperature condition of 1173 K, 1223 K and 1273 K, the maximum velocities at the gas inlet are 11.56 m/s, 12.05 m/s, 12.54 m/s, respectively.

Secondly, the diffusion coefficient Γ in this calculation has been calculated by the equation:

$$\Gamma = \frac{\mu}{\sigma} \quad (4-3)$$

Where σ is the Schmidt number which has been designated as a constant number. μ , the viscosity of the gases, is calculated by the mix kinetic theory:

$$\mu_i = 2.6693 * 10^{-5} \frac{\sqrt{MW_i T}}{\delta_i^2 \Omega_{\mu}} \quad (4-4)$$

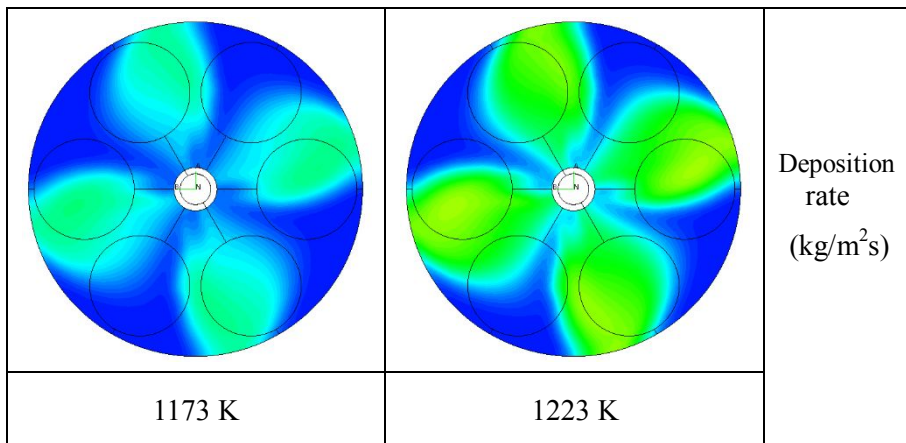
Where μ_i is dynamic viscosity of species i, MW_i is molecular weight of species i, T is the temperature, δ_i is the characteristic diameter of the molecule. Ω is the collision integral. The viscosity of the gas species μ_i is proportional to the square root of temperature T, and the diffusion coefficient Γ is also proportional to the gas species μ_i . So increasing the temperature would accelerate the diffusion process.

Thirdly, the temperature would also change the adsorption of the GaCl on the GaN site. The adsorption coefficient of GaCl is decided by the Arrhenius form:

$$\alpha_{\text{GaCl}} = 100 \exp(-17000/T) \quad (4-5)$$

From this equation, high temperature increases the adsorption coefficient.

Based on the above theory, the temperature effect has been analyzed. The deposition rate distributions under different temperatures have been obtained by the calculation in the figure 4.8. The deposition rate increases when the temperature increases due to the sticking coefficient increases in the equation 4-5. If the deposition rates are plot along the radial direction, it is clearly shown that the deposition rate increases with the increase of the



temperature (figure 4.9).

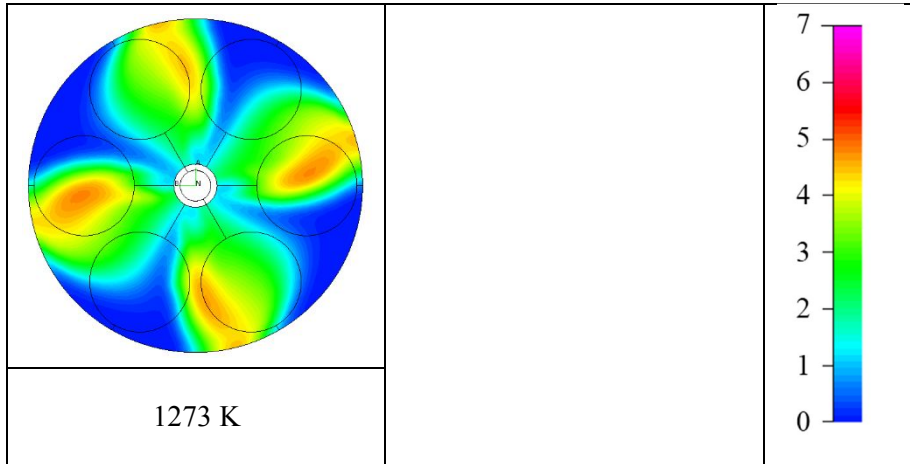


Figure 4.8 GaN deposition rate distribution under different temperature conditions: 1173 K, 1223 K, 1273K.

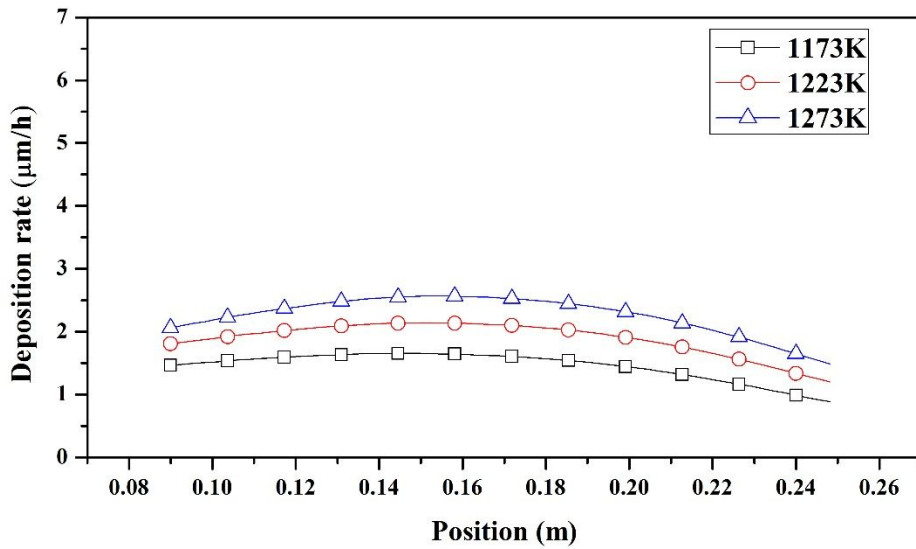


Figure 4.9 Deposition rate distributions along the radial direction from the inlet with different temperatures: 1173 K, 1223 K, 1273 K.

Moreover, the calculation results of deposition thickness distributions along the radial direction have been achieved in the figure 4.10. And the standard deviations from figure 4.11 show that the 1273 K has the best uniformity. In the figure 4.10, the three profiles of deposition thickness look similar. Moreover, the deposition thickness difference with different temperature conditions at the upstream section of the wafer is more notable than that at the downstream. To uncover the reason of the difference, GaCl mass fraction distributions along the radial direction with different temperatures are shown in the figure 4.12(a). The starting point and the ending point values normalized by dividing by the average mass fraction are plotted in the figure 4.12(b). In the figure 4.12(b), when the temperature increases, the normalized mass fraction decreases at the upstream section and increases at the downstream section. And the rate of change at the upstream section is larger than that at the downstream section (for example, left endpoint is 9.6%, right endpoint is 5.1%). Thus, the thickness difference at the upstream appears more notable than that at the downstream. Namely, the high temperature decreases the GaCl mass fraction at the upstream section more sharply than that at downstream section. This is because GaCl above the upstream section of the wafer is carried away by the carrier gas with a larger velocity at a higher temperature instead of descending on the wafer. So in this

equipment, with 30 slm carrier gas, 1273 K has a better uniformity compared to the lower temperature.

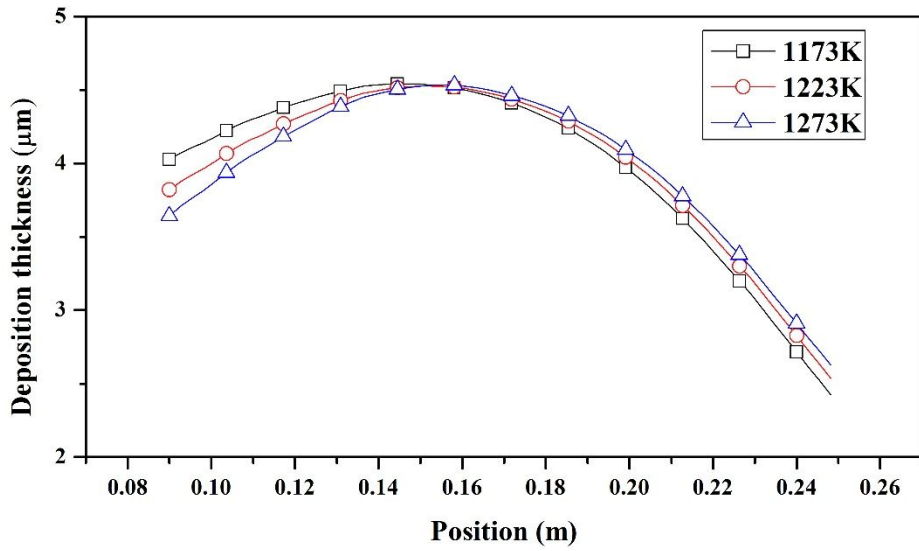


Figure 4.10 Deposition thickness distributions along the radial direction from the inlet with different temperatures: 1173 K, 1223 K, 1273 K.

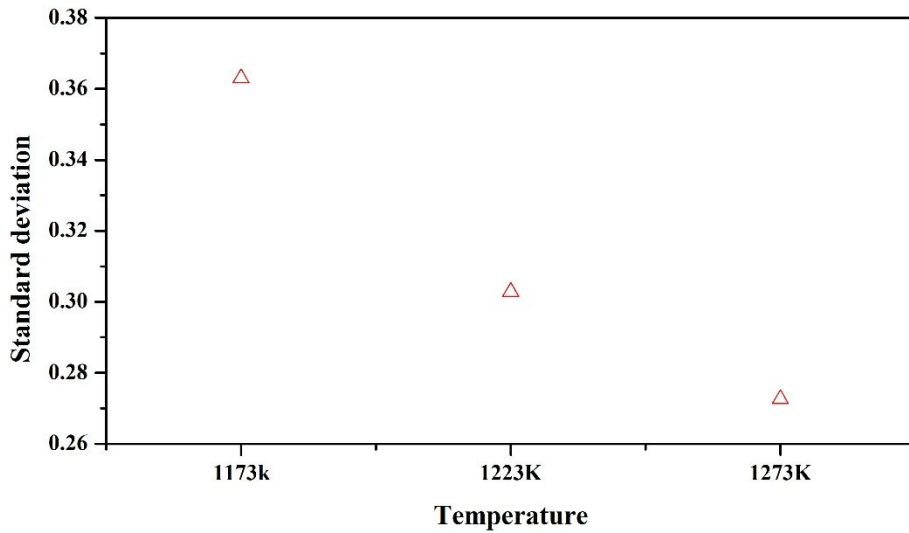


Figure 4.11 Standard deviations of the deposition thickness under different temperature conditions.

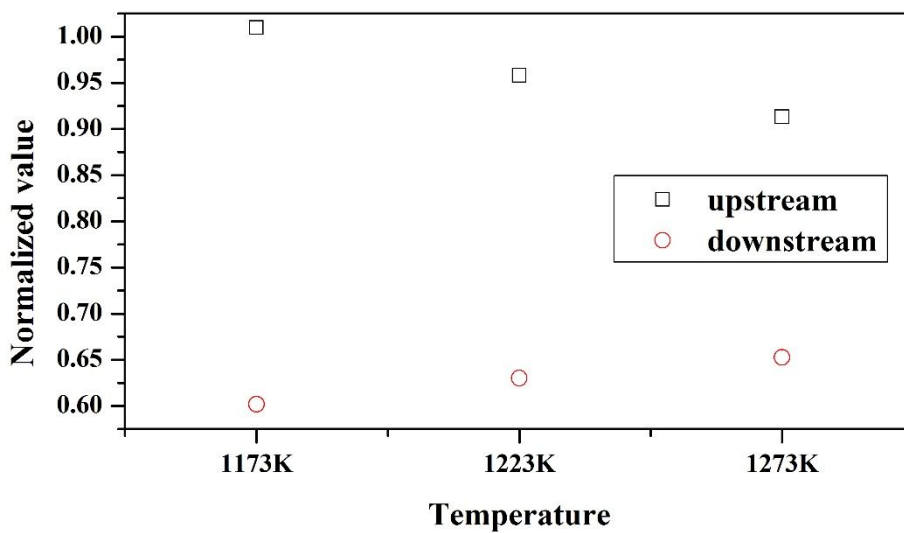
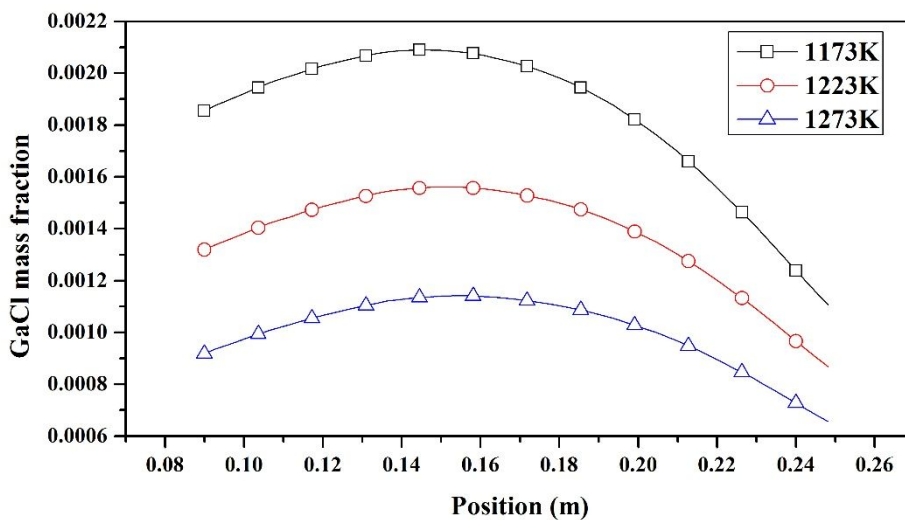


Figure 4.12 (a) GaCl mass fraction distributions along the radial direction; (b) normalized mass fractions at the upstream and the downstream with different temperatures.

4.4.1.3 Pressure effect

Pressure is among the most important operating parameters which could affect the uniformity of deposition thickness of GaN thin film produced by HVPE. According to the experimental and simulation study by L.Kdinski [49], not only the experiment results but also the calculation results prove that with the decrease of the pressure, the deposition rate significantly decreases. Though the deposition rate decreases, the uniformity of the thin film thickness will be improved by the low pressure.

In order to understand how the pressure affects the uniformity, three pressure conditions of 0.3 Bar, 0.6 Bar and 1 Bar are selected to conduct the calculations. It is observed from the figure 4.13 that the deposition rate of 1 Bar is clearly larger than that of 0.3 Bar and 0.6 Bar. By processing the data into the deposition rate distributions along the radial direction (figure 4.14), we can find that the deposition rate of high pressure is clearly larger than that of low pressure. If the same average deposition thickness of 4 μ m is achieved under different pressure conditions, the figure of the comparison of deposition thickness between different pressures will be attained (figure 4.15). In the figure 4.15, at the upstream section, the deposition thickness of low pressure is smaller than that of high pressure. However, at the downstream section, the deposition thickness of low pressure is larger than that of high pressure. Because at lower pressure, the GaCl gas will migrate further to descend due to

the diffusion. When the pressure is 0.3 Bar, the uniformity is significantly better than those of 0.6 Bar and 1 Bar. If the standard deviations of every single curve are compared (figure 4.16), it is noted that the uniformity is best when the pressure is 0.3 Bar, which means that low pressure could improve the uniformity of deposition thickness along the radial direction.

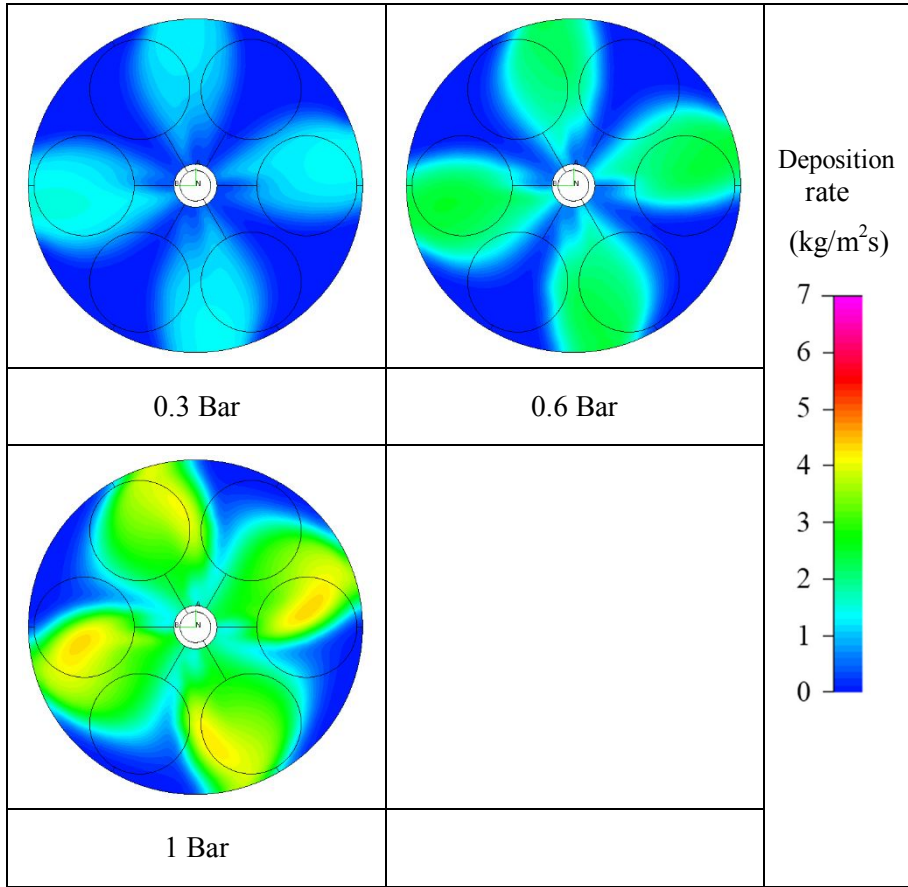


Figure 4.13 GaN deposition rate distribution under different pressure conditions: 0.3 Bar, 0.6 Bar, 1 Bar.

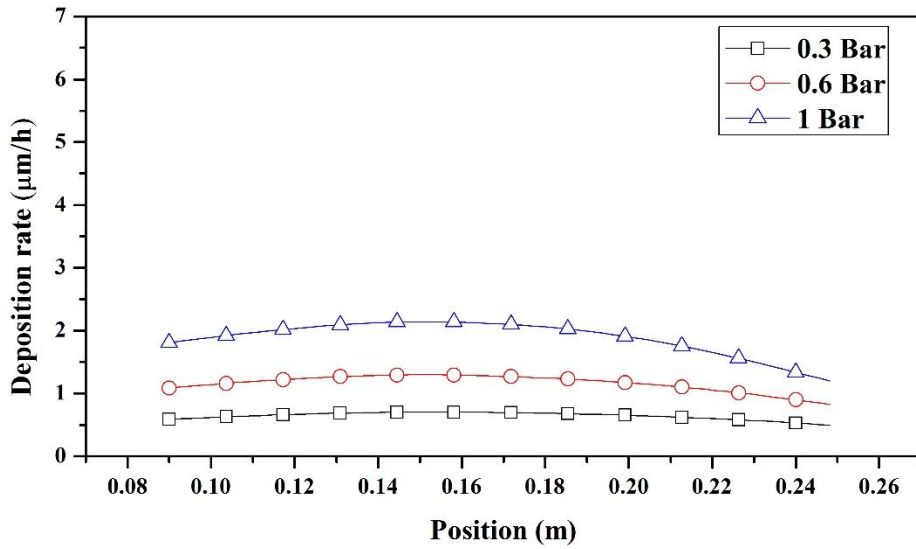


Figure 4.14 Deposition rate distributions along the radial direction from the inlet with different pressures: 0.3 Bar, 0.6 Bar, 1 Bar.

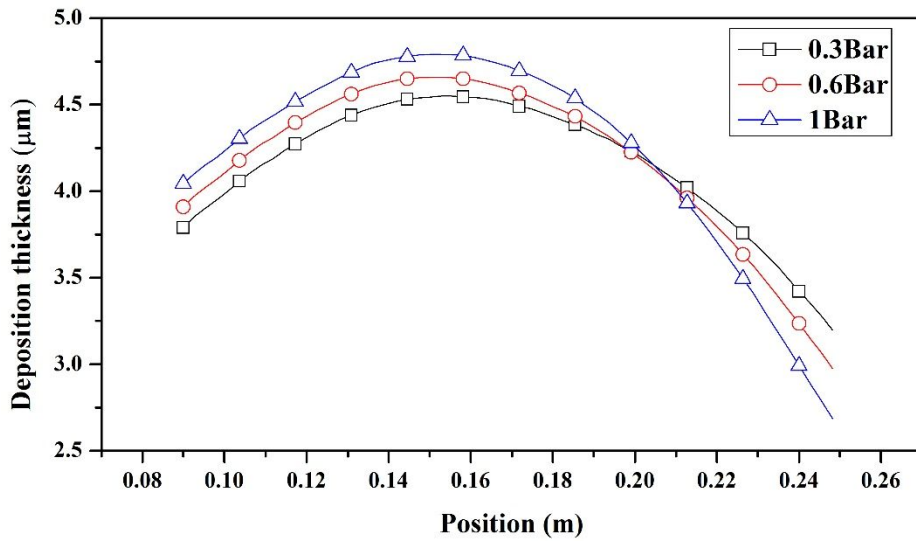


Figure 4.15 Deposition thickness distributions along the radial direction from the inlet with different pressures: 0.3 Bar, 0.6 Bar, 1 Bar.

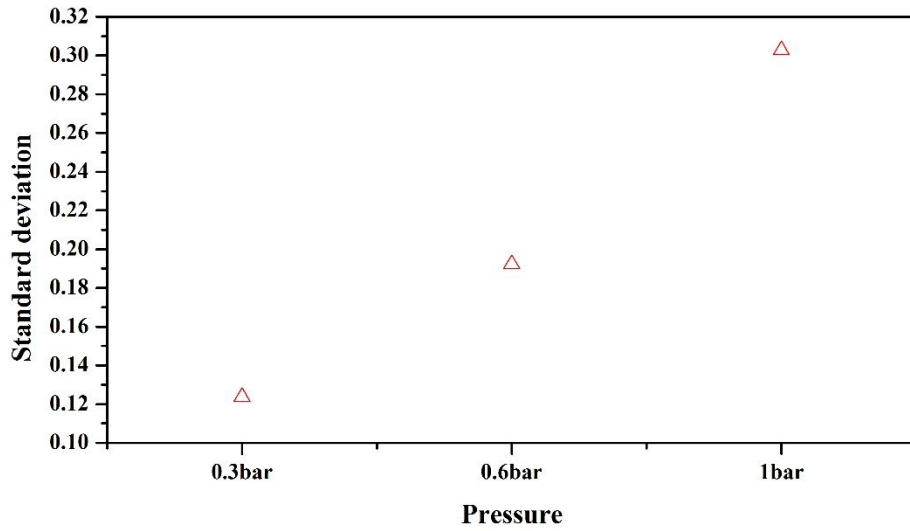


Figure 4.16 Standard deviations of the deposition thickness under different pressure conditions.

4.4.1.4 Susceptor rotation effect

In order to increase the uniformity of the thin film thickness between different wafers, susceptor is rotated at a constant speed. Therefore, the rotation speed is also an essentially important condition. In addition to the previous calculation of 5 rpm, 0 rpm, 10 rpm, 15 rpm calculations are also conducted to compare with. The figure 4.17 shows the comparison of deposition rates between different rotation speeds. It is observed from the results that, when the rotation speed is 0 rpm, the deposition rate is smallest. And the pattern of deposition distribution is consistent with the direction of the gas inlets. When the rotation speed is 15 rpm, the deposition rate is larger than the others. With the increase of the rotation speed, the maximum value of deposition rate is closer to the center and the deposition rate significantly decrease at the edge of the susceptor. Besides, the symmetric axis is changing at different rotation speed. Although along the rotation direction, the uniformity will be improved by increasing the rotation speed. In another word, the uniformity between different wafers will be improved. Moreover, from the figure 4.18, it can be seen that the deposition rate of 15 rpm is nearly 3 times larger than that of 0 rpm. But along the radial direction, the uniformity of 0 rpm is better than the others. Figure 4.19 shows the comparison of the thickness distribution under different rotation speeds with the same average thickness of 4 μm . Along the radial direction, the deposition thickness of 5 rpm, 10 rpm and 15 rpm decreases rapidly at the downstream. But the uniformity of the deposition thickness of 0 rpm is better. Figure 4.20 shows

the comparison of standard deviations of deposition thickness between different rotation speed conditions. In the figure, the standard deviation of 0 rpm is smaller than those of 5 rpm, 10 rpm and 15 rpm. Though uniform deposition between different wafers could not be achieved without rotation, yet theoretically, the lower the rotation speed is, the more uniform the deposition thickness along the radial direction is. The low uniformity of high rotation speed is caused by the flow pattern of the reacting gases. Because the susceptor rotation leads the gases to flow along the rotation direction instead of flowing to the periphery. This phenomenon compound the problem that the deposition rate is high at the upstream. Thus if the uniformity between different wafers can be guaranteed, the rotation speed should be decreased to some extent.

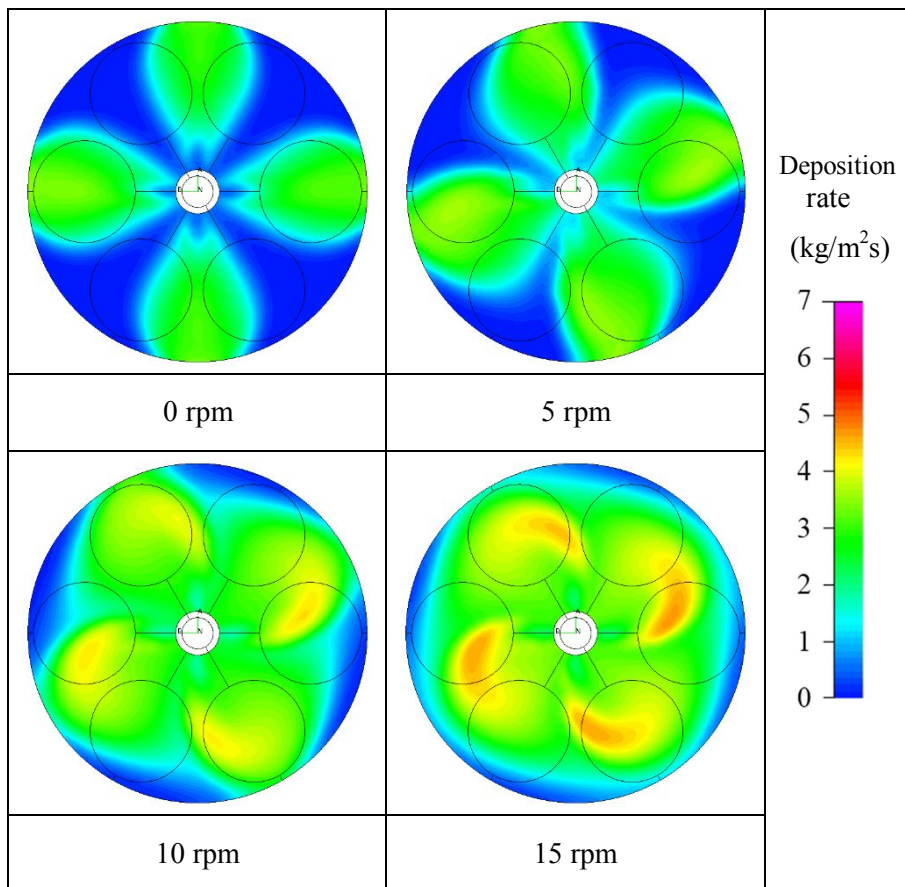


Figure 4.17 GaN deposition rate distribution under different rotation speeds:
2.5 rpm, 5 rpm, 10 rpm, 15 rpm.

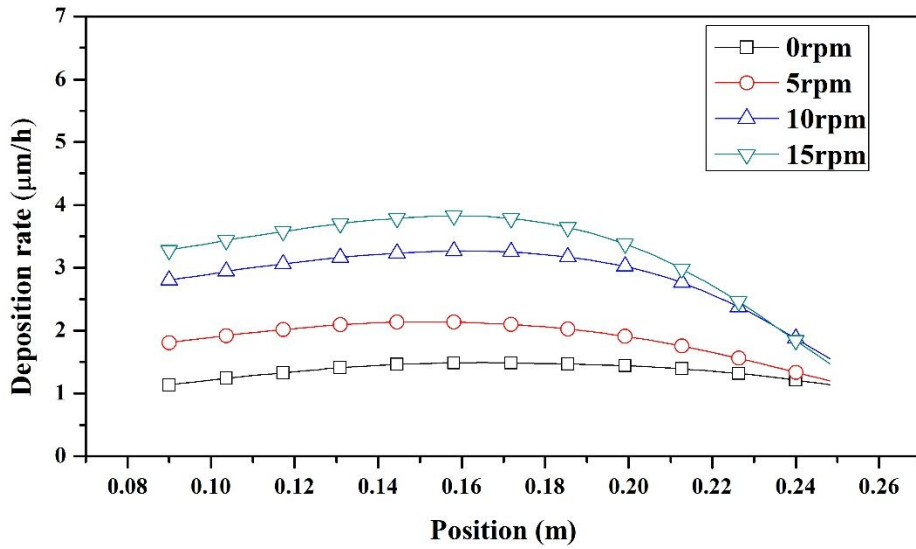


Figure 4.18 Deposition rate distributions along the radial direction from the inlet with different rotation speeds: 0 rpm, 5 rpm, 10 rpm, 15 rpm.

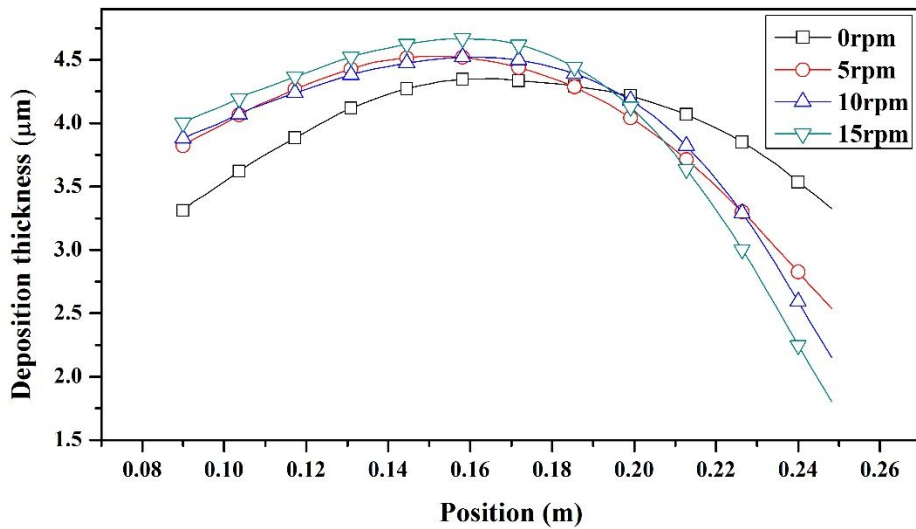


Figure 4.19 Deposition thickness distributions along the radial direction from the inlet with different rotation speeds: 0 rpm, 5 rpm, 10 rpm, 15 rpm.

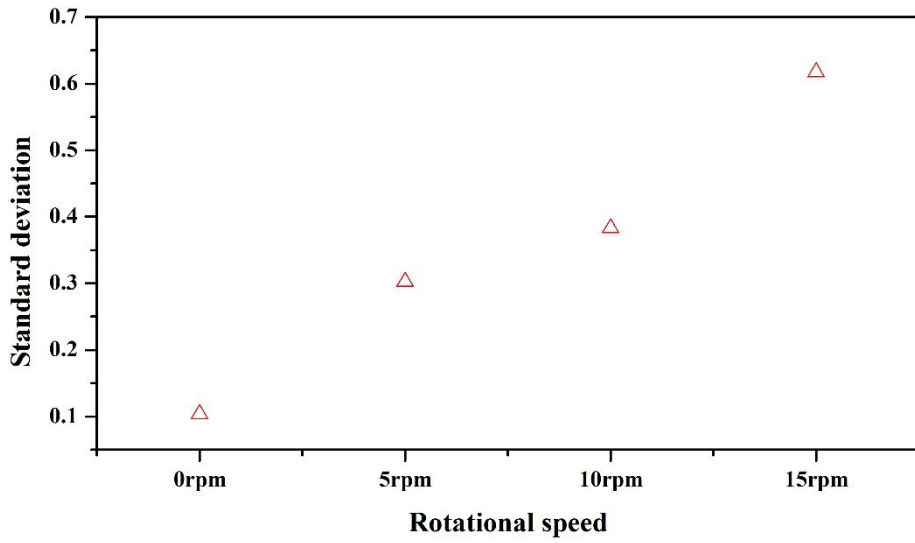


Figure 4.20 Standard deviations of the deposition thickness under different rotation speed conditions.

4.4.1.5 Wafer rotation effect

Besides susceptor rotation, wafer rotation is also employed in the multi-wafer HVPE equipment to increase the uniformity of the GaN deposition thickness (figure 4.21). In the traditional HVPE equipment, only one wafer is rotated [87, 88]. In terms of simulation, the wafer rotation could be modeled by designating rotating volume conditions in the volume of the wafer, which is called “moving solid” in CFD-ACE. However, if the susceptor and wafers rotate at the same time, the direct volume conditions are not feasible to simulate the phenomena because the position of each node at the wafer is constantly changed by the rotation of both susceptor and wafer. Moreover, if the grid deformation is used to simulate the situation, the mesh will be distorted until entirely destroyed.

Taking into account the impossibility of direct simulation on the rotation of susceptor and wafers, we adopt the method to track the position change of the certain points over time, collecting the history of the deposition rates of the certain points. As shown in the figure 4.21, in the case of wafers and susceptors rotating under a certain speed, a certain point at the wafer has moved from the initial position to the final position. This motion can be divided into two parts: in the first movement, only the rotation of susceptor is considered, the point migrates from the initial position to the intermediate position; in the second movement, only the rotation of wafer is considered, the

point migrates from the intermediate position to the final position. If we designate the horizontal axis and vertical axis as x and z, then we can employ geometrical method to precisely calculate the accurate position of the point at a certain time by utilizing the following equation which we derived to describe the movement of the point:

$$X = (a + b) \cos\theta - (a * \cos\theta - a * \cos(\beta + \theta)) \quad (4-6)$$

$$Z = (a + b) \sin\theta + a * \sin(\beta + \theta) - a * \sin\theta \quad (4-7)$$

here, a is the distance from wafer center to probe point

b is the distance from susceptor center to wafer center

θ is the angle of susceptor rotation

β is the angle of wafer rotation

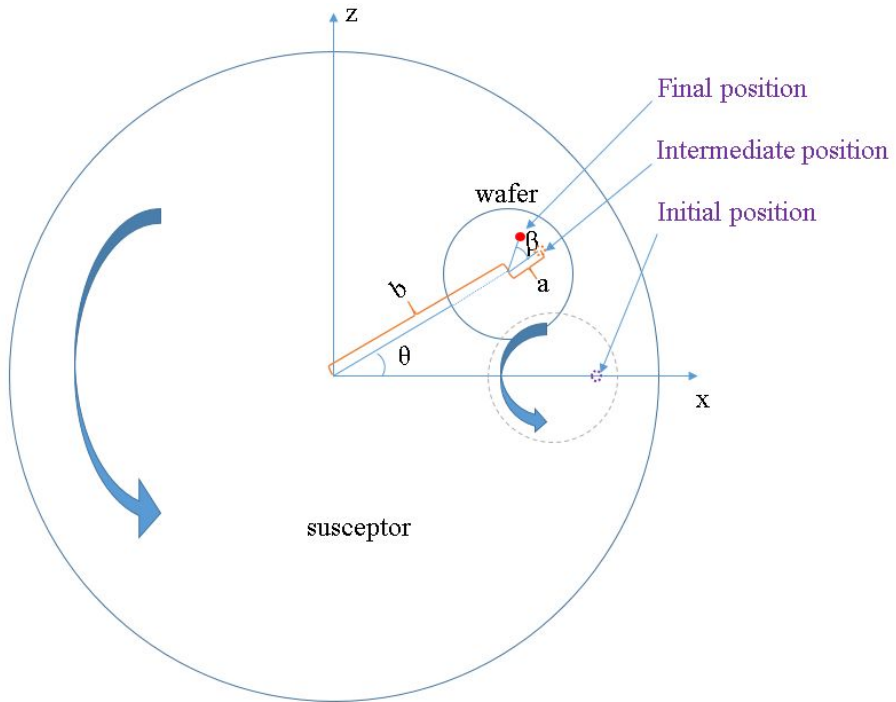


Figure 4.21 Schematic diagram of the movement of a certain point at the wafer.

According to the above theory, through the Matlab program, we selected several points to calculate their positions. For convenience, in this section, the susceptor rotation is called revolution while the wafer rotation is called rotation. When the revolution and rotation is 5 rpm and 10 rpm (5-10), as shown in figure 4.22, the trajectory of the points over time as well as the wafer positions have been drawn. In the figure, under the coupling effect of the revolution and rotation, the initial nearest end point at the wafer will move to the farthest end. Initial farthest point will move to the nearest end. The initial center point at the wafer presents a circular trajectory, which means the position has not changed at the wafer.

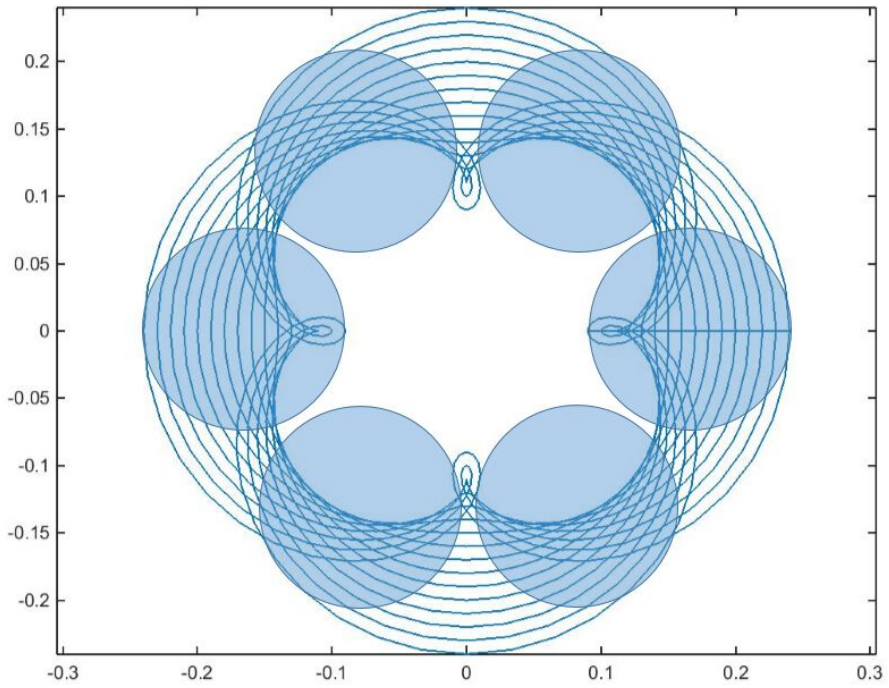


Figure 4.22 Trajectories of the points at the wafers over time under revolution of 5 rpm and rotation of 10 rpm.

Figure 4.23 shows the trajectories of the points under the revolution speed of 5 rpm and the rotation speed from 5 to 40 rpm. It is seen that with the change of the ratio between the revolution speed and rotation speed, trajectories of the points have also changed. Here we do not consider the high rotation speed. Because this method is to track the position change of the point over time, but ignore the effect of wafer rotation on the gas flow. Therefore, if the rotation speed is too high, the accuracy of the results will decline.

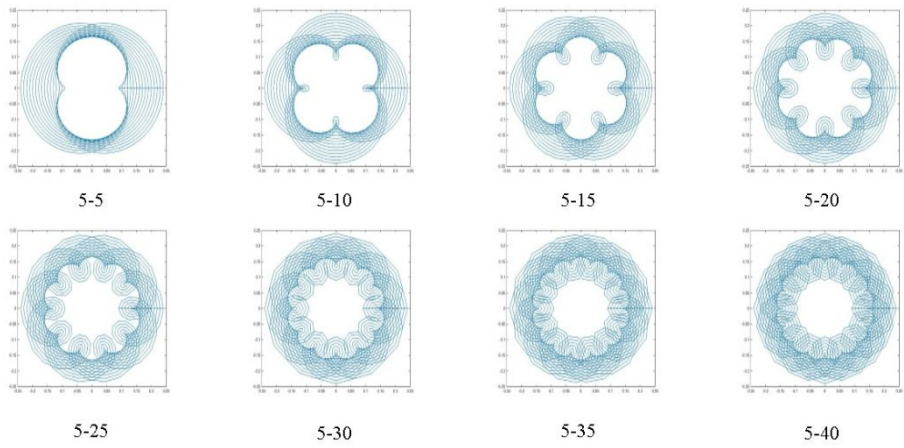


Figure 4.23 Trajectories of the points at the wafers over time under different rotation conditions (revolution-rotation).

Through the method above, we have calculated the deposition rate distributions along the radial direction under the revolution speed of 5 rpm and the rotation speed from 5 to 25 rpm (Figure 4.24). In the figure 4.24, the black square indicates the deposition rate distribution without rotation. It is clearly observed that in the case of no rotation, the uniformity of the deposition rate is lowest. When the rotation is employed, the uniformity of deposition is significantly improved. However, by comparing the 5-10 and 5-20, it is found that fast rotation does not always improve the uniformity of the deposition rate.

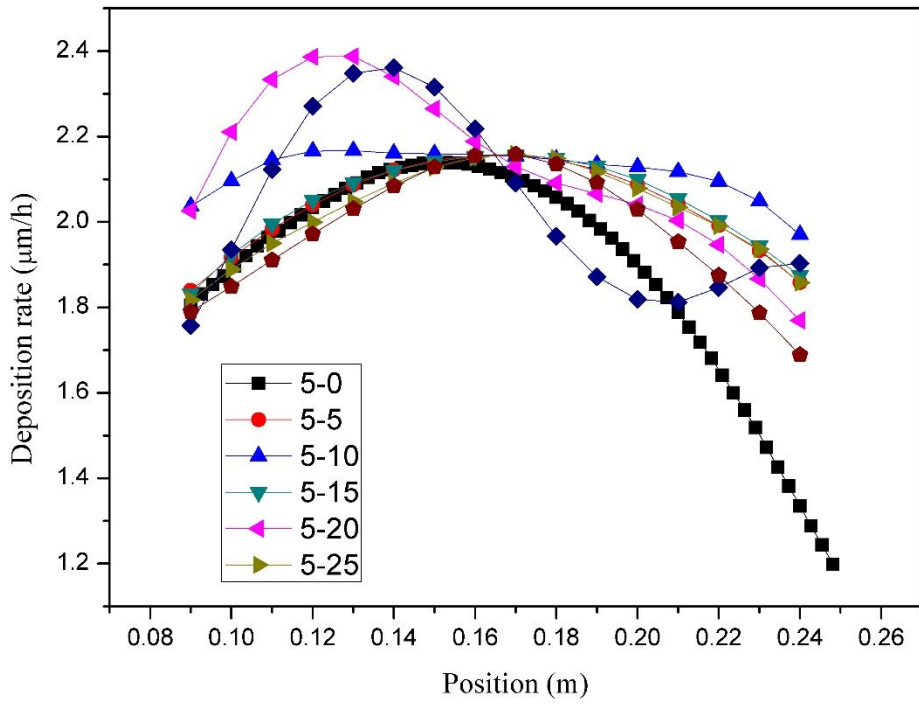


Figure 4.24 Comparison between the deposition rate distributions under different rotation conditions.

Therefore, in order to find the best operating parameter, we have compared all the standard deviations of the deposition rates under the revolution from 1 to 15, at intervals of 1, and the rotation from -40 (the minus sign indicates the directions of revolution and rotation are opposite) to 40 at intervals of 0.5. In the figure 4.25, the standard deviation distribution shows that in the case of the absence of rotation, the standard deviations of the deposition rates are high. Meanwhile, not all the rotations help improve the uniformity of deposition rates. For example, when the directions of revolution and rotation is different, 1-4, 2-8, 3-12, 4-16 significantly increase the deviations. Because the points at the wafers will go through a deposition rate cycle every 90 degree of revolution as shown in the figure 4.8 due to the four-nozzle configuration. Moreover, if the rotation speed is 4 times the revolution, when the revolution is 90 degrees, rotation is exactly 360 degrees. This would result in the closest point, where growth rate is high, moving back to the closest position again, leading to a less uniform deposition. Thus, in the actual production, these combinations of revolution and rotation conditions should be avoided.

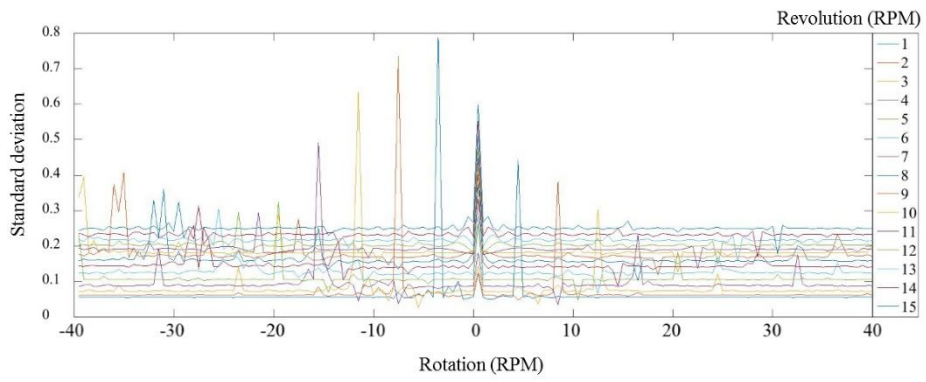


Figure 4.25 Standard deviation distribution under different revolution and rotation conditions.

To find a more intuitive way to investigate the effects of revolution and rotation on the uniformity of the deposition rate, figure 4.26 has been used to clearly show the deviation distribution. From figure 4.26, it is clearly observed that regardless of the directions of rotation and revolution, the conditions of 1-4, 2-8, 3-12, 4-16, 5-20 should be avoided in the actual production. On the contrary, the conditions of 2-4, 3-6, 4-8 could help decrease the deviations of the deposition rates. Besides, through the comparison of the data, it is found that when the directions of revolution and rotation are different, under the condition of 3-6, the standard deviation is 0.027, which is smallest. Therefore, we suggest that if the rotation is employed, 3-6 with rotation and revolution in the opposite direction is the best operating parameter for improving the uniformity.

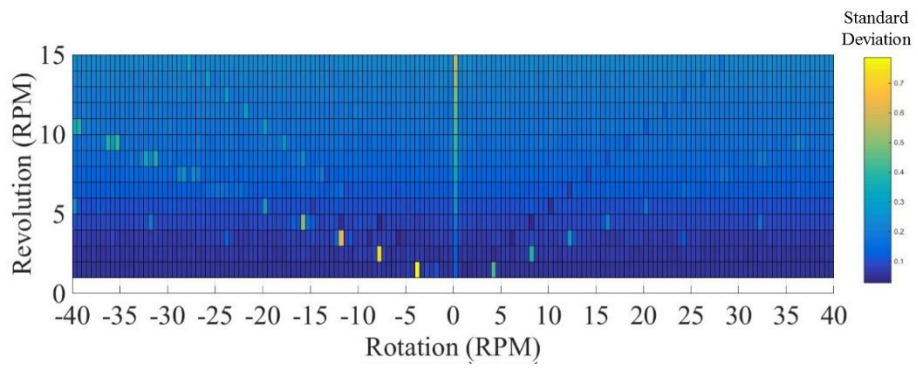


Figure 4.26 Standard deviation map under different revolution and rotation conditions.

4.4.1.6 Carrier gas composition effect

Carrier gas is used to transport the reaction gas so that the diluted reaction gas can flow far away from the nozzle to deposit at the wafers uniformly. The effect of carrier gas flow rate on the deposition rate and deposition thickness has been discussed in the previous section 4.4.1.1. Furthermore, in this section, the carrier gas composition effect on the uniformity will be discussed in detail. Since the carrier gas must be steadily feasible and will not contaminate the crystal thin film, nitrogen and hydrogen as well as the mixture of nitrogen and hydrogen has been widely used in the industrial production of manufacturing GaN thin films [113]. With the total flow rate of carrier gas fixed, four simulation tests have been performed under different proportions of nitrogen and hydrogen: 1) nitrogen 0 slm and hydrogen 30 slm; 2) nitrogen 10 slm and hydrogen 20 slm; 3) nitrogen 20 slm and hydrogen 10 slm; 4) nitrogen 30 slm and hydrogen 0 slm. The calculation results of deposition rate distribution are shown in the figure 4.27. It is noted that with the increase of the proportion of nitrogen, the overall deposition rate becomes smaller. In addition, the maximum deposition rate also migrates from the center to periphery when the flow rate of nitrogen is increased. When the flow rate of nitrogen is 0, there is almost no deposition at the peripheral part of the susceptor. As the flow rate of nitrogen increases, the deposition began to appear at the peripheral part. In the figure 4.28, the deposition rate distribution along the radial direction indicates that the deposition rate is

largest with the absence of nitrogen. Especially, the deposition rate without nitrogen is greatly larger than the other cases at the upstream section. And the deposition rate without hydrogen is smallest. When the flow rate of nitrogen is 0, the deposition rate decreases rapidly along the radial direction. Meanwhile, when the flow rate of hydrogen is 0, the curve is relatively flat. This is because as carrier gases, the most notable difference between hydrogen and nitrogen is the density. The density of reacting gas of GaCl is larger than both of nitrogen and hydrogen. So the transport of GaCl to the wafer in the carrier gas depends on the density difference between GaCl and carrier gas. The density of the hydrogen is much smaller than nitrogen, so that under the hydrogen atmosphere, the GaCl injected from the nozzle can descend rapidly on the surface of the wafer to deposit. In a contrary, under the nitrogen atmosphere, GaCl descends to the wafer relatively slowly and could flow to a further place to descend. As a result, the curve with only nitrogen looks more flat along the radial direction.

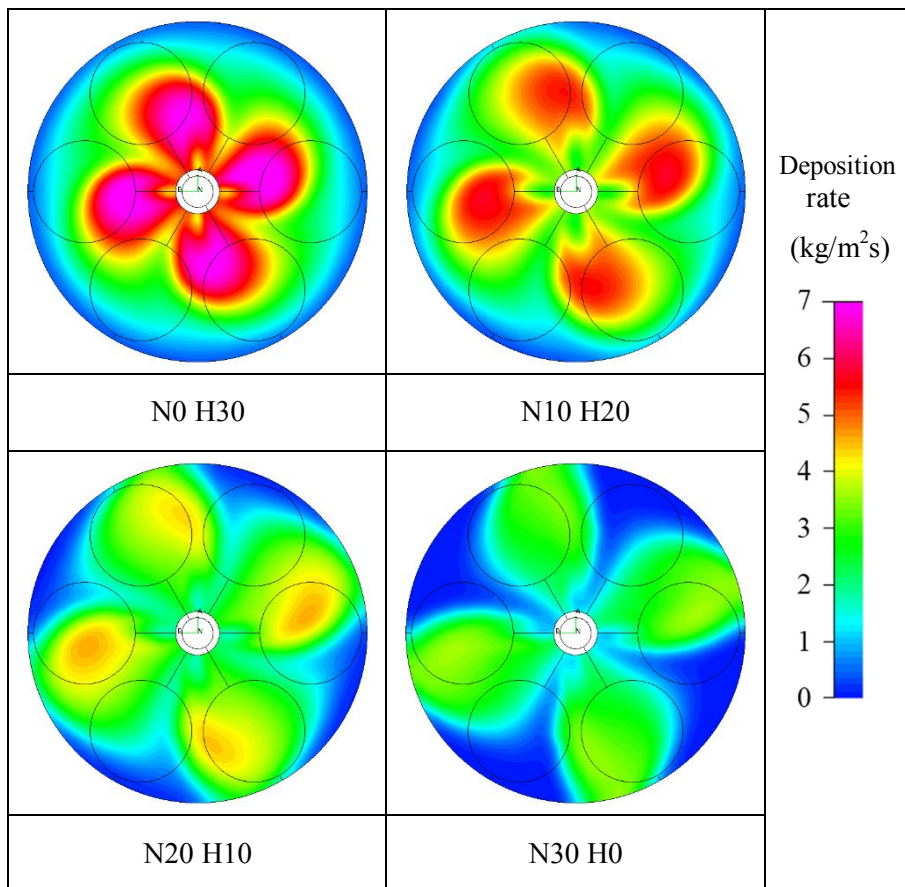


Figure 4.27 GaN deposition rate distribution under different carrier gas compositions: N0 H30, N10 H20, N20 H10, N30 H0.

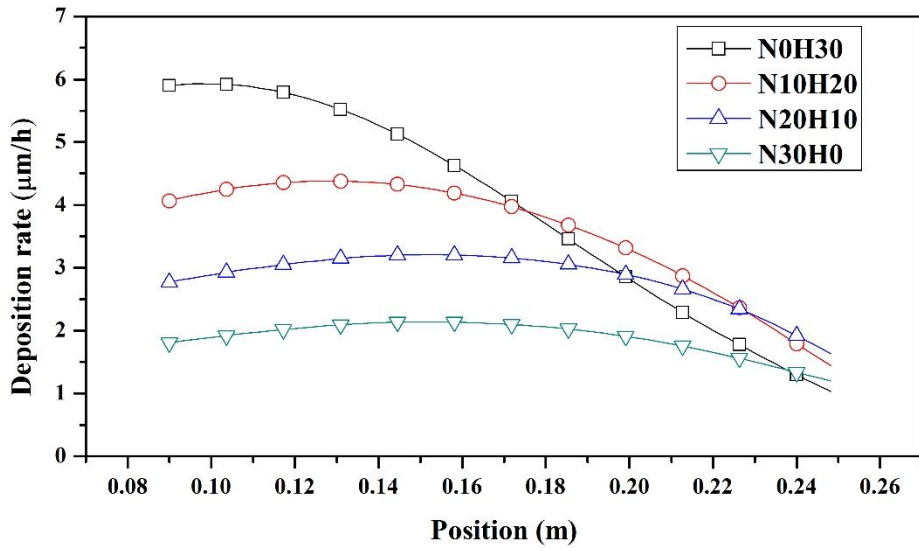


Figure 4.28 Deposition rate distributions along the radial direction from the inlet with different carrier gas compositions: N0 H30, N10 H20, N20 H10, N30 H0.

Figure 4.29 is the comparison of the deposition thickness distribution under different carrier gas composition conditions. From the figure, it is apparently shown that if there is no hydrogen in the carrier gas, the curve is quite flat. Moreover, when the flow rate of hydrogen is 10slm, the uniformity is also excellent. According to the standard deviation from figure 4.30, the uniformity of the thickness is best when only nitrogen is used.

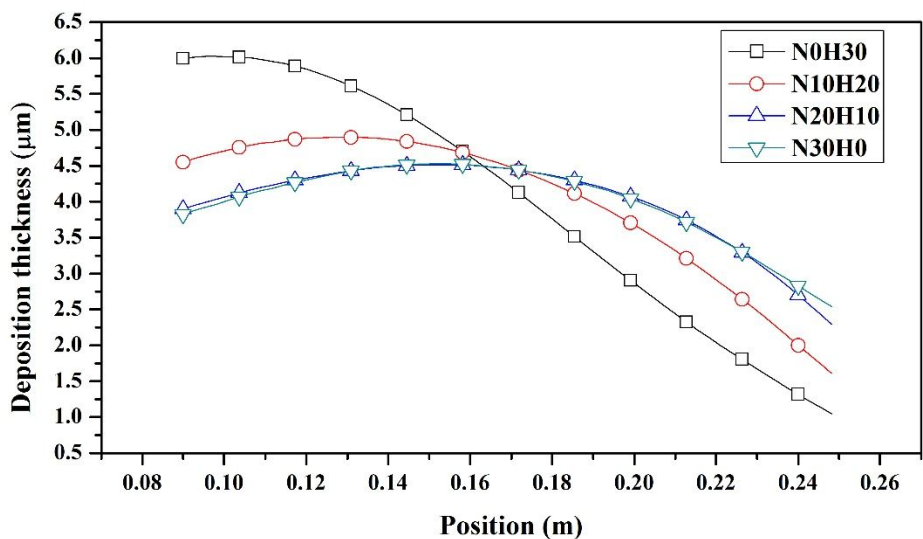


Figure 4.29 Deposition thickness distributions along the radial direction from the inlet with different carrier gas compositions: N0 H30, N10 H20, N20 H10, N30 H0.

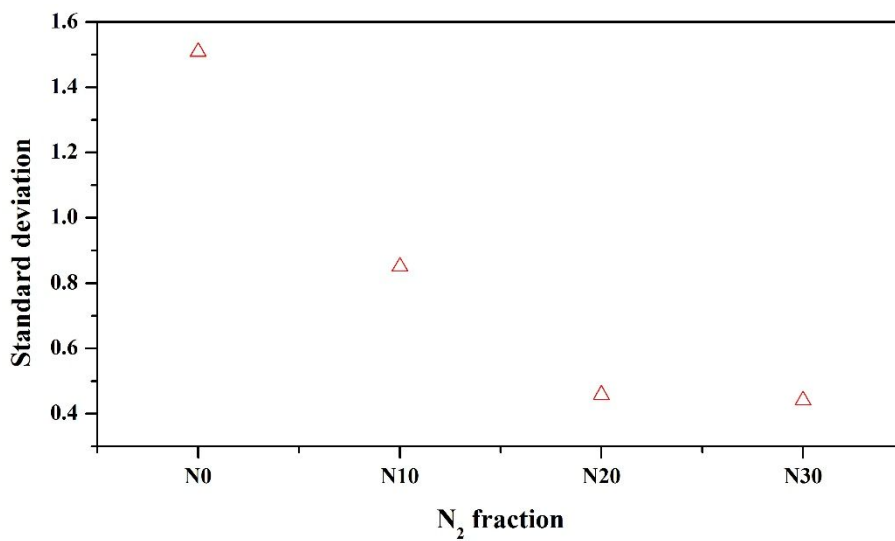


Figure 4.30 Standard deviations of the deposition thickness under different carrier gas composition conditions

4.4.2 Effect of non-uniform deposition rate on hillocks

4.4.2.1 Hillock distribution at the GaN surface

Hillocks have been observed from the experiments at both 1193 K and 1223 K. Figure 4.31 shows the surface morphology taken from the center of the sapphire wafers of P2, P4 and P6 (three 2-inch wafers are called P2, P4 and P6 from center to periphery as shown in figure 3.2.) by 3D laser measuring microscope. The hillocks at 1223 K are larger than the hillocks at 1193 K, which might be caused by the high growth rate at high temperature. Moreover, from the comparison between the three wafers, it is clear seen that the density of the hillocks increases from P2 to P6.

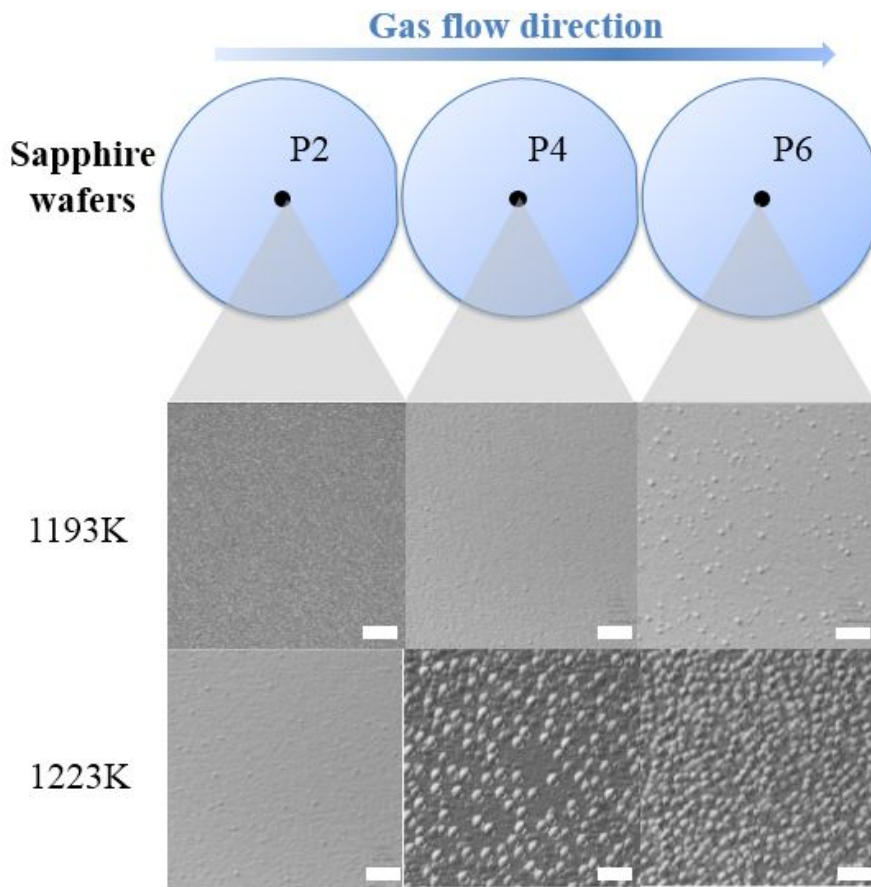
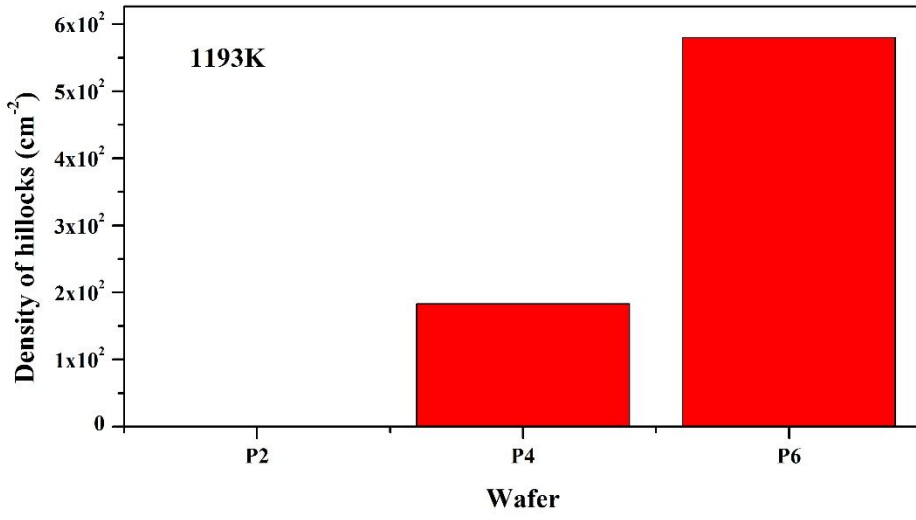
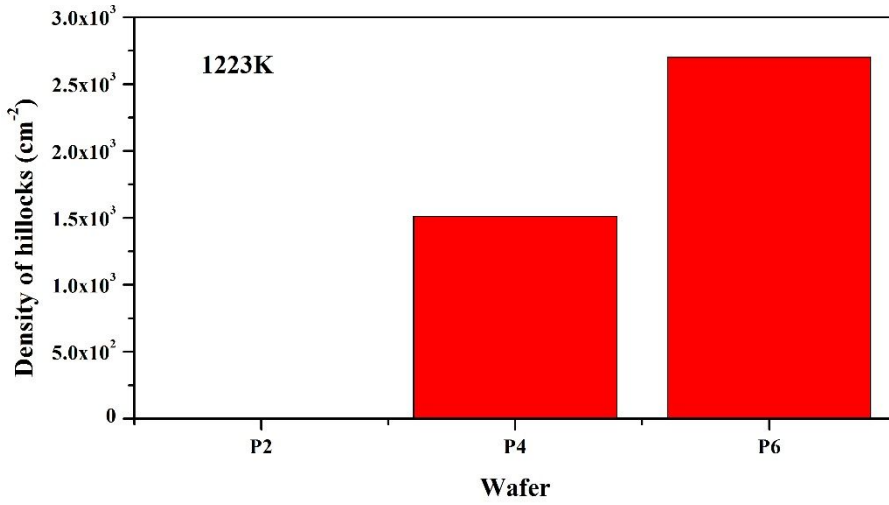


Figure 4.31 Surface morphology taken from the center of the sapphire wafers of P2, P4 and P6 by 3D laser measuring microscope (white scale bar is 320 μm).

To exactly illustrate the increase of the hillocks, the quantity of the hillocks is calculated by the image processing of the Matlab code in the Fig. 4.32. Because the dimensions of the hillocks at 1193 K and 1223 K are different, the identified critical sizes of two temperatures are defined differently to make the density of the hillocks of P2 wafers as zero for both 1193 K and 1223 K. As shown in the figure 4.32, at 1193 K, from P2 to P6, the density of the hillocks are 0 cm^{-2} , $1.83 \times 10^2 \text{ cm}^{-2}$, $1.51 \times 10^3 \text{ cm}^{-2}$; at 1223 K, from P2 to P6, the density of the hillocks investigated are 0 cm^{-2} , $5.79 \times 10^2 \text{ cm}^{-2}$, $2.70 \times 10^3 \text{ cm}^{-2}$.



a



b

Figure 4.32 The density of the hillocks at the GaN surface grown under: (a) 1193 K and (b) 1223 K.

4.4.2.2 Growth rate distribution along the radial direction

Through the numerical calculations, the growth rate distributions at the susceptor and wafer under 1193 K and 1223 K have been obtained, which are shown in the figure 4.33. The patterns of the deposition rate distribution are both 4-fold due to the four-way flow design of the gas inlets. The deposition rate of 1223 K is larger than that of 1193 K because the sticking coefficient is higher at a higher temperature. After averaging the deposition rates along the rotation direction and plotting them along the radial direction, the comparison of deposition rate distribution along the radial direction between 1193 K and 1223 K is achieved in figure 4.34. The trends of the deposition rate under 1193 K and 1223 K are similar that both of the curves increase at the upstream and decrease at the downstream, which is identical to our previous research results [95].

Therefore, through the comparison between the deposition rate distribution by calculations and surface morphology by experiments, we could conclude that the density of hillocks is not increased by the increasing of deposition rate.

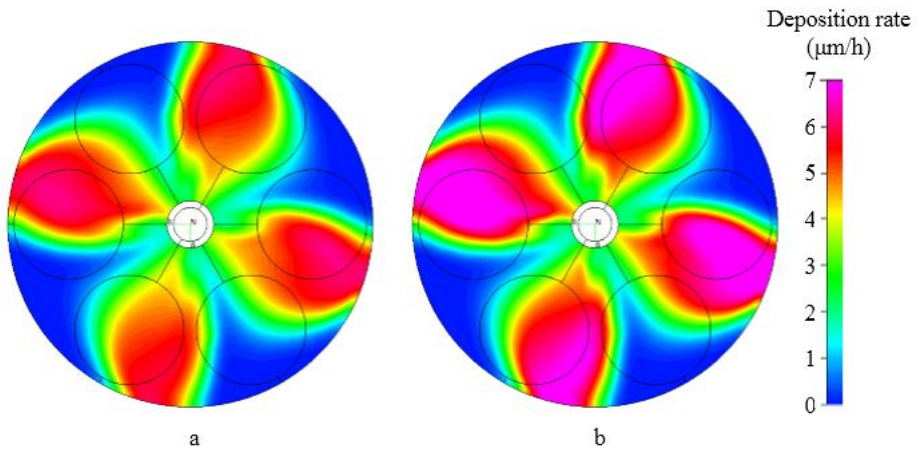


Figure 4.33 Deposition rate distribution at different temperatures: (a) 1193 K; (b) 1223 K.

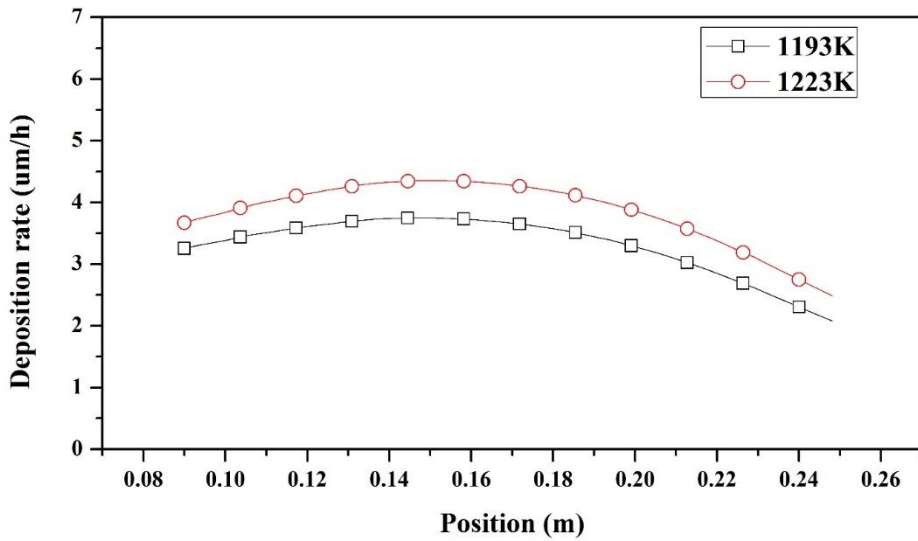
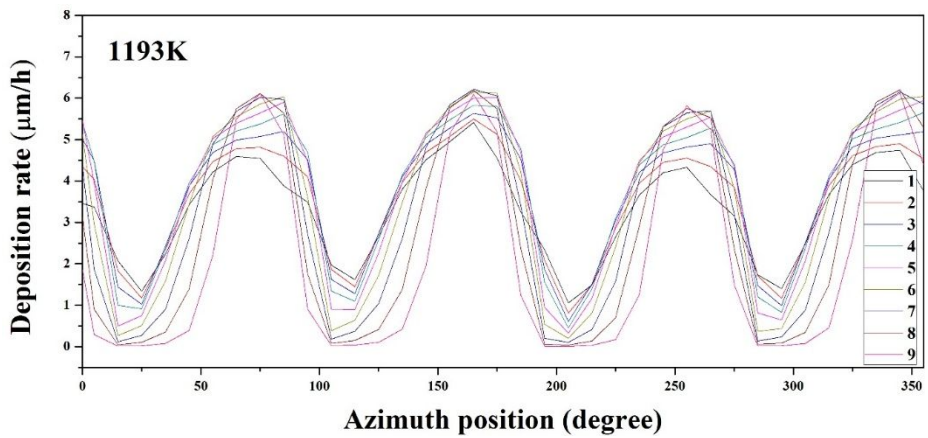


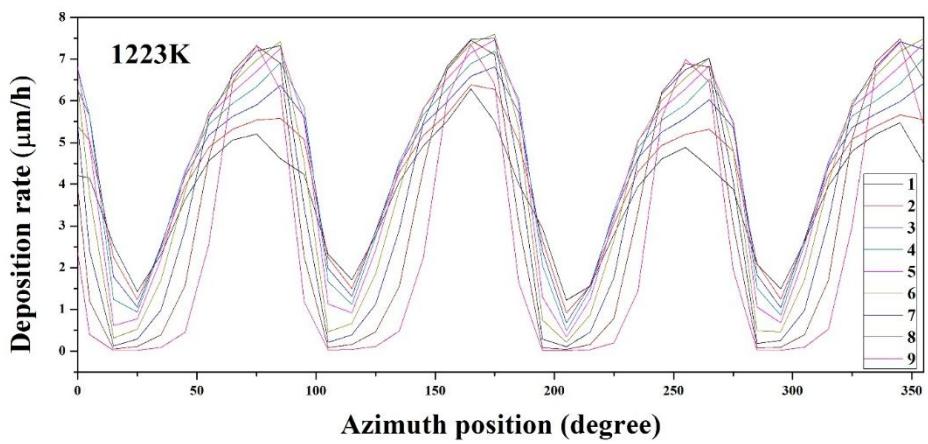
Figure 4.34 Deposition rate distribution along the radial direction at 1193 K and 1223 K.

4.4.2.3 Growth rate distribution along the rotation direction

Since the susceptor keeps rotating during the operation, a certain position at the sapphire wafers will experience high growth rate and low growth rate alternately four times each rotation. Therefore, the degree of the deposition rate change has been investigated by comparing the deposition rate distributions along the rotation direction at different radii. As shown in the 4.35, nine curve probes have been selected from the nearest point of P2 to the farthest point of P6 from the inlets. Curves 1, 2 and 3 are the nearest point, center point and farthest point of P2. In the same way, there are totally nine curve probes are employed to plot the deposition rate. Figure 4.34 shows the deposition rate distribution along the radial direction at 1193 K and 1223 K. The black curves in both figure 4.35(a) and 4.35(b), which indicate nearest point of P2, obviously have the smallest fluctuation. From curve 2 to curve 9, the fluctuation becomes gradually large.



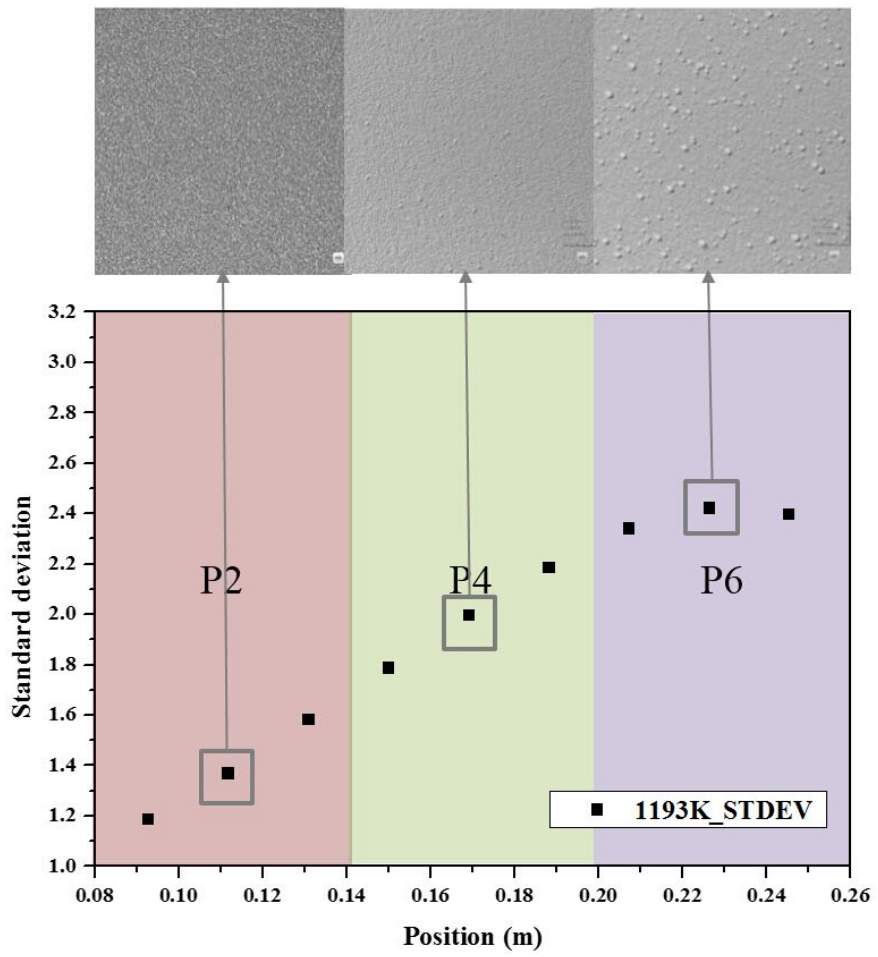
a



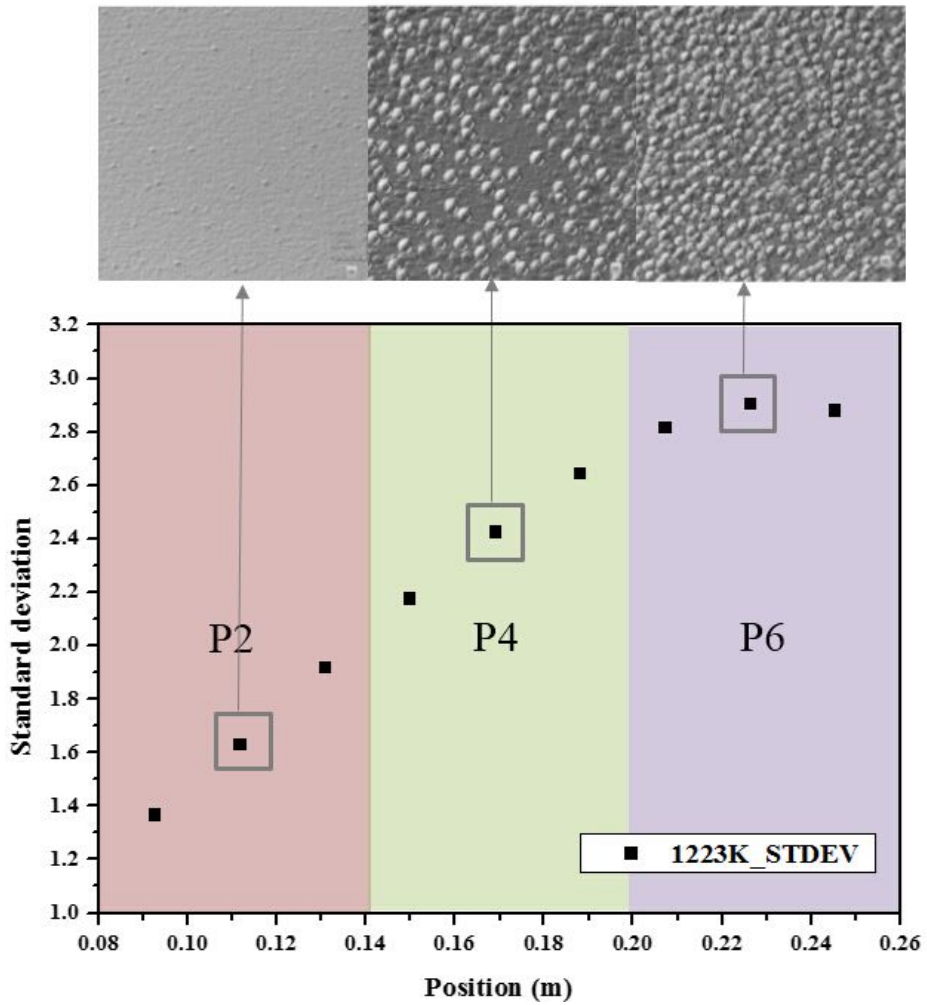
b

Figure 4.35 Deposition rate distribution along the radial direction at different temperatures: (a) 1193 K; (b) 1223 K.

To evaluate and compare the degrees of fluctuation of the deposition rate between the curve probes with different radii, the standard deviation of deposition rate along the rotation direction has been introduced. Fig. 4.36 shows the comparison between the hillocks and standard deviation of deposition rate along the rotation direction at 1193 K and 1223 K. The density of hillocks at 1223 K are larger than those of 1193 K seems to support the idea that high deposition rates increase hillock density. However, through the comparison between the figure 4.36(a) and 4.36(b), it is seen that the standard deviations at 1223 K are larger than those at 1193 K, which is also another reason why the density of hillocks at 1223 K is larger than that of 1193 K. Besides, the deviation distribution shows a same trend at 1193 K and 1223 K that along the flow direction, the deviation increases gradually and decreases slightly at the end of the P6. Accordingly, the density of the hillocks increases from the center of P2 to the center of P6. So the present study strongly support the idea that non-uniform deposition rate could induce hillocks.



a



b

Figure 4.36 The comparison between the hillock distribution and the deviation of the deposition rate along the radial direction for P2, P4 and P6 at: (a) 1193 K; (b) 1223 K.

4.4.2.4 Rotation effect on non-uniform deposition rate

For the equipment we discussed in this study, the primary factor resulting in the non-uniform deposition is the rotation of the susceptor. Because accompanied by the rotation of the susceptor, 4 gas inlets injecting the reacting gases separately, leading to a non-uniform impingement of the atoms of reacting gases on the GaN surface site. This non-uniform impingement could easily cause the irregular arrangement of atoms on the surface site, which might provide a great deal of screw dislocations, leading to a high density of hillocks. To improve the uniformity of the atoms impinging on the surface site, a more uniform distribution of reacting gases should be formed above the wafers. The more uniform distribution of reacting could be obtained by adjusting the flow pattern of the reacting gases. Therefore, the rotation speed has been increased to improve the uniformity of the deposition along the rotation direction. Figure 4.37(a) and figure 4.37(b) show the comparison of flow velocity vector distributions at the horizontal symmetry plane with 1223 K under 5 rpm and 15 rpm respectively. In the figure 4.37(b), due to a higher rotation speed of 15 rpm, the magnitudes of the velocity vectors above the wafers are obviously more uniform than those of 5 rpm in the figure 4.37(a). Thus, the calculation results show that the high rotation speed will improve the uniformity of the reacting gas flow.

The calculation results of different rotation speeds have supported the prediction that high rotation speed will improve the uniformity of deposition rate. Figure 4.37(c) and figure 4.37(d) show the comparison of deposition rate distribution with different rotation speeds of 5 rpm and 15 rpm at 1223 K. Compared with the deposition rate distribution at 5 rpm in the figure 4.37(c), the deposition rate is larger at 15 rpm in the figure 4.37(d). Because high rotation speed of susceptor effectively extend the residence time of the reacting gas above the susceptor, giving rise to a higher deposition rate. Moreover, the blue color (low deposition rate) at the directions between the gas inlets directions has diminished, which mean that high speed rotation not only increases the deposition rate but also improve the uniformity of the deposition rate along the rotation direction. Figure 4.38 shows the comparison of deposition rate distributions along the rotation direction between 5 rpm and 15 rpm. It is also observed that the deposition rate of 15 rpm is larger than that of 5 rpm. The peaks of deposition rate distribution at 15 rpm in the figure 4.38b are less steep than those of 5 rpm, which means that the fluctuation of deposition rate is smaller at 15 rpm. Besides, figure 4.39 shows the comparison of standard deviation of deposition rate along the rotation direction between 5 rpm and 15 rpm. The highest deviation value (1.476) in the 15 rpm is even lower than the deviation at the center point (1.629) of P2 in the 5 rpm. This result could demonstrate that under 15 rpm, besides the wafer of P2 and P4, the surface morphology of even P6 will be as clear as that of P2

in 5 rpm (Fig. 4.31). Therefore, through the calculations, it is indicated that high speed rotation will provide a more uniform gas flow pattern. The more uniform gas flow pattern results in a higher uniformity of deposition rate along the rotation direction, which is a principal factor inducing the hillock formation in the experiments.

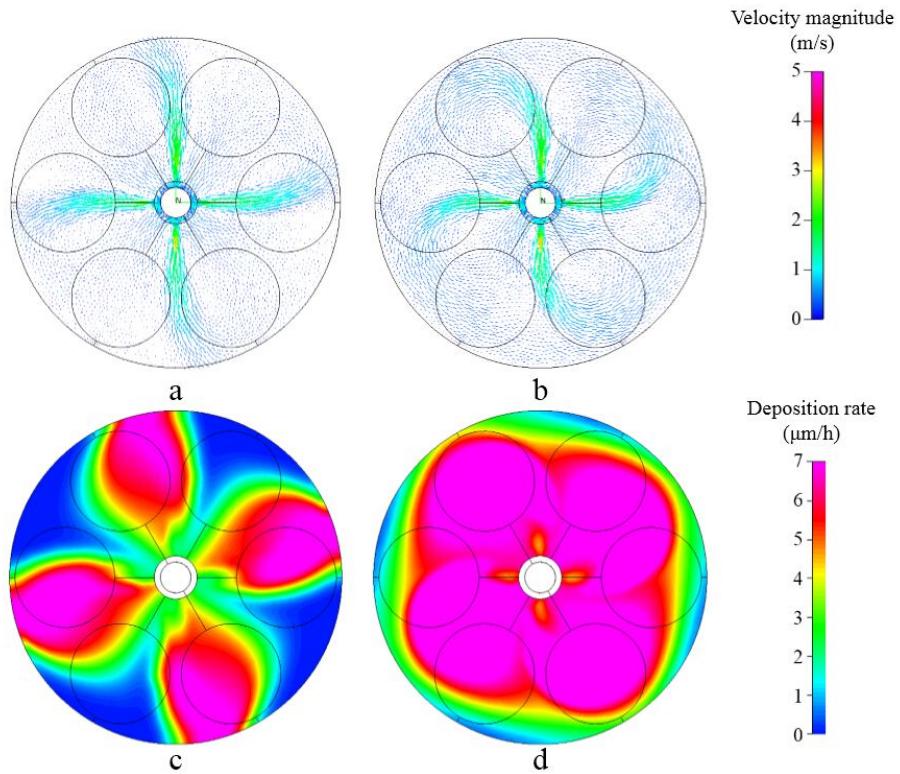
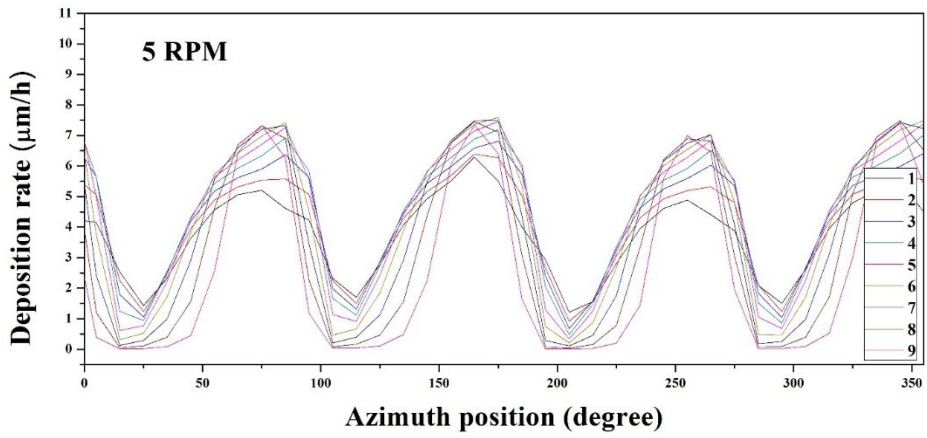
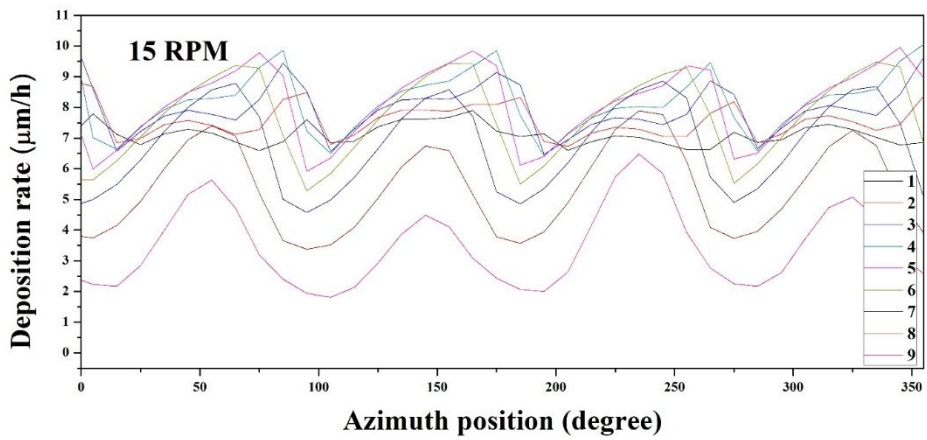


Figure 4.37 Flow velocity vector distributions and deposition rate distributions at 1223 K under different rotation speeds: (a) flow velocity vector distribution at the horizontal symmetry plane under 5 rpm; (b) flow velocity vector distribution at the horizontal symmetry plane under 15 rpm; (c) deposition rate distribution under 5 rpm; (d) deposition rate distribution under 5 rpm.



a



b

Figure 4.38 Deposition rate distribution along the rotation direction at different rotation speeds: (a) 5 rpm; (b) 15 rpm.

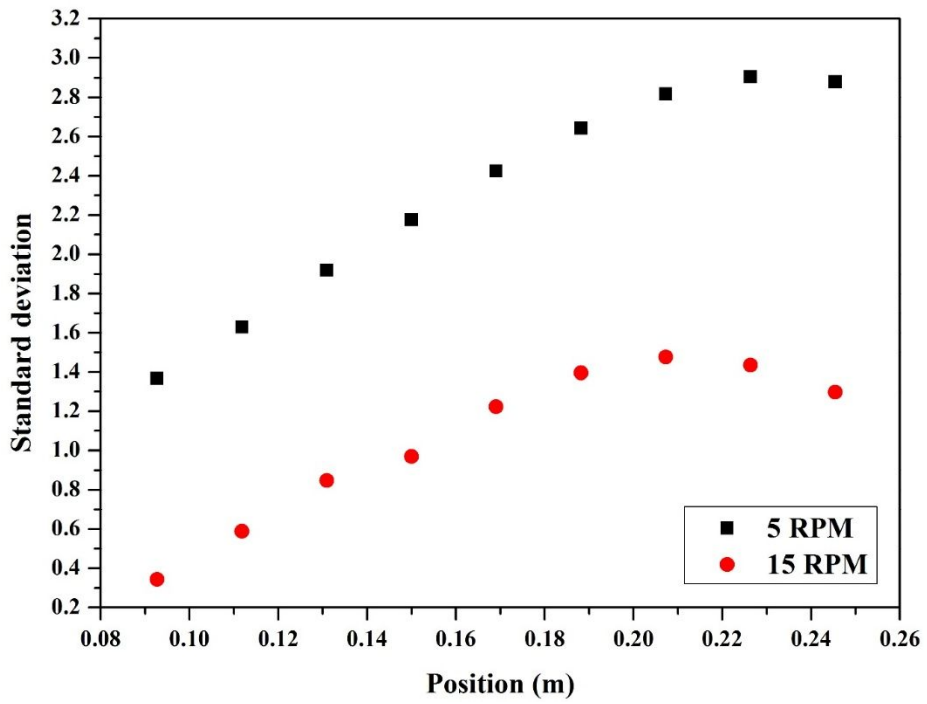


Figure 4.39 The comparison of standard deviation of deposition rate along the rotation direction between 5 rpm and 15 rpm.

4.5 Summary

4.5.1 Thickness uniformity

In this work, experiments and numerical calculations have been compared to study the newly developed 6-inch wafer HVPE device. In the experiments, the flow rates of carrier gas are changed to improve the uniformity. In order to study the effect of carrier gas on the deposition rate of the epitaxial layer, we implemented the steady CFD simulation under the same condition and obtained the similar results. In addition, we suggested to use the average values with different directions to achieve the deposition rate distributions along the radial direction and use the standard deviation to evaluate the uniformity. Through comparing the experiments and the calculations, it can be concluded that increasing the carrier gas to some extent would improve the uniformity. Moreover, with the calculation results of each species, the gas flow features have been analyzed. Moreover, the temperature effect on the deposition rate is also elaborated. By comparing the three results of different temperatures, it is found that high temperature is beneficial to the high uniform distribution of the deposition rate along the radial direction. Since the calculation results under different carrier gas flow rates agree well with the experimental results, though there is no experimental data for the pressure to compare with the calculation data, yet the calculation results with different pressures are extremely credible. Through the analysis of calculation results, it is certain that low pressure is helpful to achieve the high uniformity

of thickness deposition along the radial direction. Although the low pressure will result in more complicated process, inconvenient operating procedure and more operation time, yet proper low pressure can be used to improve the uniformity of the deposition thickness. Besides, calculations under four rotation speeds of susceptor also have been conducted. It is seen from the results that the radial uniformity of deposition thickness is best at low speed. However, low speed will decrease the uniformity of deposition thickness along the rotation direction. So the rotation speed could be decreased to improve the uniformity of the thickness of the thin film until deposition thickness along the rotation direction becomes not uniform. Furthermore, the wafer rotation speed is also studied. Through the comparison between the deviations of different wafer rotation speeds, it is investigated that with opposite rotation direction, susceptor and wafer rotate at 3 and 6 rpm has the best uniformity. The last parameter elaborated is the carrier gas composition. When the carrier gas is composed entirely of nitrogen, the uniformity is finest. Therefore, in this equipment, carrier gas composed entirely of nitrogen is the best choice. Figure 4.40 shows the optimal operating parameters for high thickness uniformity along the radial direction in the newly developed 6-inch wafer HVPE device. And table 4.3 has shown the specific value of the stand deviation under different operating parameters. In a word, with regard to the uniformity of deposition thickness along the radial direction, high carrier gas

flow rate, high temperature, low pressure, low rotation speed and nitrogen as the carrier gas are the optimized conditions.

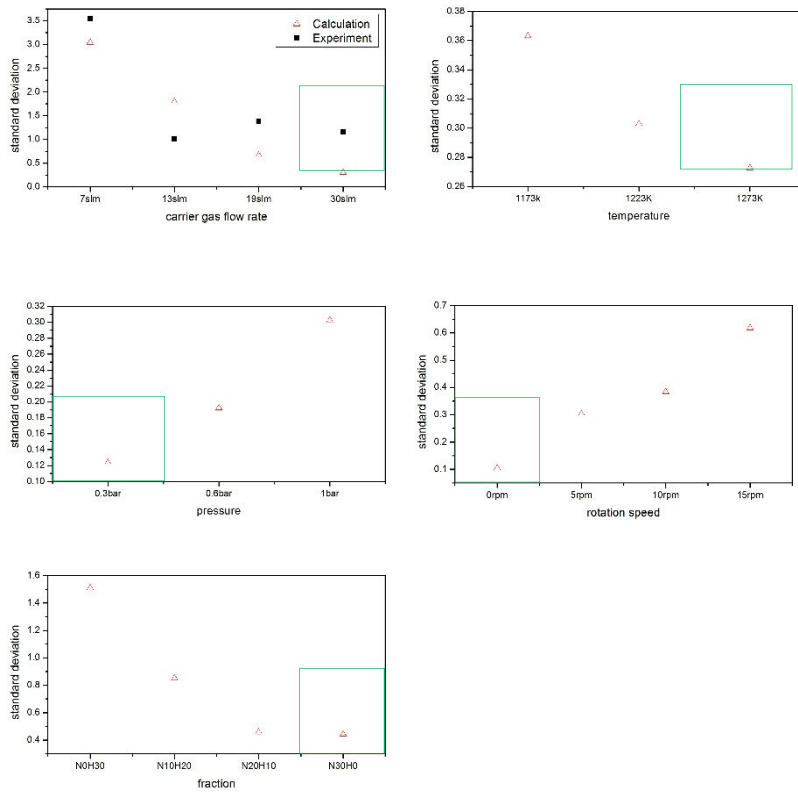


Figure 4.40 Optimal operating parameters for high thickness uniformity along the radial direction in the newly developed 6-inch wafer HVPE device.

Carrier gas flow rate	Standard deviation	
	Calculation	Experiment
7 slm	3.043	3.536
13 slm	1.790	1.003
19 slm	0.663	1.376
30 slm	0.303	1.162
Temperature		
1173 K	0.363	
1223 K	0.302	
1273 K	0.273	
Pressure		
0.3 Bar	0.124	
0.6 Bar	0.192	
1 Bar	0.303	
Susceptor rotation speed		
0 rpm	0.104	
5 rpm	0.303	
10 rpm	0.383	
15 rpm	0.617	
Wafer rotation speed		
-6 rpm (Susceptor 3 rpm)	0.027	
Carrier gas composition		
N0H30	1.508	
N10H20	0.851	
N20H10	0.458	
N30H0	0.442	

Table 4.3 Standard deviation under different operating parameters in the newly developed 6-inch wafer HVPE device.

4.5.2 Processing time

In addition to the uniformity, the processing time is also an essential factor in the GaN film growth. The short process time could improve the competitiveness of the production by saving the power cost and increasing the throughput. Figure 4.41 shows the processing time comparison between different carrier gas flow rates, temperatures, pressures, rotation speeds and carrier gas compositions in the HVPE equipment, respectively when the average deposition thickness of GaN thin film along the radial direction is 4 μm . In the figure, the conditions with the shortest processing time have been indicated by the green squares. Compared with the standard deviations from the figure 4.40, it can be concluded that the exclusive condition that high temperature could not only improves the uniformity of the deposition thickness but also saves processing time. In contrast, the other conditions beneficial to the high uniformity such as high carrier gas flow rate, low pressure, low rotation speed and carrier gas without hydrogen go against short processing time.

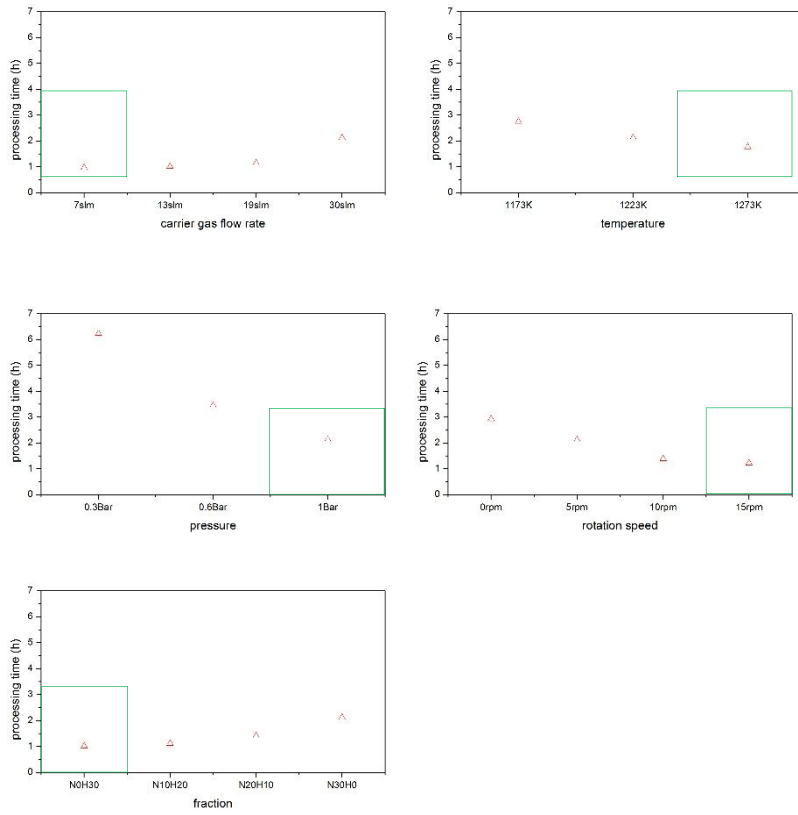


Figure 4.41 Optimal operating parameters for shortest processing time in the newly developed 6-inch wafer HVPE device.

The processing times under different operating parameters are listed in the table 4.4. From this table, for the carrier gas flow rate, temperature, rotation speed, carrier gas composition, the processing time of the longest one is approximately twice as long as the shortest one, respectively. For the pressure, the longest one is roughly three times as long as the shortest one. Therefore, though the uniformity of the deposition thickness is important, yet the processing time is also should be considered.

Carrier gas flow rate	Processing time (h)
7 slm	0.96
13 slm	1.01
19 slm	1.13
30 slm	2.12
Temperature	
1173 K	2.75
1223 K	2.12
1273 K	1.77
Pressure	
0.3 Bar	6.23
0.6 Bar	3.44
1 Bar	2.12
Rotation speed	
0 rpm	2.92
5 rpm	2.12
10 rpm	1.38
15 rpm	1.22
Wafer rotation speed	
28 rpm (Susceptor 15 rpm)	1.10
Carrier gas composition	
N0H30	1.02
N10H20	1.19
N20H10	1.41
N30H0	2.12

Table 4.4 Processing time under different operating parameters in the newly developed 6-inch wafer HVPE device.

4.5.3 Hillock density distribution

In this chapter, we have discussed the influence of non-uniform deposition rate on the hillock formation in the multi-wafer horizontal HVPE equipment. Through the comparison of the hillocks distribution, deposition rate along the radial direction and deviation of deposition rate change, it is found that the density of hillocks is related to the large deposition rate change, rather than the high deposition rate. From the calculation results of the deposition rate distribution, the deposition rate change becomes large along the radial direction from center to periphery. This phenomenon is caused by the non-uniform reacting gas depositing at the surface site, which is the result of the unique geometry of 4 inlets separated transporting the reacting gases. Therefore, to solve this problem, we have suggested that the rotation speed of susceptor should be increased. The calculation result of high rotation speed shows a more uniform deposition rate and lower deviation of deposition rate change, which would prevent the formation of the hillocks at the GaN surface.

Chapter 5. Three-way nozzle design

5.1 Introduction

The price of the LED chip is among the chief factors which could affect the competitiveness of the LED lightings. To reduce the cost of producing LED chip, throughput is increased by loading more and larger wafers into the HVPE equipment. Different from the traditional equipment with one susceptor and one wafer, the novel equipment has 7 susceptors stacked vertically with 4 inch sapphire wafer on each one. In this chapter, the experiments of new nozzle with 3 directions of reaction gas holes, which is called 3-way nozzle has been conducted. Three-way nozzle could be used to produce n-GaN with Si dopants. Because this nozzle includes a third gas pipe transporting the SiH_4 gas. However, in the experiments, SiH_4 gas is replaced by N_2 . In order to investigate the discrepancy between different susceptors, a complex multi-layer model has been developed by take advantage of hybrid grids (combination of structured grids and unstructured grids).

5.2 Model description

Though single layer model of HVPE is steadily available and able to predict the deposition distribution, yet it is limited to investigate the fluid flow and deposition distribution between different susceptors. So a more detailed model with 7 susceptors has been developed. Figure 5.1 shows the geometry of the model composed of stacked susceptors and complex nozzle from different views. The model contains 2981216 structured and unstructured grids. Considering there is no heat transfer in the nozzle, the thickness of the gas tube in the nozzle is ignored by applying the “thin wall” option due to the complicity of the nozzle design. GaCl gas is transported from top inlets by 3 pipes and sprayed into the susceptors through the round gas holes located in every layer. In the same way, N₂ is transported form another 3 pipes and spayed into the susceptors through the round gas holes in every layer. In the experiments of growing undoped GaN, nitrogen is substituted for doping gas of SiH₄. The 6 tubes occupy most space of the outer tube and the remaining space is used to transport the NH₃, which is sprayed out from the elliptic holes under the GaCl gas holes.

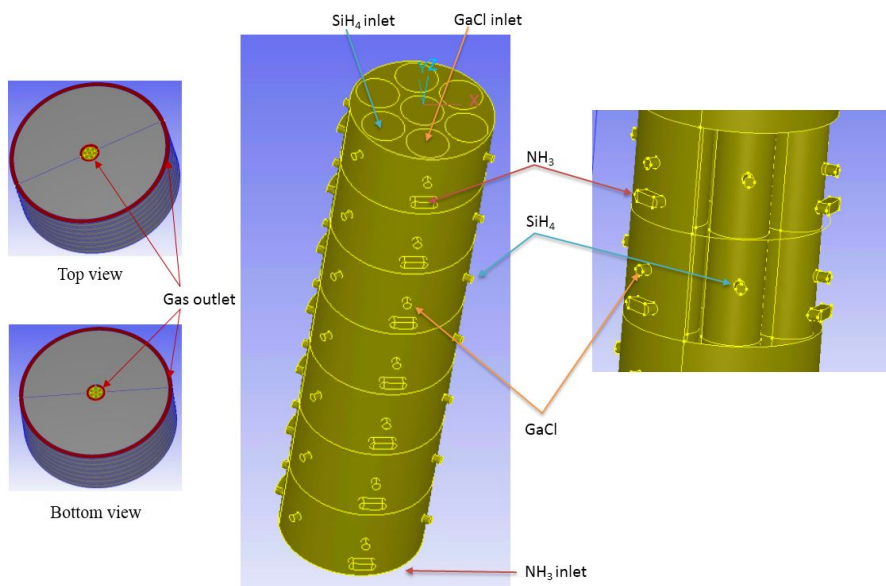


Figure 5.1 Schematic diagram of multi-layer simulation model.

5.3 Simulation conditions

5.3.1 Boundary conditions

The major conditions in the calculations are collected in the table 5.1. The temperature in the experiment is measured by the thermocouples, indicating that the temperature is 1213 K. Additionally, with the excellent thermal insulator, the deviation of the temperature between different susceptors is below 1 K. Thus, adiabatic condition is applied to the wall of the furnace and the temperature of the entire domain is constant. The pressure in the equipment is 1 Bar. The susceptors are rotating as a constant speed of 5 rpm. The reacting gases are transported into the nozzle with a constant volume per minute. The outlet type is constant pressure taking into account of the backflow. The deposition rate is calculated by the quasi-thermodynamics method, which has been mentioned in previous research [95]. The surface reactions occur at each surface of the susceptor from S1 to S7 shown in the figure 5.2.

Temperature	Pressure	Susceptor Rotation Speed	Inlet	Outlet	Wall
1213 K	1 Bar	5 rpm	Constant volume per minute	Constant pressure	Adiabatic

Table 5.1 Major conditions in the calculation

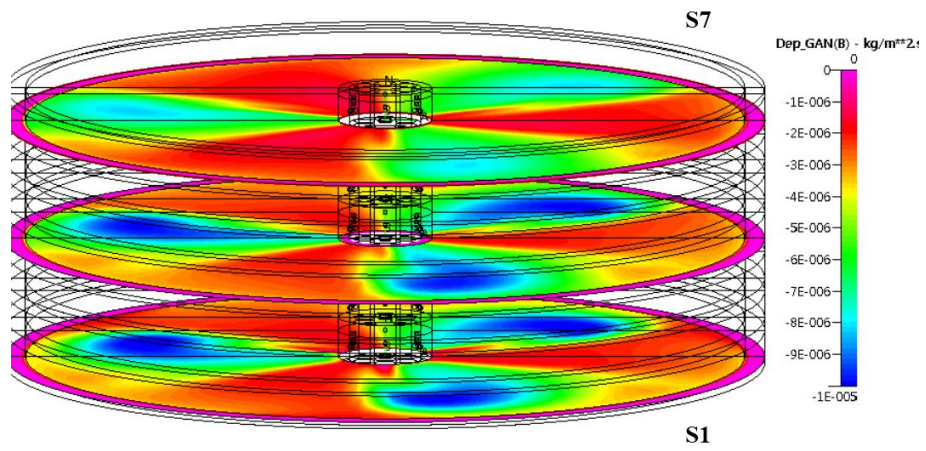


Figure 5.2 Deposition rate distribution at different susceptors. (Only S1, S4 and S7 are shown in the figure)

5.3.2 Volume conditions

The physical properties of the materials involved in this calculation are shown in the table 5.2. The density of gases has been calculated in the ideal gas law, which means that all kinds of gases both inside and outside the nozzle are compressible fluids. Heat capacity of gases is calculated by mix JANAF method that the value of heat capacity depends on temperature. Thermal conductivity and viscosity are handled by mix kinetic theory. And the mass diffusivity is considered as dimensionless Schmidt number 0.7. Moreover, the physical properties of susceptors are also shown in the table 5.2.

	Density	Heat capacity	Thermal conductivity	Viscosity	Mass diffusivity
Gases	Ideal gas law	Mix JANAF method	Mix kinetic theory	Mix kinetic theory	Schmidt number 0.7
Susceptors	2200 kg/m ³	670 J/kg • K	1.4 W/m • K		

Table 5.2 Physical properties of gases and susceptors employed in the calculation

5.4 Results and discussion

5.4.1 Fluid flow analysis

5.4.1.1 Fluid flow of GaCl

The velocity vector distributions at horizontal cross sections of GaCl and N₂ holes from susceptor 1 to susceptor 7 is shown in the figure 5.3. In order to clearly show all of the vectors with various velocities, the magnitude of the velocity vector is set as uniform. It can be obviously observed that a large amount of GaCl gas and nitrogen gas spray out from the 6 tubes separately. The maximum value of the legend is designated as 0.5 m/s, which is much lower than that of the maximum velocity at the gas holes, to indicate that the tube walls are well simulated by the “thin wall” option. By using the “thin wall” option, the thickness of the tube wall is 0, which is effectively separate the different gases. Additionally, the density of the vectors inside the nozzle is much higher than that outside the nozzle, for the reason that nozzle domain is constructed by unstructured grids, the density of which is required higher than structured grids to ensure the mesh quality. Moreover, it is confirmed that GaCl gas and nitrogen gas flow out from the nozzle with a high velocity and some of the gases flow back to nozzle surface between two adjacent gas holes, which is indicated from the vectors with opposite direction.

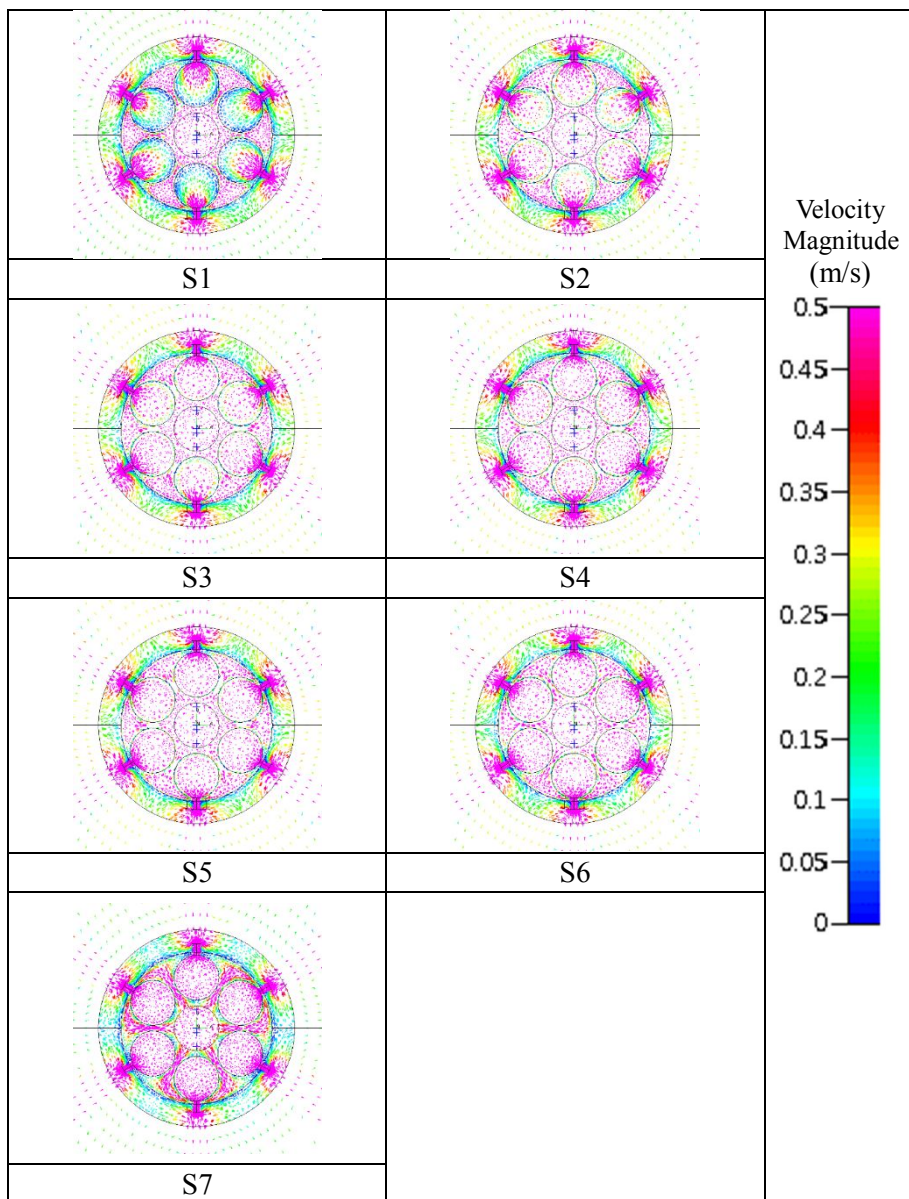


Figure 5.3 Velocity vector distribution at the horizontal cross section of GaCl & SiH₄ holes from susceptor 1 to susceptor 7.

5.4.1.2 Fluid flow of NH_3

The figure 5.4 shows velocity vector distributions at the horizontal cross sections of NH_3 holes from susceptor 1 to susceptor 7. As shown in the figure 5.1, the position of NH_3 holes are lower than the GaCl holes. The cross sections observed thereby are lower than the cross sections shown in the figure 5.3. As figure 5.4 shows, from top view, it can be seen that the caliber of NH_3 hole is larger than that of GaCl hole. And the NH_3 gas is squeezed out from the remaining part which is not occupied by the 6 small tubes. The central circle is not a tube, but just a circular gas inlet at the bottom surface of the nozzle. Like the previous section, the maximum value of the legend is designated as 0.5 m/s to indicate the positions of the tube walls. Among the results, the vector distribution of susceptor 1 is different from the others because susceptor 1 is close to the bottom of the nozzle, leading the velocity of the gases in the N_2 and GaCl tubes is smaller. In addition, it is shown that NH_3 gas flows out from the nozzle with a high velocity and some of the gas flows back to nozzle surface between two adjacent gas holes.

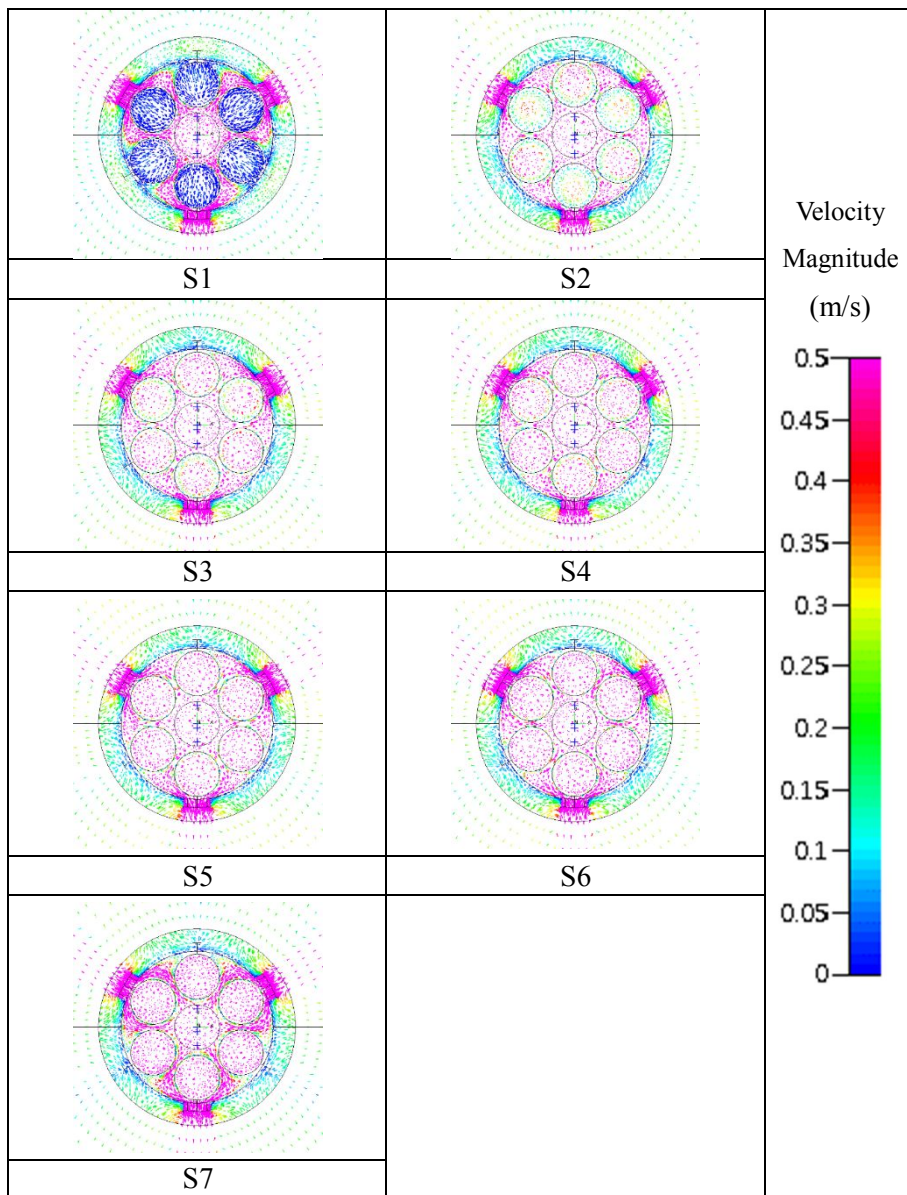


Figure 5.4 Velocity vector distribution at the horizontal cross section of NH_3 holes from susceptor 1 to susceptor 7.

5.4.4.3 Flow velocity at different susceptors

In the figure 5.5, velocity vector distribution at the vertical cross section has been calculated. In the figure, GaCl and NH₃ holes are located at the left side. N₂ holes are located at the right side. The results clearly show that GaCl and N₂ are fed from the top of the nozzle. At the same time, the NH₃ is transported from the center of bottom of the nozzle. Besides, the velocities at the N₂ holes are significantly larger than those of GaCl and NH₃.

From the result in figure 5.5, it is difficult to know the difference between different susceptors for each gas. So two line probes from S1 to S7 have been designated in front of GaCl holes and N₂ holes, respectively. The flow velocity magnitude distribution in front of GaCl and NH₃ has been obtained as shown in the figure 5.6. In the figure 5.6, the maximum velocities of GaCl and NH₃ appear alternately. The lower peaks represent NH₃ holes, and higher peaks represent GaCl holes. The velocities in front of GaCl holes are larger than those of NH₃, because the area of NH₃ hole is larger than that of GaCl hole. Moreover, the velocity in front of GaCl hole increases from S1 to S7. This trend could be explained by the transportation of GaCl from top to bottom. It is fair to say that more gas flow out from the upper holes than the lower holes. On the other hand, velocity in front of NH₃ holes also increases from S1 to S7. Due to the blockage of the GaCl and N₂ pipes, NH₃ gas could

not directly flow from the bottom to the lower holes. On the contrary, NH_3 tend to flow upward and go around the pipes to flow out from the upper holes.

Figure 5.7 shows the flow velocity magnitude distribution in front of N_2 holes from bottom to top. The velocity in front of N_2 holes also increases from S1 to S7. Because N_2 gas is transported from top to bottom. Overall, the flow rates of all the gases increase from bottom to top.

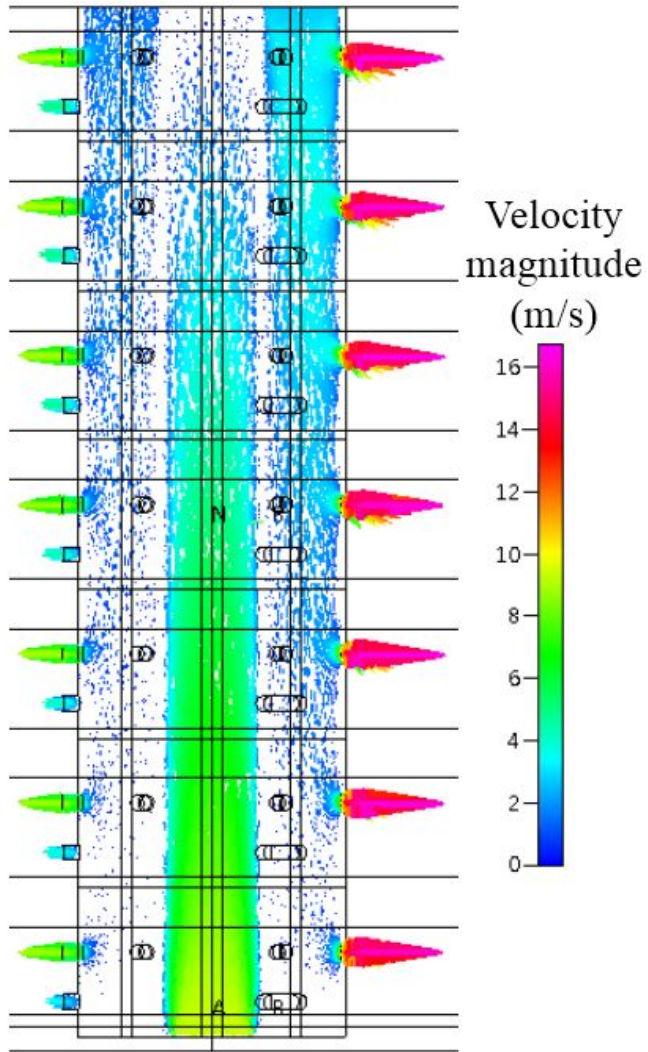


Figure 5.5 Velocity vector distribution at vertical cross section

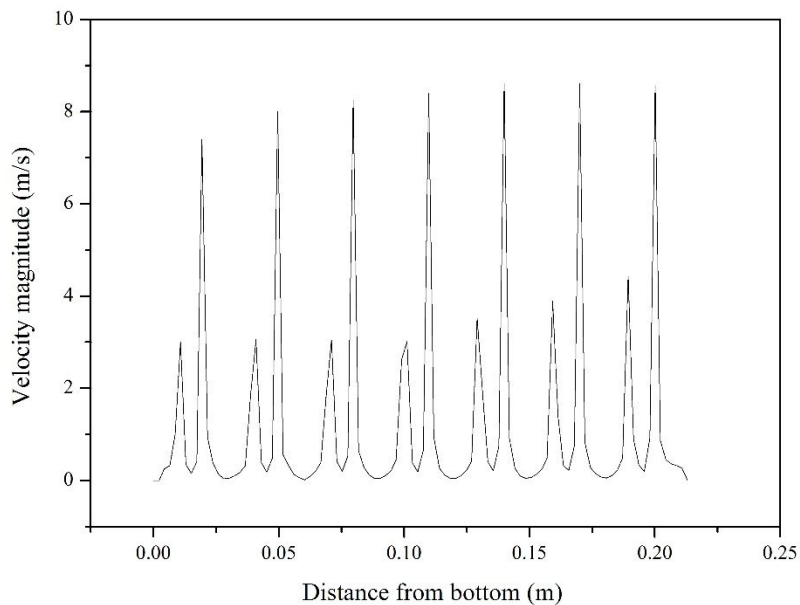


Figure 5.6 Flow velocity magnitude distribution in front of GaCl and NH₃ holes from bottom to top.

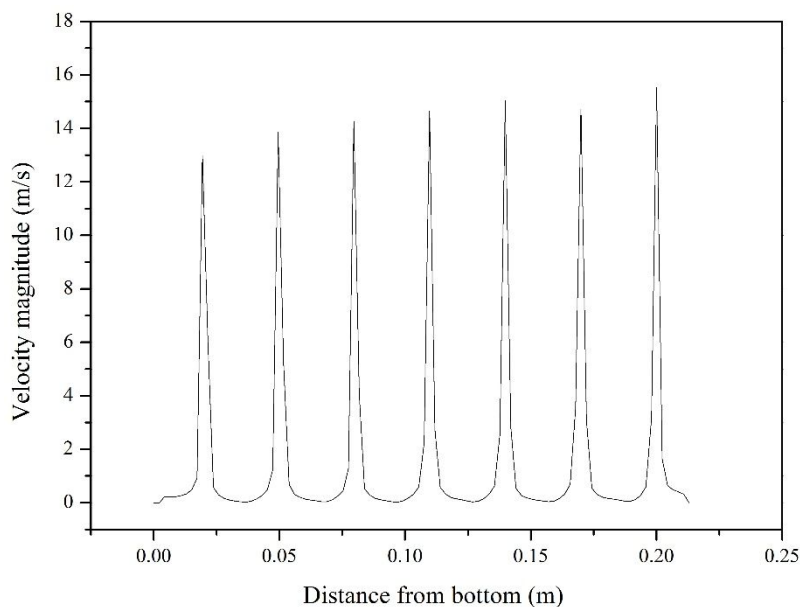


Figure 5.7 Flow velocity magnitude distribution in front of N₂ holes from bottom to top.

5.4.2 Deposition rate analysis

The uniformity of deposition thickness undoubtedly influences the quality of thin film. Due to the geometry of the horizontal HVPE, the unintentional non-uniform transportation of reacting gases results in an obviously non-uniform deposition distribution along the flow direction. Figure 5.8 shows deposition rate distribution at from susceptor 1 to susceptor 7. The pink color indicates high deposition rate and blue one indicates low deposition rate. The peripheral boundary is the gap between the susceptors and furnace wall, which is full of gases, showing a dark blue color. It is observed that all of the results show a 3-fold symmetrical pattern distribution due to the 3 directions of gas holes designed in the nozzle. From susceptor 2 to susceptor 7, the pink color becomes lighter which means the deposition rate diminishes gradually from susceptor 2 to susceptor 7. The peculiar phenomenon of low deposition rate at susceptor 1 could be explained by the nitrogen sucked into the susceptors from outlet, which dilutes the GaCl gas above susceptor 1. In the same way, a lot of nitrogen also flow into the gas above susceptor 7, decreasing the partial pressure of GaCl gas above susceptor 7, then decreasing the deposition rate at susceptor 7. This phenomenon will be discussed more evidently in the later sections.

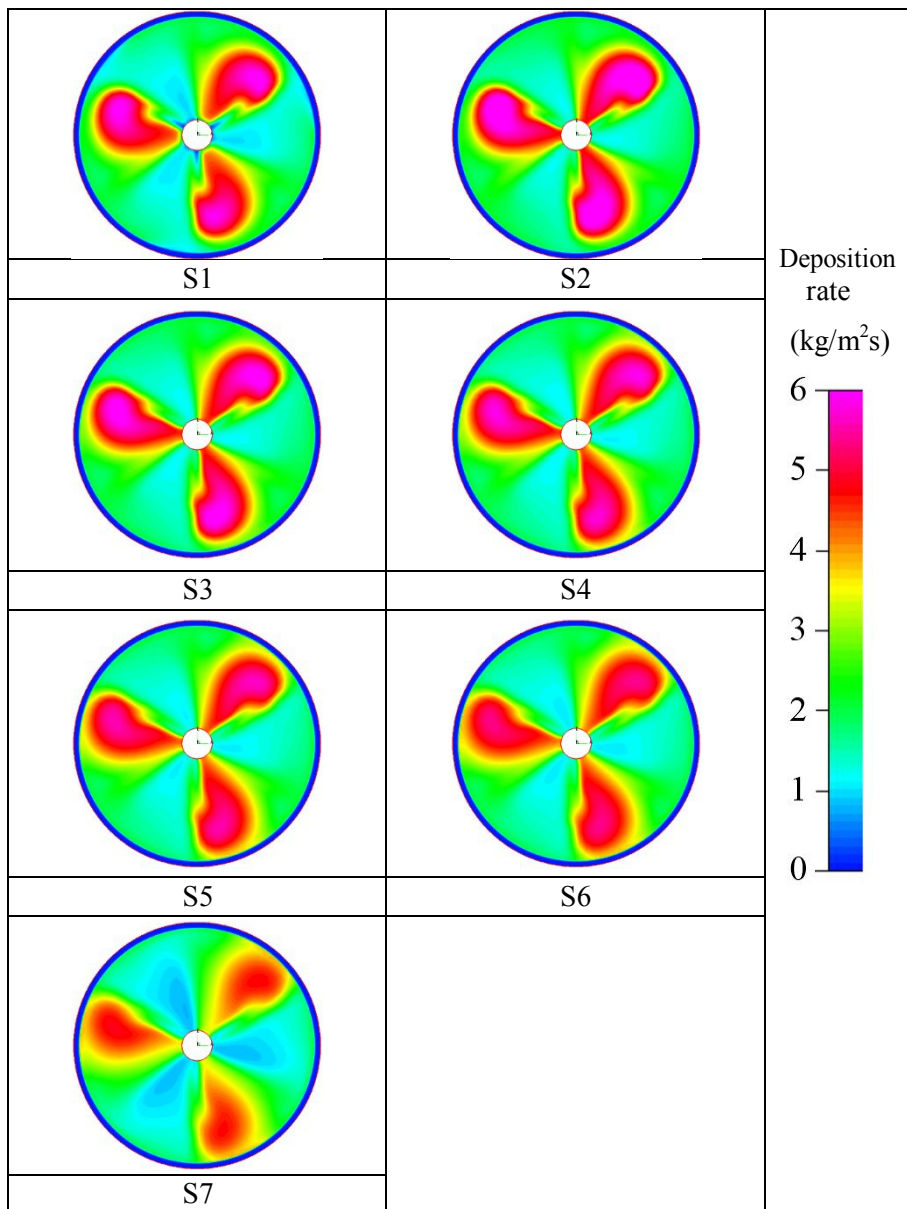


Figure 5.8 Deposition rate distributions at the different susceptors.

5.4.3 Reacting gas distribution analysis

5.4.3.1 GaCl analysis at horizontal cross section

Since the quantity of GaCl is much smaller than NH_3 , GaCl mass fraction distribution tremendously influence the deposition rate distribution. Figure 5.9 shows GaCl mass fraction distribution at 1mm above the susceptors. The distribution of GaCl mass fraction, which is also 3-fold symmetrical, is identical to the distribution of deposition rate. Moreover, the different quantities of GaCl between different susceptors cause the deposition deviation between different susceptors. It is confirmed that similar with the deposition rate distribution, GaCl mass fraction also decreases from susceptor 2 to susceptor 7.

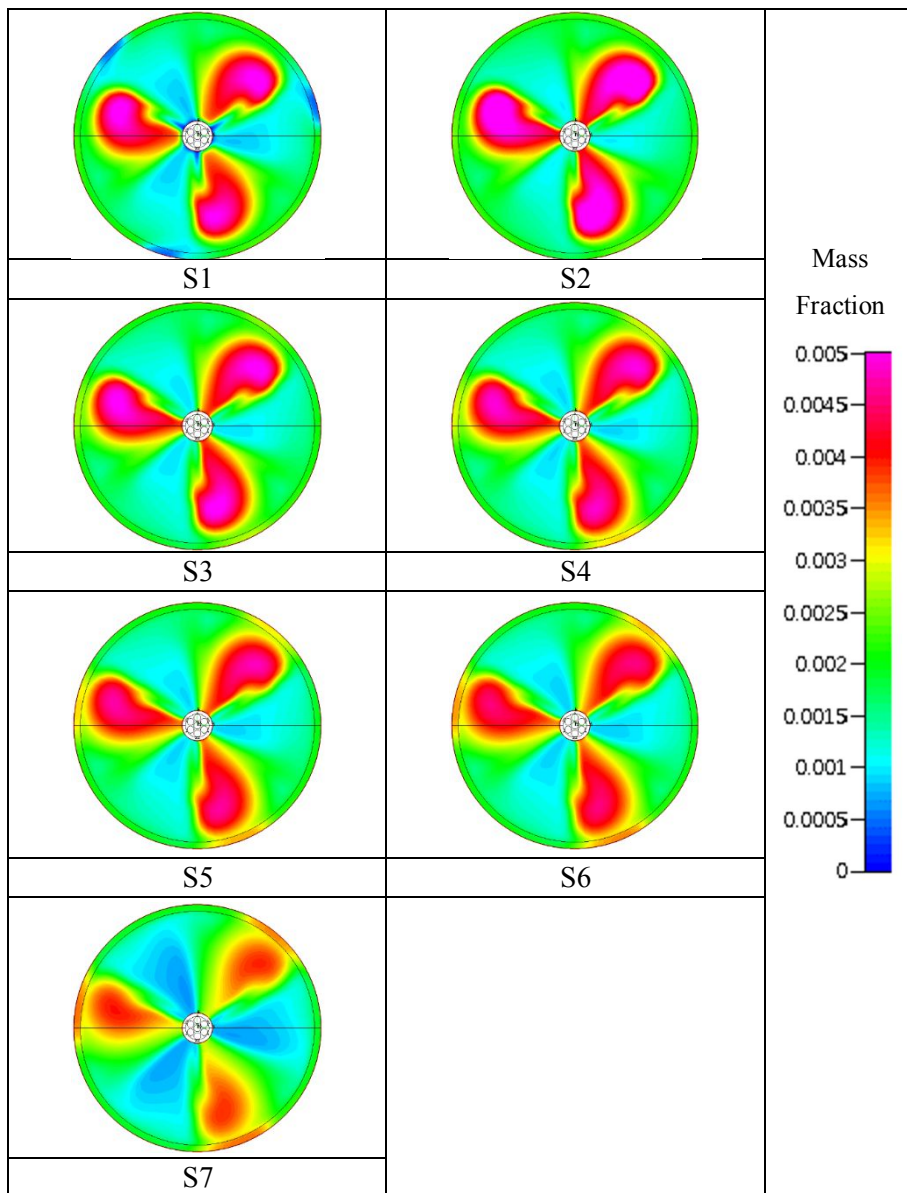
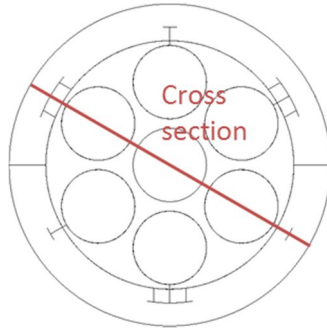


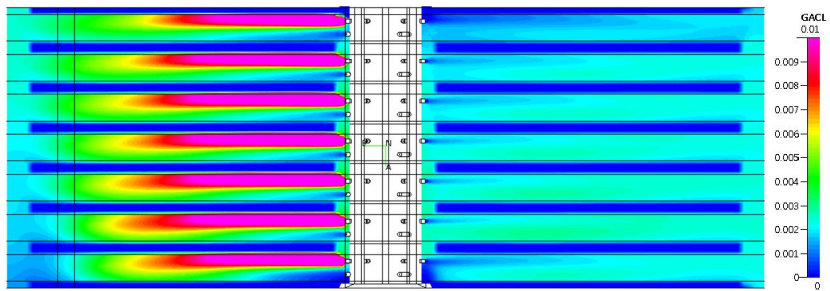
Figure 5.9 GaCl mass fraction distribution at 1mm above the susceptors.

5.4.3.2 GaCl and NH₃ analysis at vertical cross section

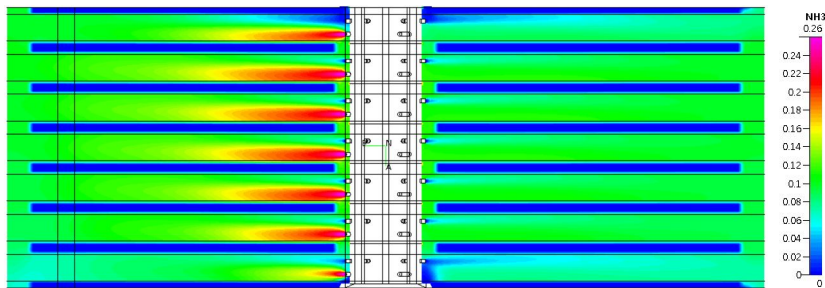
Regarding the limitation of reaction gas analysis at horizontal planes, GaCl and NH₃ mass fraction at vertical planes are also investigated in the simulation. Considering the symmetrical structure of the nozzle, the results are divided into two cases: the mass fraction profiles along the radial direction in front of the gas holes and the mass fraction profiles along the direction in the middle of two adjacent gas holes. Figure 5.10 shows GaCl mass fraction distribution and NH₃ mass fraction at vertical cross section along the radial direction in front of the gas holes. The cross section is also pointed out by the red line from top view. At the cross section plane, the left half is in front of the GaCl and NH₃ gas holes and the right half is in front of the SiH₄ gas holes. From the GaCl mass fraction distribution, it is illustrated that the mass fraction of GaCl gas injected from the nozzle decreases from susceptor 2 to susceptor 7. In contrast, the mass fraction of NH₃ gas injected from the nozzle increases from susceptor 1 to susceptor 6. As GaCl is insufficient compared with NH₃ in the experimental conditions, the deposition rate is consistent with GaCl distribution but not NH₃ distribution. Besides, the outlet, which is the gap between susceptors and nozzle at top and bottom, presents dark blue color from both of GaCl mass fraction distribution and NH₃ mass fraction distribution, providing the evidence for that a lot of nitrogen gases flow into the susceptors. The backflow of nitrogen gives rise to the phenomenon that susceptor 1 and susceptor 7 do not comply with the trend of other susceptors.



Cross section position from top view



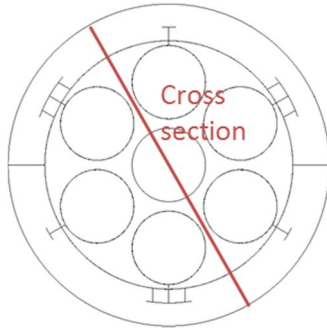
GaCl mass fraction distribution



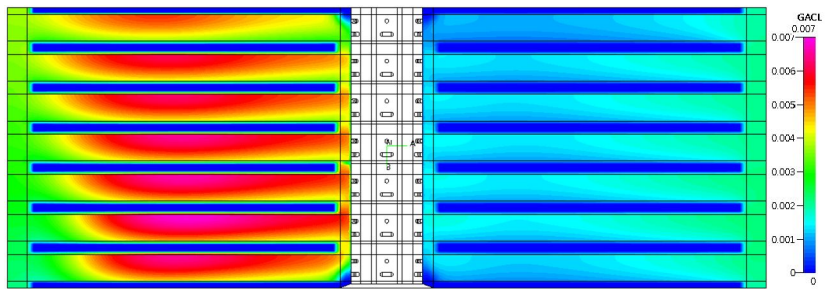
NH₃ mass fraction distribution

Figure 5.10 GaCl mass fraction distribution and NH₃ mass fraction at vertical cross section along the radial direction in front of the gas holes.

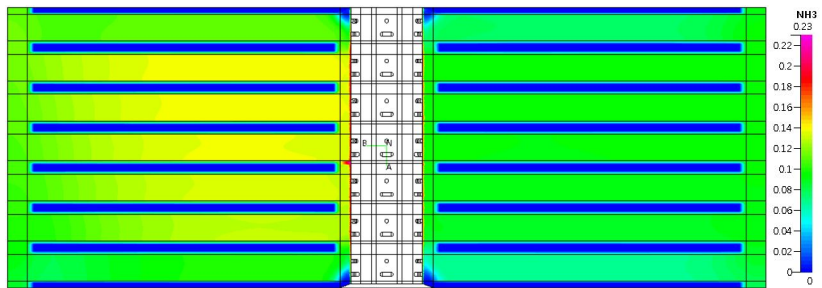
Figure 5.11 shows the GaCl and NH₃ mass fraction distribution at vertical cross section in the middle of two adjacent gas holes. Different from the previous cross section plane, both of the left half and right half are in the middle between GaCl gas holes and N₂ holes. The discrepancy between the left half and the right half is caused by the rotation of the susceptors. Both of the mass fraction distributions visibly reveal that a strong backflow occurs at the outlets between susceptors and nozzles, which supports the result of low deposition rates at susceptor 1 and susceptor 7.



Cross section position from top view



GaCl mass fraction distribution



NH₃ mass fraction distribution

Figure 5.11 GaCl mass fraction distribution and NH₃ mass fraction at vertical cross section in the middle of two adjacent gas holes.

5.4.4 Experimental verification of deposition rate

Figure 5.12 shows the experimental results of deposition rate distributions along the radial direction from susceptor 1 to susceptor 7. The curves of different susceptors cross with each other at the intersection, which is located at about 0.215 m away from the center. As a result of the experiment error, there is no noticeable trend between different susceptors. Especially the existence of the irregular result of susceptor 1 and susceptor 7 leads to a more complicated result to analyze. However, it is clearly confirmed that the deposition rates at all of the susceptors decrease along the radial direction. Correspondingly, calculation results are shown in the figure 5.13. The calculation results offer a more readable information to analyze. As previous section has discussed, susceptor 1 and susceptor 7 have lower GaCl partial pressures than they should have. This phenomenon is shown in the calculation results as well as experimental results evidently.

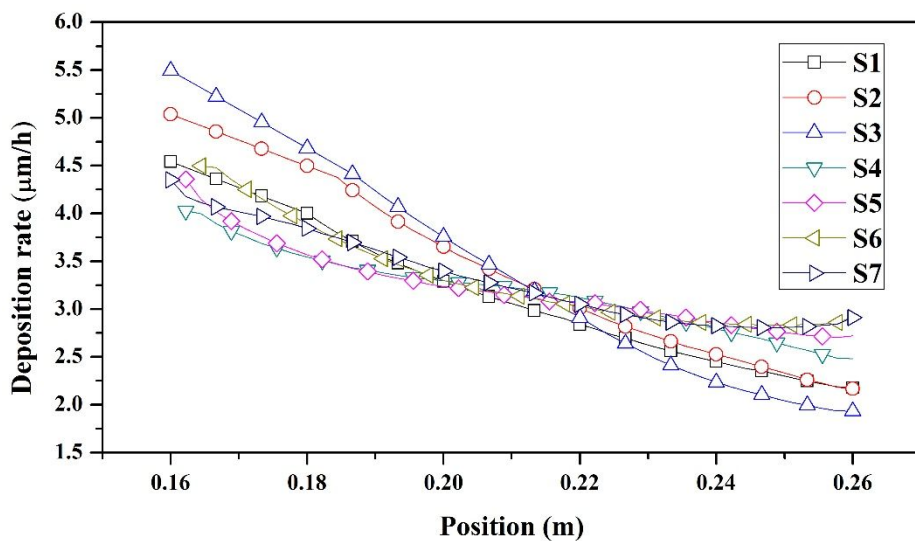


Figure 5.12 Experimental results of deposition rate distributions along the radial direction from susceptor 1 to susceptor 7.

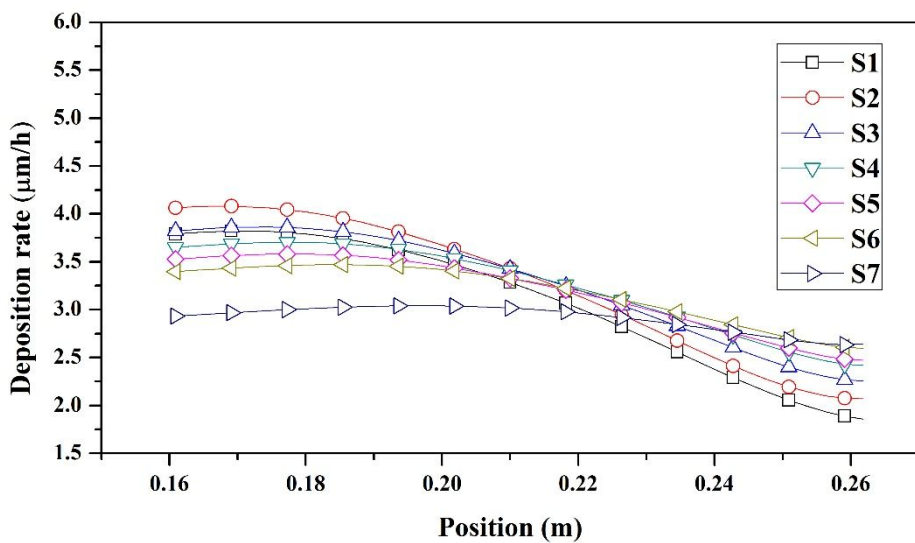


Figure 5.13 Calculation results of deposition rate distributions along the radial direction from susceptor 1 to susceptor 7.

To compare the calculation data with experimental data more readily, in the figure 5.14 and 5.15, susceptor 1 and 7 have been moved from both of them. S2 to S6 are renamed as S1 to S5. In the experimental result shown in the figure 5.14, at the upstream, S1 and S2 have higher deposition rates than S4 and S5. Nevertheless, at the downstream, S1 and S2 have lower deposition rates than S4 and S5. Accordingly, in the calculation result shown in the figure 5.15, the profiles of deposition rates provide a good fit to the experimental results and the trend is more homogeneous. Though there is a little difference between the deposition rate of calculation and that of experiment, yet the variation trend along the radial direction and variation trend from susceptor 1 to susceptor 5 are similar. There is also trivial discrepancy between the experimental results and calculation results, which is reasonably due to the assumptions of the simulation and errors of the experiment. In brief, the calculation result is adequately credible to reflect what has happened theoretically in the equipment in detail.

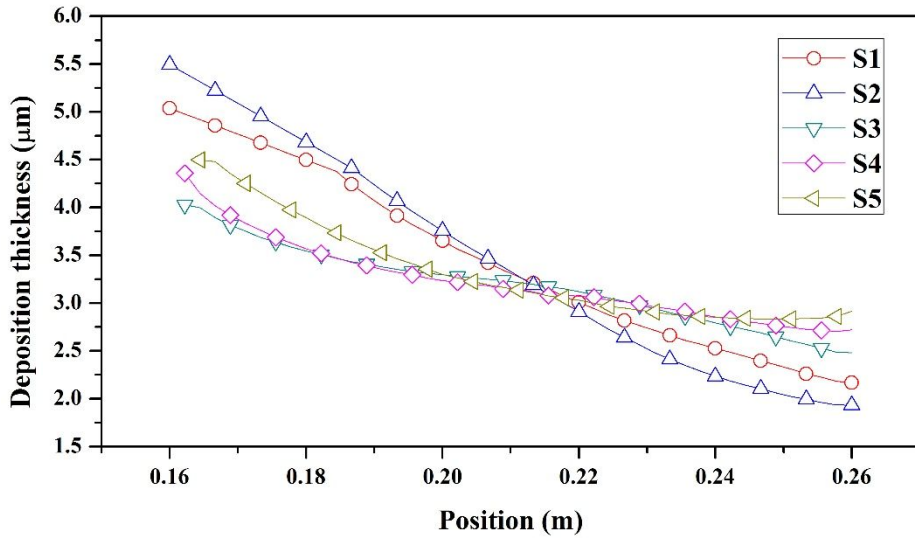


Figure 5.14 Experimental results of deposition thickness distributions along the radial direction from susceptor 1 to susceptor 5.

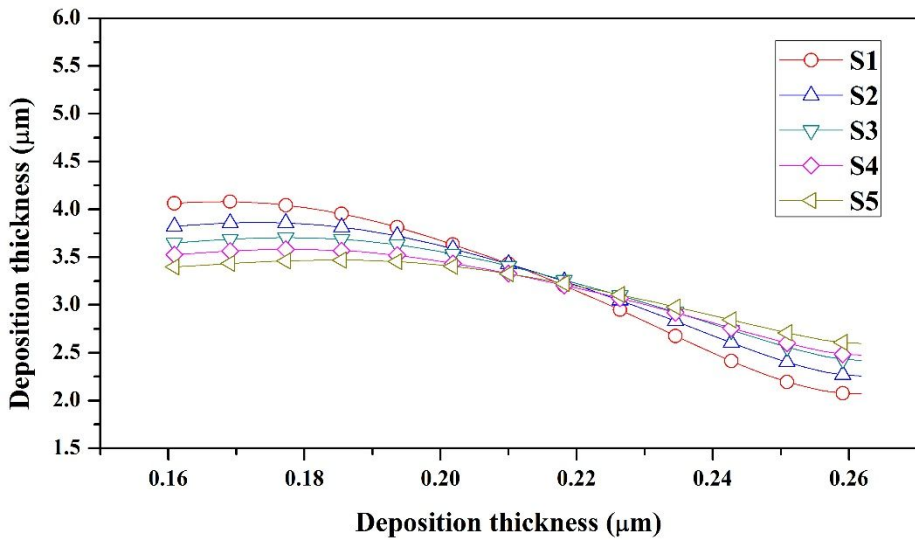


Figure 5.15 Calculation results of deposition rate distributions along the radial direction from susceptor 1 to susceptor 5.

We also have compared the standard deviation of deposition thickness between the experimental results and calculation results from different susceptors in the figure 5.16. Despite the discrepancy between the experimental results and calculation results, both of them display an obvious trend that the thickness of the deposition becomes uniform from S1 to S5.

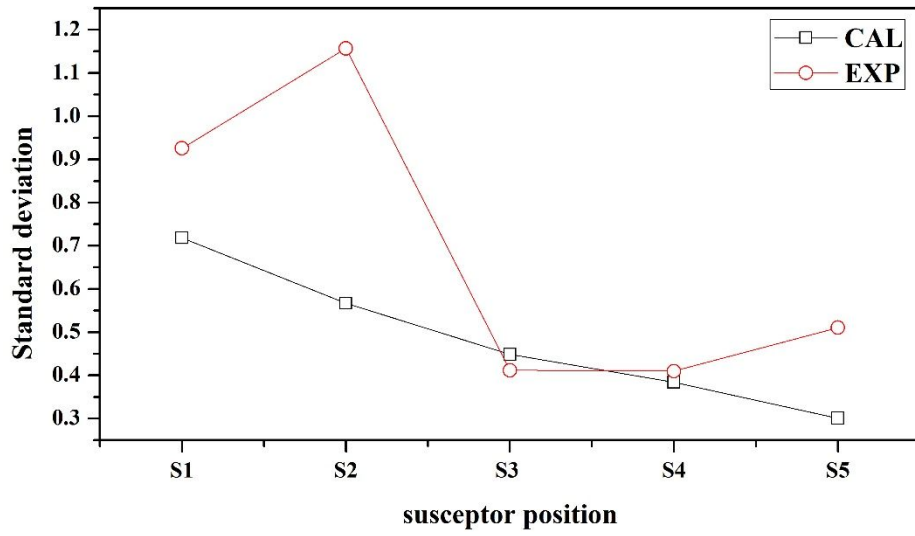
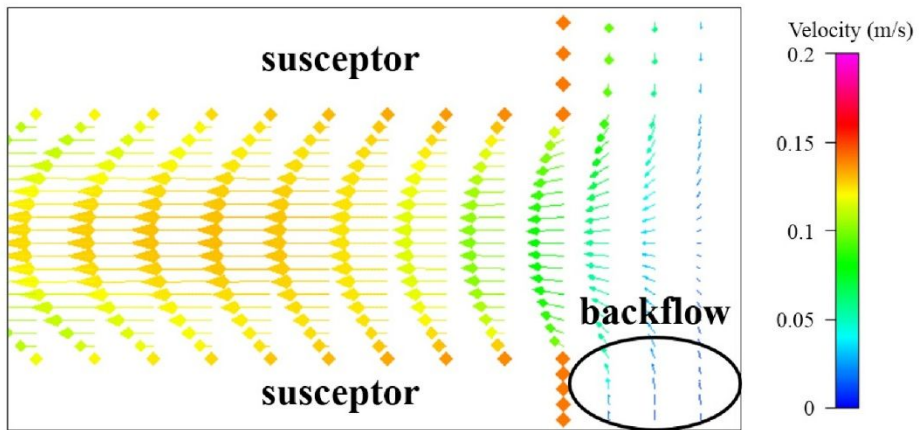


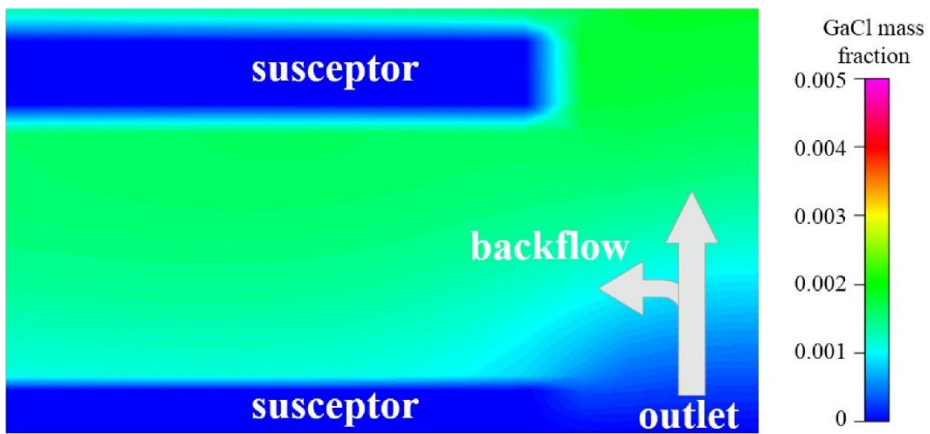
Figure 5.16 Comparison of the standard deviation of the deposition thickness between the calculation results and experimental results at different susceptors.

5.4.5 Effect of backflow

In order to investigate the difference of deposition thickness distribution between the five susceptors, the backflow at the outlet has been observed in detail. Because the backflow, which is composed of almost nitrogen carrier gas with a small amount of reacting gases, flows into the space between the susceptors from the gap between the susceptors and the furnace at the bottom as shown in the figure 5.17(a). Although the velocity of backflow is not large, yet the backflow obviously dilutes the GaCl gas shown in the figure 5.17(b) and decreases the partial pressure of the GaCl gases, giving rise to a lower deposition thickness at the downstream. Moreover, from the comparison of N₂ mass fraction between S1 and S7 (figure 5.18). The effect of backflow on the lower susceptors is more significant than that on the upper susceptors. Because the flow rates of the gases from upper holes are larger than lower holes, which could be confirmed in the figure 5.6 and figure 5.7. That is why low susceptors have thinner depositions than high susceptors at the downstream. As a result of the effect of backflow, all of the deposition thickness decreases from the upstream to downstream.



a



b

Figure 5.17 (a) Backflow velocity vector distribution at the outlet. (b) The GaCl mass distribution at the outlet.

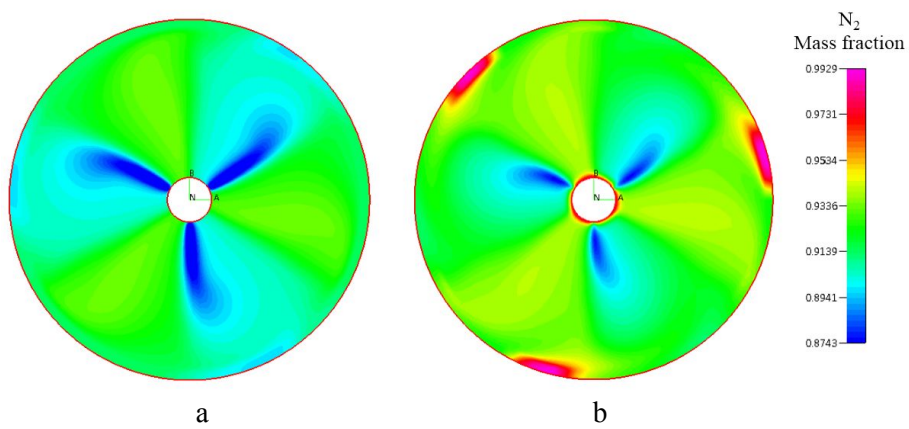


Figure 5.18 The N₂ mass fraction distribution at horizontal cross section: (a) S7 (b) S1.

5.4.6 V-III ratio distribution

V-III ratio has a significant effect on the surface morphology of the thin film of III-nitride semiconductors [114-116]. In this study, the V-III ratio that we discussed is not the molar ratio of total amount of group V elements to group III elements but rather the molar ratio of NH_3 to GaCl at the surface of the GaN deposition. Figure 5.19 shows the calculated V-III ratio along the radial direction from S1 to S5. The V-III ratio is collected at 1 mm above the GaN surface. The curves in the figure 5.19 present two major trends. Firstly, the V-III ratio becomes larger from S1 to S5 at the upstream, and the V-III ratio becomes smaller from S1 to S5 at the downstream. Secondly, along the flow direction, the V-III ratio increases for all the susceptors.

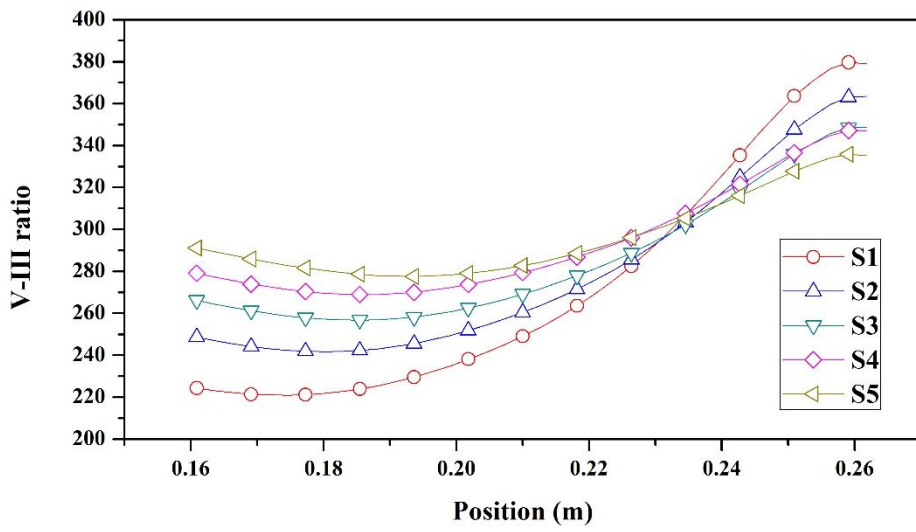


Figure 5.19 Calculated V-III ratio along the radial direction from susceptor 1 to susceptor 5.

5.4.7 Experimental verification of V-III ratio distribution

Besides the measurements of the growth rates, the pits also have been observed when we investigated the surface morphology by the OLS4000 3D laser measuring microscope (figure 5.20). Pit is an ordinary defect in III-nitrides thin film, which is always accompanied by threading dislocations [96, 117-120]. Threading dislocation is also a common dislocation in the GaN thin film [121, 122]. The figure 5.16 shows the surface morphology of GaN thin film observed by laser measuring microscope from S1 to S5. As shown in the figure 5.20, we have selected 3 points to observe the surface morphology: The top point is the apex of the wafer where is closest to the gas inlets; the center point is located at the center of the wafer; the flat point is the tail of the wafer, where is the farthest point from the gas inlets. In the figure 5.20, consistent with the calculation results, we can conclude that there are also two obvious trends in the experimental results. Firstly, at the top of wafers, the density of pits significantly decreases from S1 to S5. Secondly, along the flow direction, the density of the pits decreases for all the susceptors.

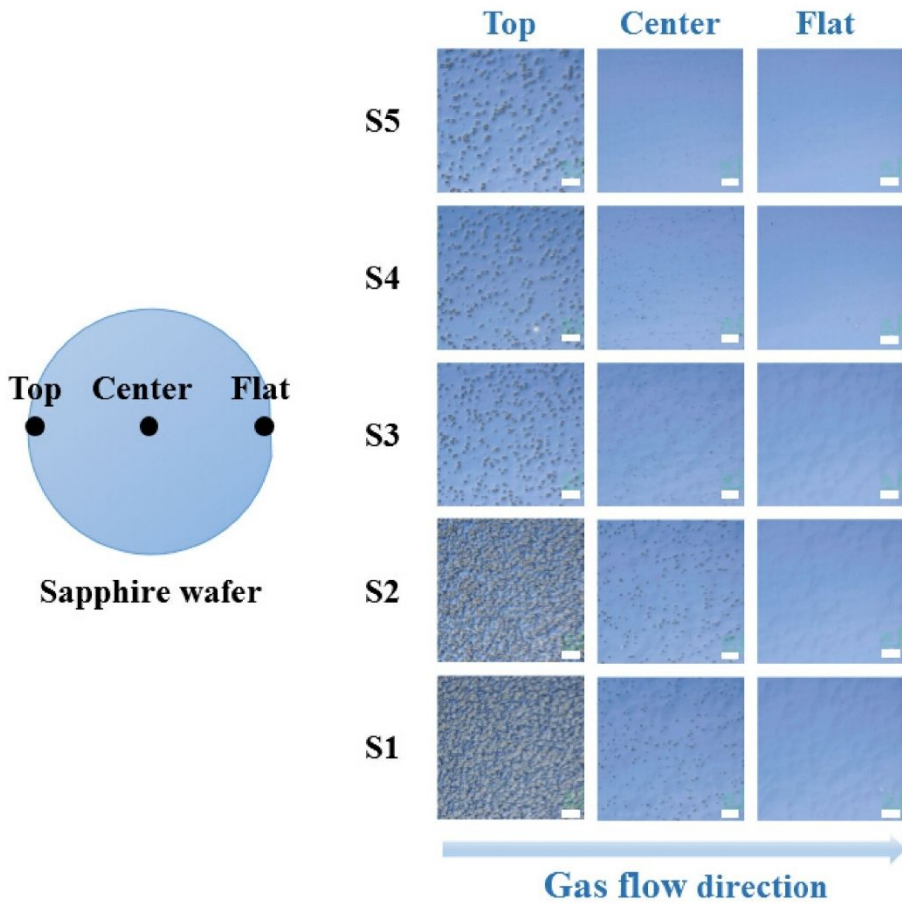


Figure 5.20 Surface morphology of GaN thin film from susceptor 1 to susceptor 5.

5.5 Summary

In this chapter, a multi-susceptor model considering mass transfer, fluid flow and chemical deposition has been developed to investigate the deposition rate and V-III ratio at different susceptors. The calculated deposition thickness provides a good fit with the deposition thickness measured in the experiments, regarding the model as a high reliable analysis tool. It is found in both of the calculation results and experimental results that at each susceptor, the deposition rate decreases from center to periphery. And the uniformity of the deposition thickness becomes better from low susceptor to high susceptor. Moreover, through the calculation model, V-III ratio distribution at 1mm distance above the deposition surface has been achieved. V-III ratio increases from center to periphery for all of the susceptors. At the upstream, V-III ratio increases from S1 to S5. Accordingly, in the experiments, it is observed that the density of pits becomes lower from S1 to S5 and from top point to flat point. Since the temperature variation in the entire stacks of susceptors is accurately controlled below 1K, we speculate that the primary factor affects the density of pits is the V-III ratio. Therefore, through the comparison between the calculation results and experimental results, it is fair to assert that the calculation model can be employed to predict the pits distribution and prevent the pits from forming before the mass production for the multi-susceptor equipment in the future research.

Chapter 6. Conclusions

In this study, we have developed single layer model and multi-layer model to investigate the effect of operating parameters on the uniformity of GaN deposition thin film, the effect of non-uniform deposition rate on the hillocks formation and the relation between V-III ratio and pits formation, respectively.

In the single layer model, with regard to the uniformity of deposition thickness along the radial direction, high carrier gas flow rate, high temperature, low pressure, low rotation speed and nitrogen as the carrier gas are the optimized conditions. However, it can be concluded that the exclusive condition that high temperature could not only improves the uniformity of the deposition thickness but also saves processing time. In contrast, the other conditions beneficial to the high uniformity such as high carrier gas flow rate, low pressure, low rotation speed and the carrier gas without hydrogen result in a long processing time. Besides, through the comparison between the calculation results and experimental results, it is investigated that the high density of the hillocks is caused by the non-uniform deposition rate. We suggests that increasing the rotation speed will decrease the density of the hillocks.

In the multi-layer model, through the flow fluid analysis, it is confirmed that the backflow of nitrogen has significantly influenced the mass fraction

distribution of the gases above the susceptor 1 and susceptor 7, leading to unusually different behaviors of gas distributions and deposition rate distributions of susceptor 1 and susceptor 7. Through the comparison between the experimental results and calculation results, current research validates the view that there is a precise relationship between V-III ratio and the formation of pits. Therefore, the multi-layer model could be employed to predict the pits formation in the future study and production.

References

- [1] P. Bogusl, E. Briggs, J. Bernholc, Native defects in gallium nitride, *Physical Review B*, 51 (1995) 17255.
- [2] L. Liu, J.H. Edgar, Substrates for gallium nitride epitaxy, *Materials Science and Engineering: R: Reports*, 37 (2002) 61-127.
- [3] F. Scholz, Semipolar GaN grown on foreign substrates: a review, *Semiconductor Science and Technology*, 27 (2012) 024002.
- [4] E.F. Schubert, *Light-Emitting Diodes second edition*, (2006).
- [5] S. Nakamura, M. Senoh, S.-i. Nagahama, N. Iwasa, T. Yamada, T. Matsushita, H. Kiyoku, Y. Sugimoto, InGaN-based multi-quantum-well-structure laser diodes, *Japanese Journal of Applied Physics*, 35 (1996) L74.
- [6] S. Nakamura, M. Senoh, S.-i. Nagahama, N. Iwasa, T. Yamada, T. Matsushita, H. Kiyoku, Y. Sugimoto, T. Kozaki, H. Umemoto, Present status of InGaN/GaN/AlGaN-based laser diodes, *Journal of crystal growth*, 189 (1998) 820-825.
- [7] S. Nakamura, InGaN/GaN/AlGaN-based laser diodes grown on free-standing GaN substrates, *Materials Science and Engineering: B*, 59 (1999) 370-375.

- [8] S. Nakamura, InGaN-based blue light-emitting diodes and laser diodes, *Journal of crystal growth*, 201 (1999) 290-295.
- [9] B. Beaumont, P. Gibart, J.P. Faurie, Nitrogen precursors in metalorganic vapor phase epitaxy of (Al,Ga)N, *Journal of Crystal Growth*, 156 (1995) 140-146.
- [10] Q. Bao, M. Saito, K. Hazu, K. Furusawa, Y. Kagamitani, R. Kayano, D. Tomida, K. Qiao, T. Ishiguro, C. Yokoyama, Ammonothermal crystal growth of GaN using an NH₄F mineralizer, *Crystal Growth & Design*, 13 (2013) 4158-4161.
- [11] M. Meneghini, L.-R. Trevisanello, G. Meneghesso, E. Zanoni, A review on the reliability of GaN-based LEDs, *Device and Materials Reliability, IEEE Transactions on*, 8 (2008) 323-331.
- [12] M. Boćkowski, I. Grzegory, S. Krukowski, B. Łuczniak, Z. Romanowski, M. Wróblewski, J. Borysiuk, J. Weyher, P. Hageman, S. Porowski, Directional crystallization of GaN on high-pressure solution grown substrates by growth from solution and HVPE, *Journal of crystal growth*, 246 (2002) 194-206.
- [13] W.V. Lundin, E.E. Zavarin, D.S. Sizov, M.A. Sinitsin, A.F. Tsatsul'nikov, A.V. Kondratyev, E.V. Yakovlev, R.A. Talalaev, Effects of reactor pressure and residence time on GaN MOVPE growth efficiency, *Journal of Crystal Growth*, 287 (2006) 605-609.

- [14] A. Hirako, K. Ohkawa, Effect of thermal radiation and absorption in GaN-MOVPE growth modeling on temperature distribution and chemical state, *Journal of Crystal Growth*, 276 (2005) 57-63.
- [15] S.Y. Karpov, V. Prokofyev, E. Yakovlev, R. Talalaev, Novel approach to simulation of group-III nitrides growth by MOVPE, *MRS Internet Journal of Nitride Semiconductor Research*, 4 (1999) 1.
- [16] A. Koukitu, T. Taki, N. Takahashi, H. Seki, Thermodynamic study on the role of hydrogen during the MOVPE growth of group III nitrides, *Journal of crystal growth*, 197 (1999) 99-105.
- [17] H. Moffat, K.F. Jensen, Complex flow phenomena in MOCVD reactors: I. Horizontal reactors, *Journal of Crystal Growth*, 77 (1986) 108-119.
- [18] K. Fujito, S. Kubo, H. Nagaoka, T. Mochizuki, H. Namita, S. Nagao, Bulk GaN crystals grown by HVPE, *Journal of Crystal Growth*, 311 (2009) 3011-3014.
- [19] C. Hemmingsson, G. Pozina, Optimization of low temperature GaN buffer layers for halide vapor phase epitaxy growth of bulk GaN, *Journal of Crystal Growth*, 366 (2013) 61-66.
- [20] Y. Development, http://www.ledlighting-eetimes.com/en/general-lighting-applications-drive-led-market.html?cmp_id=7&news_id=222908773, (September 2013).

- [21] J. Karpiński, S. Porowski, S. Miotkowska, High pressure vapor growth of GaN, *Journal of Crystal Growth*, 56 (1982) 77-82.
- [22] J. Karpiński, J. Jun, S. Porowski, Equilibrium pressure of N₂ over GaN and high pressure solution growth of GaN, *Journal of Crystal Growth*, 66 (1984) 1-10.
- [23] I. Grzegory, High pressure growth of bulk GaN from solutions in gallium, *Journal of Physics: Condensed Matter*, 13 (2001) 6875.
- [24] I. Grzegory, M. Boćkowski, B. Łuczniak, S. Krukowski, Z. Romanowski, M. Wroblewski, S. Porowski, Mechanisms of crystallization of bulk GaN from the solution under high N₂ pressure, *Journal of crystal growth*, 246 (2002) 177-186.
- [25] I. Grzegory, S. Krukowski, Synthesis and Crystal Growth of AlInBV Semiconducting Compounds Under High Pressure of Nitrogen, *Physica Scripta*, 1991 (1991) 242.
- [26] I. Grzegory, M. Bockowski, B. Lucznik, S. Krukowski, M. Wroblewski, S. Porowski, Recent Results in the Crystal Growth of GaN at High N₂ Pressure, *MRS Internet Journal of Nitride Semiconductor Research*, 1 (1996) e20.
- [27] B. Łuczniak, B. Pastuszka, I. Grzegory, M. Boćkowski, G. Kamler, E. Litwin-Staszewska, S. Porowski, Deposition of thick GaN layers by

- HVPE on the pressure grown GaN substrates, *Journal of Crystal Growth*, 281 (2005) 38-46.
- [28] M. Boćkowski, M. Wroblewski, B. Łuczniak, I. Grzegory, Crystal growth of aluminum nitride under high pressure of nitrogen, *Materials Science in Semiconductor Processing*, 4 (2001) 543-548.
- [29] M. Bockowski, P. Strak, I. Grzegory, B. Lucznik, S. Porowski, GaN crystallization by the high-pressure solution growth method on HVPE bulk seed, *Journal of Crystal Growth*, 310 (2008) 3924-3933.
- [30] M. Bockowski, I. Grzegory, B. Lucznik, T. Sochacki, G. Nowak, B. Sadovyi, P. Strak, G. Kamler, E. Litwin-Staszewska, S. Porowski, Multi feed seed (MFS) high pressure crystallization of 1–2in GaN, *Journal of Crystal Growth*, 350 (2012) 5-10.
- [31] H. Yamane, M. Shimada, S.J. Clarke, F.J. DiSalvo, Preparation of GaN single crystals using a Na flux, *Chemistry of materials*, 9 (1997) 413-416.
- [32] H. Yamane, M. Shimada, T. Sekiguchi, F.J. DiSalvo, Morphology and characterization of GaN single crystals grown in a Na flux, *Journal of crystal growth*, 186 (1998) 8-12.
- [33] M. Aoki, H. Yamane, M. Shimada, S. Sarayama, F.J. DiSalvo, GaN single crystal growth using high-purity Na as a flux, *Journal of crystal growth*, 242 (2002) 70-76.

- [34] A. Denis, G. Goglio, G. Demazeau, Gallium nitride bulk crystal growth processes: A review, *Materials Science and Engineering: R: Reports*, 50 (2006) 167-194.
- [35] H. Yamane, M. Shimada, T. Endo, F.J. DISALVO, Crystal Growth of GaN from Na-Ga Melt in BN Containers, *Journal of the Ceramic Society of Japan (日本セラミックス協会学術論文誌)*, 107 (1999) 925-929.
- [36] M. Aoki, H. Yamane, M. Shimada, T. Sekiguchi, T. Hanada, T. Yao, S. Sarayama, F.J. DiSalvo, Growth of GaN single crystals from a Na-Ga melt at 750° C and 5MPa of N₂, *Journal of crystal growth*, 218 (2000) 7-12.
- [37] R. Dwiliński, A. Wyszomolek, J. Baranowski, M. Kamińska, R. Doradziński, J. Garczyński, L. Sierzputowski, H. Jacobs, GaN synthesis by ammonothermal method, *Acta Physica Polonica A*, 88 (1995) 833-836.
- [38] R. Dwiliński, J. Baranowski, M. Kamińska, R. Doradziński, J. Garczyński, L. Sierzputowski, On GaN crystallization by ammonothermal method, *Acta Physica Polonica A*, 90 (1996) 763-766.
- [39] R. Dwiliński, R. Doradziński, J. Garczyński, L. Sierzputowski, J. Baranowski, M. Kamińska, Exciton photo-luminescence of GaN bulk crystals grown by the AMMONO method, *Materials Science and Engineering: B*, 50 (1997) 46-49.

- [40] Q.-S. Chen, J.-Y. Yan, Y.-N. Jiang, W. Li, Modeling on ammonothermal growth of GaN semiconductor crystals, *Progress in Crystal Growth and Characterization of Materials*, 58 (2012) 61-73.
- [41] J. Erlekampf, J. Seebeck, P. Savva, E. Meissner, J. Friedrich, N. Alt, E. Schlücker, L. Frey, Numerical time-dependent 3D simulation of flow pattern and heat distribution in an ammonothermal system with various baffle shapes, *Journal of Crystal Growth*, 403 (2014) 96-104.
- [42] S. Pimputkar, S. Kawabata, J. Speck, S. Nakamura, Improved growth rates and purity of basic ammonothermal GaN, *Journal of Crystal Growth*, 403 (2014) 7-17.
- [43] H. Amano, N. Sawaki, I. Akasaki, Y. Toyoda, Metalorganic vapor phase epitaxial growth of a high quality GaN film using an AlN buffer layer, *Applied Physics Letters*, 48 (1986) 353-355.
- [44] A. Sakai, H. Sunakawa, A. Usui, Defect structure in selectively grown GaN films with low threading dislocation density, *Applied Physics Letters*, 71 (1997) 2259-2261.
- [45] S. Kim, J. Oh, J. Kang, D. Kim, J. Won, J.W. Kim, H.-K. Cho, Two-step growth of high quality GaN using V/III ratio variation in the initial growth stage, *Journal of crystal growth*, 262 (2004) 7-13.

- [46] D.D. Koleske, M.E. Coltrin, K.C. Cross, C.C. Mitchell, A.A. Allerman, Understanding GaN nucleation layer evolution on sapphire, *Journal of Crystal Growth*, 273 (2004) 86-99.
- [47] C. Roder, S. Einfeldt, S. Figge, D. Hommel, Temperature dependence of the thermal expansion of GaN, *Physical Review B*, 72 (2005).
- [48] T. Bergunde, F. Durst, L. Kadinski, Y.N. Makarov, M. Schäfer, M. Weyers, Modelling of growth in a 5 X 3 inch multiwafer metalorganic vapour phase epitaxy reactor, *Journal of crystal growth*, 145 (1994) 630-635.
- [49] L. Kadinski, V. Merai, A. Parekh, J. Ramer, E. Armour, R. Stall, A. Gurary, A. Galyukov, Y. Makarov, Computational analysis of GaN/InGaN deposition in MOCVD vertical rotating disk reactors, *Journal of crystal growth*, 261 (2004) 175-181.
- [50] A. Bouteville, Numerical simulation applied to chemical vapor deposition process, rapid thermal CVD and spray CVD, *J. Optoelectronics and Advanced Materials*, 7 (2005) 599-606.
- [51] M.-L. Tsai, C.-C. Fang, L.-Y. Lee, Numerical simulation of the temperature distribution in a planetary MOCVD reactor, *Chemical Engineering and Processing: Process Intensification*, 81 (2014) 48-58.

- [52] M. Akiyama, Y. Kawarada, K. Kaminishi, Growth of Single Domain GaAs Layer on (100)-Oriented Si Substrate by MOCVD, Japanese Journal of Applied Physics Part 2-Letters, 23, L843, (1984).
- [53] Y.-C. Chuang, C.-T. Chen, Mathematical modeling and optimal design of an MOCVD reactor for GaAs film growth, Journal of the Taiwan Institute of Chemical Engineers, 45 (2014) 254-267.
- [54] T. Morishita, M. Iwaya, T. Takeuchi, S. Kamiyama, I. Akasaki, Homoepitaxial growth of AlN layers on freestanding AlN substrate by metalorganic vapor phase epitaxy, Journal of Crystal Growth, 390 (2014) 46-50.
- [55] Q. Bao, T. Zhu, N. Zhou, S. Guo, J. Luo, C. Zhao, Effect of hydrogen carrier gas on AlN and AlGa_N growth in AMEC Prismo D-Blue® MOCVD platform, Journal of Crystal Growth, 419 (2015) 52-56.
- [56] R. Dupuis, Epitaxial growth of III–V nitride semiconductors by metalorganic chemical vapor deposition, Journal of crystal growth, 178 (1997) 56-73.
- [57] L. Rodak, K. Kasarla, D. Korakakis, Effect of gas flow on the selective area growth of gallium nitride via metal organic vapor phase epitaxy, Journal of crystal growth, 306 (2007) 75-79.
- [58] Aixtron, http://www.aixtron.com/fileadmin/documents/Technologien/Produktblatt_AIX_2800G4-TM_low.pdf.

- [59] J. Pankove, J. Berkeyheiser, H. Maruska, J. Wittke, Luminescent properties of GaN, *Solid State Communications*, 8 (1970) 1051-1053.
- [60] R. Molnar, W. Götz, L. Romano, N. Johnson, Growth of gallium nitride by hydride vapor-phase epitaxy, *Journal of Crystal Growth*, 178 (1997) 147-156.
- [61] S. Nakamura, GaN growth using GaN buffer layer, *Japanese Journal of Applied Physics*, 30 (1991) L1705.
- [62] A. Usui, H. Sunakawa, A. Sakai, A.A. Yamaguchi, Thick GaN epitaxial growth with low dislocation density by hydride vapor phase epitaxy, *Japanese Journal of Applied Physics, Part 2: Letters*, 36 (1997) L899-L902.
- [63] C. Sasaoka, H. Sunakawa, A. Kimura, M. Nido, A. Usui, A. Sakai, High-quality InGaN MQW on low-dislocation-density GaN substrate grown by hydride vapor-phase epitaxy, *Journal of crystal growth*, 189 (1998) 61-66.
- [64] M.K. Kelly, R.P. Vaudo, V.M. Phanse, L. Görgens, O. Ambacher, M. Stutzmann, Large free-standing GaN substrates by hydride vapor phase epitaxy and laser-induced liftoff, *Japanese journal of applied physics*, 38 (1999) L217.
- [65] C. Kim, M. Yang, W. Lee, J. Yi, S. Kim, Y. Choi, T.-K. Yoo, S.T. Kim, Formation and characteristics of inversion domain in GaN grown by

- hydride vapor-phase epitaxy, *Journal of Crystal Growth*, 213 (2000) 235-240.
- [66] E.V. Etzkorn, D.R. Clarke, Cracking of GaN films, *Journal of Applied Physics*, 89 (2001) 1025.
- [67] D. Martin, J. Carlin, V. Wagner, H. Bühlmann, M. Ilegems, In-Situ Monitoring of GaN Growth by Hydride Vapor Phase Epitaxy, *physica status solidi (a)*, 194 (2002) 520-523.
- [68] M. Amilusik, T. Sochacki, B. Łuczniak, M. Boćkowski, B. Sadovyi, A. Presz, I. Dziećielewski, I. Grzegory, Analysis of self-lift-off process during HVPE growth of GaN on MOCVD-GaN/sapphire substrates with photolithographically patterned Ti mask, *Journal of Crystal Growth*, 380 (2013) 99-105.
- [69] T. Sochacki, Z. Bryan, M. Amilusik, M. Bobea, M. Fijalkowski, I. Bryan, B. Lucznik, R. Collazo, J.L. Weyher, R. Kucharski, HVPE-GaN grown on MOCVD-GaN/sapphire template and ammonothermal GaN seeds: Comparison of structural, optical, and electrical properties, *Journal of Crystal Growth*, 394 (2014) 55-60.
- [70] P. Kempisty, B. Łuczniak, B. Pastuszka, I. Grzegory, M. Boćkowski, S. Krukowski, S. Porowski, CFD and reaction computational analysis of the growth of GaN by HVPE method, *Journal of Crystal Growth*, 296 (2006) 31-42.

- [71] P. Kempisty, S. Krukowski, Crystal growth of GaN on (0001) face by HVPE-atomistic scale simulation, *Journal of Crystal Growth*, 303 (2007) 37-43.
- [72] J. Uhlrich, M. Garcia, S. Wolter, A.S. Brown, T.F. Kuech, Interfacial chemistry and energy band line-up of pentacene with the GaN (0001) surface, *Journal of Crystal Growth*, 300 (2007) 204-211.
- [73] P. Kempisty, S. Krukowski, Crystal growth of GaN on (0001) face by HVPE: Ab initio simulations, *Journal of Crystal Growth*, 310 (2008) 900-905.
- [74] A. Ishii, T. Aisaka, First-principle calculation of the epitaxial growth of GaN(0001), *physica status solidi (c)*, 0 (2003) 2490-2493.
- [75] F. Gao, E. Bylaska, W. Weber, Intrinsic defect properties in GaN calculated by ab initio and empirical potential methods, *Physical Review B*, 70 (2004).
- [76] D. Moscatelli, P. Caccioppoli, C. Cavallotti, Ab initio study of the gas phase nucleation mechanism of GaN, *Applied Physics Letters*, 86 (2005) 091106.
- [77] N. Takeuchi, A. Selloni, T. Myers, A. Doolittle, Adsorption and diffusion of Ga and N adatoms on GaN surfaces: Comparing the effects of Ga coverage and electronic excitation, *Physical Review B*, 72 (2005).

- [78] M. Ganchenkova, R. Nieminen, Nitrogen Vacancies as Major Point Defects in Gallium Nitride, *Physical Review Letters*, 96 (2006).
- [79] W.H. Moon, C.H. Choi, Molecular-dynamics study of inversion domain boundary in w-GaN, *Physics Letters A*, 352 (2006) 538-542.
- [80] T. Kawamura, Y. Kangawa, K. Kakimoto, Investigation of thermal conductivity of GaN by molecular dynamics, *Journal of Crystal Growth*, 284 (2005) 197-202.
- [81] D.E. Boucher, G.G. DeLeo, W.B. Fowler, Simulations of GaN using an environment-dependent empirical tight-binding model, *Physical Review B*, 59 (1999) 10064.
- [82] W.H. Moon, H.J. Hwang, Structural and thermodynamic properties of GaN: a molecular dynamics simulation, *Physics Letters A*, 315 (2003) 319-324.
- [83] K. Harafuji, T. Tsuchiya, K. Kawamura, Molecular dynamics simulation of dislocations in wurtzite-type GaN crystal, *Journal of Applied Physics*, 96 (2004) 2513.
- [84] X. Zhou, D. Murdick, B. Gillespie, H. Wadley, Atomic assembly during GaN film growth: Molecular dynamics simulations, *Physical Review B*, 73 (2006).
- [85] D. Sengupta, S. Mazumder, W. Kuykendall, S.A. Lowry, Combined ab initio quantum chemistry and computational fluid dynamics calculations

- for prediction of gallium nitride growth, *Journal of Crystal Growth*, 279 (2005) 369-382.
- [86] C.E.C. Dam, P.R. Hageman, P.K. Larsen, Carrier gas and position effects on GaN growth in a horizontal HVPE reactor: An experimental and numerical study, *Journal of Crystal Growth*, 285 (2005) 31-40.
- [87] A.S. Segal, A.V. Kondratyev, S.Y. Karpov, D. Martin, V. Wagner, M. Ilegems, Surface chemistry and transport effects in GaN hydride vapor phase epitaxy, *Journal of Crystal Growth*, 270 (2004) 384-395.
- [88] C.E.C. Dam, A.P. Grzegorzcyk, P.R. Hageman, R. Dorsman, C.R. Kleijn, P.K. Larsen, The effect of HVPE reactor geometry on GaN growth rate—experiments versus simulations, *Journal of Crystal Growth*, 271 (2004) 192-199.
- [89] Ł.J. Sytniewski, A.A. Lapkin, S. Stepanov, W.N. Wang, CFD optimisation of up-flow vertical HVPE reactor for GaN growth, *Journal of Crystal Growth*, 310 (2008) 3358-3365.
- [90] W. Seifert, G. Fitzl, E. Butter, Study on the growth rate in VPE of GaN, *Journal of Crystal Growth*, 52 (1981) 257-262.
- [91] C. Dam, T. Bohnen, C. Kleijn, P. Hageman, P. Larsen, Scaling up a horizontal HVPE reactor, *Surface and Coatings Technology*, 201 (2007) 8878-8883.
- [92] C.-A. manual, CFD-ACE manual, (2011.0).

- [93] N. Liu, J. Wu, W. Li, R. Luo, Y. Tong, G. Zhang, Highly uniform growth of 2-inch GaN wafers with a multi-wafer HVPE system, *Journal of Crystal Growth*, 388 (2014) 132-136.
- [94] Z. Zhang, H. Fang, H. Yan, Z. Jiang, J. Zheng, Z. Gan, Influencing factors of GaN growth uniformity through orthogonal test analysis, *Applied Thermal Engineering*, 91 (2015) 53-61.
- [95] X.-F. Han, M.-J. Hur, J.-H. Lee, Y.-j. Lee, C.-s. Oh, K.-W. Yi, Numerical simulation of the gallium nitride thin film layer grown on 6-inch wafer by commercial multi-wafer hydride vapor phase epitaxy, *Journal of Crystal Growth*, 406 (2014) 53-58.
- [96] S. Hu, S. Liu, Z. Zhang, H. Yan, Z. Gan, H. Fang, A novel MOCVD reactor for growth of High-quality GaN-related LED layers, *Journal of Crystal Growth*, (2015).
- [97] K. Zhou, J. Liu, S. Zhang, Z. Li, M. Feng, D. Li, L. Zhang, F. Wang, J. Zhu, H. Yang, Hillock formation and suppression on c-plane homoepitaxial GaN Layers grown by metalorganic vapor phase epitaxy, *Journal of Crystal Growth*, 371 (2013) 7-10.
- [98] E. Valcheva, T. Paskova, B. Monemar, Nanopipes and their relationship to the growth mode in thick HVPE-GaN layers, *Journal of crystal growth*, 255 (2003) 19-26.

- [99] A. Zauner, J. Weyher, M. Plomp, V. Kirilyuk, I. Grzegory, W. Van Enckevoort, J. Schermer, P. Hageman, P. Larsen, Homo-epitaxial GaN growth on exact and misoriented single crystals: suppression of hillock formation, *Journal of crystal growth*, 210 (2000) 435-443.
- [100] T. Wei, R. Duan, J. Wang, J. Li, Z. Huo, Y. Zeng, Hillocks and hexagonal pits in a thick film grown by HVPE, *Microelectronics Journal*, 39 (2008) 1556-1559.
- [101] F. Oehler, T. Zhu, S. Rhode, M. Kappers, C. Humphreys, R. Oliver, Surface morphology of homoepitaxial *c*-plane GaN: Hillocks and ridges, *Journal of Crystal Growth*, 383 (2013) 12-18.
- [102] J.K. Kennedy, W.D. Potter, The effect of various growth parameters on the formation of pits and hillocks on the surface of epitaxial GaAs layers, *Journal of Crystal Growth*, 19 (1973) 85-89.
- [103] B.J. Baliga, S.K. Ghandhi, Hillocks on epitaxial GaAs grown from trimethylgallium and arsine, *Journal of Crystal Growth*, 26 (1974) 314-316.
- [104] C. Kisielowski, J. Krüger, S. Ruvimov, T. Suski, J. Ager III, E. Jones, Z. Liliental-Weber, M. Rubin, E. Weber, M. Bremser, Strain-related phenomena in GaN thin films, *Physical Review B*, 54 (1996) 17745.
- [105] Y. Han, M. Caliebe, M. Kappers, F. Scholz, M. Pristovsek, C. Humphreys, Origin of faceted surface hillocks on semi-polar GaN

- templates grown on pre-structured sapphire, *Journal of Crystal Growth*, 415 (2015) 170-175.
- [106] C. Hemmingsson, G. Pozina, M. Heuken, B. Schineller, B. Monemar, Modeling, optimization, and growth of GaN in a vertical halide vapor-phase epitaxy bulk reactor, *Journal of Crystal Growth*, 310 (2008) 906-910.
- [107] W.C. Lan, C.D. Tsai, C.W. Lan, The effects of shower head orientation and substrate position on the uniformity of GaN growth in a HVPE reactor, *Journal of the Taiwan Institute of Chemical Engineers*, 40 (2009) 475-478.
- [108] S.Y. Karpov, Y.N. Makarov, M. Ramm, The role of gaseous species in group-III nitride growth, *MRS Internet Journal of Nitride Semiconductor Research*, 1 (1996).
- [109] M. Averyanova, I. Przhevalskii, S.Y. Karpov, Y.N. Makarov, M. Ramm, R. Talalaev, Analysis of vaporization kinetics of group-III nitrides, *Materials Science and Engineering: B*, 43 (1997) 167-171.
- [110] S.Y. Karpov, D. Zimina, Y.N. Makarov, B. Beaumont, G. Nataf, P. Gibart, M. Heuken, H. Jürgensen, A. Krishnan, Modeling study of hydride vapor phase epitaxy of GaN, *physica status solidi (a)*, 176 (1999) 439-442.

- [111] S.Y. Karpov, Advances in the modeling of MOVPE processes, *Journal of crystal growth*, 248 (2003) 1-7.
- [112] E. Aujol, J. Napierala, A. Trassoudaine, E. Gil-Lafon, R. Cadoret, Thermodynamical and kinetic study of the GaN growth by HVPE under nitrogen, *Journal of crystal growth*, 222 (2001) 538-548.
- [113] H.-P. Liu, J.-D. Tsay, W.-Y. Liu, Y.-D. Guo, J.T. Hsu, I.-G. Chen, The growth mechanism of GaN grown by hydride vapor phase epitaxy in N₂ and H₂ carrier gas, *Journal of Crystal Growth*, 260 (2004) 79-84.
- [114] M. Jamil, H. Zhao, J.B. Higgins, N. Tansu, Influence of growth temperature and V/III ratio on the optical characteristics of narrow band gap (0.77 eV) InN grown on GaN/sapphire using pulsed MOVPE, *Journal of Crystal Growth*, 310 (2008) 4947-4953.
- [115] M. Jamil, R.A. Arif, Y.K. Ee, H. Tong, J.B. Higgins, N. Tansu, MOVPE of InN films on GaN Templates grown on sapphire and silicon (111) Substrates, *physica status solidi (a)*, 205 (2008) 1619-1624.
- [116] A. Claudel, V. Fellmann, I. Gélard, N. Coudurier, D. Sauvage, M. Balaji, E. Blanquet, R. Boichot, G. Beutier, S. Coindeau, Influence of the V/III ratio in the gas phase on thin epitaxial AlN layers grown on (0001) sapphire by high temperature hydride vapor phase epitaxy, *Thin Solid Films*, 573 (2014) 140-147.

- [117] J. Elsner, R. Jones, M. Heggie, P. Sitch, M. Haugk, T. Frauenheim, S. Öberg, P. Briddon, Deep acceptors trapped at threading-edge dislocations in GaN, *Physical Review B*, 58 (1998) 12571.
- [118] A. Hangleiter, F. Hitzel, C. Netzel, D. Fuhrmann, U. Rossow, G. Ade, P. Hinze, Suppression of nonradiative recombination by V-shaped pits in GaInN/GaN quantum wells produces a large increase in the light emission efficiency, *Physical review letters*, 95 (2005) 127402.
- [119] B. Monemar, H. Larsson, C. Hemmingsson, I.G. Ivanov, D. Gogova, Growth of thick GaN layers with hydride vapour phase epitaxy, *Journal of crystal growth*, 281 (2005) 17-31.
- [120] H. Ashraf, J.L. Weyher, G.W.G. van Dreumel, A. Gzregorzyck, P.R. Hageman, Thick GaN layers grown by HVPE: Influence of the templates, *Journal of Crystal Growth*, 310 (2008) 3957-3963.
- [121] L. Lymperakis, J. Neugebauer, M. Albrecht, T. Remmele, H. Strunk, Strain Induced Deep Electronic States around Threading Dislocations in GaN, *Physical Review Letters*, 93 (2004).
- [122] M. Barchuk, C. Röder, Y. Shashev, G. Lukin, M. Motylenko, J. Kortus, O. Pätzold, D. Rafaja, Correlation between the residual stress and the density of threading dislocations in GaN layers grown by hydride vapor phase epitaxy, *Journal of Crystal Growth*, 386 (2014) 1-8.

초 록

본 논문에서는 새롭게 개발된 멀티 웨이퍼 수소화 기상 증착 (HVPE) 설비에서, 질화 갈륨 증착 두께 균일도에 대한 파라미터의 영향을 실험 분석 및 수치 해석을 이용하여 연구하였다.

계산 및 실험 결과와의 비교를 통해, 캐리어 가스 유량을 증가시키면 증착 속도의 최대 값의 위치가 이동될 수 있고 웨이퍼 내에 증착 두께 분포의 균일도를 증가시킬 수 있다는 것을 결과를 얻었고 계산과 실험의 경향성이 잘 일치함을 확인할 수 있었다. 또한, 증착 두께 균일도에 대한 온도 및 압력의 영향, 서셉터의 회전 속도의 영향, 웨이퍼 회전 속도의 영향, 캐리어 가스 조성의 영향을 표준 편차 분석을 통해 비교하고 평가하였다. 그 중 웨이퍼의 회전은 복잡성으로 인한 계산의 효율성 저하 때문에 직접 모델링하지 않았다. 대신 증착 속도 분포를 얻기 위해 서셉터 회전 및 웨이퍼 회전의 결합 효과를 고려하고 웨이퍼에서 한 점의 궤적을 추적하는 방법을 사용하였다. 계산 결과를 통해 높은 캐리어 가스 유량, 높은 온도, 낮은 압력, 낮은 회전 속도 및 순수한 질소 조건들을 사용했을 때 최적의 증착 두께 균일도를 얻을 수 있다는 결론을 얻었다.

웨이퍼 반경 방향에 따라 hillock 밀도 분포에 영향을 미치는 인자들을 알아내기 위해 유동과 물질 전달, 증착 속도 분포에 대한 수치 해석을 진행하였다. 계산 결과에서 서셉터의 회전에 의해 웨이퍼의 증착 속도가 높아지고 낮아지는 현상을 발견하였고, 노즐로부터의 거리에 따른 성장 속도의 fluctuation 에 대한 표준 편차를 분석하여 비교하였다. 계산 결과로부터 웨이퍼 중심으로부터 외곽으로 갈 수록 방위각에 따라 증착 속도의 표준 편차가 증가함을 볼 수 있었고, 이에 따라 hillock 밀도가 중심으로부터 외곽으로 갈 수록 증가하는 이유를 확인할 수 있었다. 또한, 불균일한 증착 속도는 서셉터의 저속 회전 때문인 것을 계산을 통해 확인할 수 있었다. 만약 서셉터의 회전 속도를 증가시키면 가스 유동과 증착 속도의 균일도를 향상시킬 수 있다. 즉, 높은 회전 속도가 방위각에 따른 증착 속도의 표준 편차를 감소시킬 수 있다. 따라서, 멀티 웨이퍼 HVPE 설비에서 서셉터의 고속 회전은 hillock 의 형성을 방지할 수 있다는 결론을 얻을 수 있었다.

웨이퍼 표면에 증착된 질화 갈륨 박막의 두께 분포 및 V/III 비율 분포를 분석하기 위해 3D 멀티 서셉터 공정 모델을 개발하였다. 질화 갈륨 박막은 1213 K, 1 Bar 에서 멀티 셉터 HVPE 설비를 통해 성장되는 조건을 가정하였다. 계산 결과를 통해 V/III 비율이

중심에서부터 외곽으로, 하단 서셉터에서부터 상단 서셉터로 갈수록 증가하는 것을 확인할 수 있었다. 그리고 LMM (Laser Measuring Microscope) 을 이용해 실험으로 얻어진 GaN 박막 표면의 pit 형상을 관찰하였고, pit 의 밀도가 중심으로부터 외곽으로, 하단 서셉터에서부터 상단 서셉터로 갈수록 감소하는 것을 확인함으로써 계산 결과와 실험 결과가 일치함을 확인하였다. 본 연구를 통해 질화 갈륨 표면의 pit 분포에 대한 수치적인 예측이 가능한 모델을 개발할 수 있었다.

주요어: 질화 갈륨, 기상증착 에피택시, 수치해석, 유동, 표면 반응

학번: 2011-22858